Deformation and cluster structures in light nuclei studied with configuration mixing using Skyrme interaction

Yuta Fukuoka

February 2014

Deformation and cluster structures in light nuclei studied with configuration mixing using Skyrme interaction

Yuta Fukuoka
Doctoral Program in Physics

Submitted to the Graduate School
of Pure and Applied Sciences
in Partial Fulfillment of the Requirements
for the Degree of Doctor of Philosophy in Science

at the
University of Tsukuba

Abstract

We present an investigation of the structure of the ^{12}C, ^{16}O, and ^{20}Ne nuclei employing a newly developed configuration-mixing method. Our method is composed of the following steps. We first generate a number of Slater-determinants with various correlated structures using the imaginary-time algorithm. We then diagonalize a many-body Hamiltonian of the Skyrme interaction in the space spanned by the Slater-determinants with parity and angular momentum projections. These calculations are carried out in the grid representation of the three-dimensional Cartesian coordinate. This method allow us to get almost converged solution for the ground and low-lying excited states once the many-body Hamiltonian is given.

Our calculations reasonably describe the ground and excited states of ^{12}C nucleus, both shell-model-like and cluster-like states. The excitation energies and transition strengths of the ground-state rotational band are well described. Negative-parity excited states, 1^-_1, 2^-_1, and 3^-_1 are also reasonably described. The second and third 0^+ states, 0^+_2 and 0^+_3, appear at around 8.8 and 15 MeV in our calculations, respectively. The 0^+_2 state shows a structure consistent with a picture of α-condensation which has been proposed recently. However, the calculated radius of the 0^+_2 state is smaller than previous calculations. The three α-linear-chain configuration is found to dominate in the 0^+_3 state.

For the ^{16}O nucleus, we show that the α+^{12}C cluster structure dominates in the 0^+_2 state, though calculated excitation energy of this state is too high about 3 MeV compared with the measured value. For negative-parity excited states, the parity-doublet partner of $K^\pi = 0^+_2$ band appears as $J^\pi = 1^-_3$ and 3^-_3 states. Negative parity excited states of 1^-_1, 2^-_1, and 3^-_1, which are known to be particle-hole excited states, are reasonably described.

For the ^{20}Ne nucleus, the ground band is described by our method as states which shows α+^{16}O configuration. The calculated $E2$ transition strengths between states belonging to ground-state rotational band is well reproduced, although moment of inertia for these states is too large compared with the measurements. In the negative parity, our calculation describes $K^\pi = 2^-$ band reasonably which is known as 1p-1h excitations. The parity-doublet partner of $K^\pi = 0^+_1$ band appears in our calculations. However, we cannot obtain converged solutions for this band.

In addition to Skyrme interaction, we perform calculations using Gogny interaction. We have found that results are almost the same, showing that our calculated results do not depend on the choice of the effective Hamiltonian.

Contents

Chapter 1

Introduction

1.1 Structures of light nuclei

Atomic nuclei are finite quantum many-body systems composed of a number of nucleons. There are two kind of nucleons; neutron and proton. Less than 300 stable nuclei are found in nature, and about 3,000 nuclei have been produced and investigated in experiments. It is considered that a mean-field picture of nuclei — nucleons constituting a nucleus make a mean field potential self-consistently and nucleons move independently in the potential — applies for most nuclei. In the shell-model (SM), a picture that relatively weak interactions among nucleons which move in the mean-field potential is assumed. SM has been very successful in explaining the basic nuclear properties. Recently, the tensor-optimized shell model has been developed to take into account the tensor correlations which originate dominantly from pion exchange [1].

In spite of successful descriptions of nuclear properties, SM cannot provide satisfactory description of cluster structures. In light nuclei, cluster structures are widely observed in excited states. In most light nuclei, ground states are described by the SM. There are only a few cases where cluster structures appear in the ground state. On the other hand, a variety of cluster structures appear in excited states. Due to the saturation property of the nuclear binding energy, it costs only small energy to break light nuclei into clusters. In stable nuclei, cluster structures appear in excitation energy regions close to the threshold energy into a few clusters. This is called the threshold energy rule and has been described by the so-called Ikeda diagram [2] which is shown in Fig. 1.1. In the diagram, possible cluster structures are plotted at positions where a vertical distance from the top indicates the threshold into clusters measured from the threshold energy into α-particles. Ground states of nuclei appear along a diagonal line. They are thought to be shell-model like states except for ^{8}Be. In each cluster structure, measured threshold energy is indicated in the parenthesis in unit of MeV. We consider ^{12}C, for example. The threshold energy into three α-particles is 7.27 MeV. A cluster structure composed of three α-particles structure is expected at around this excitation energy. Indeed, the 0_2^+ excited state exists whose excitation energy is 7.66 MeV in measurement. This state is considered to have the three α-cluster structure. It is quite interesting that a variety of cluster structures appear in excited states which have very different structures from the

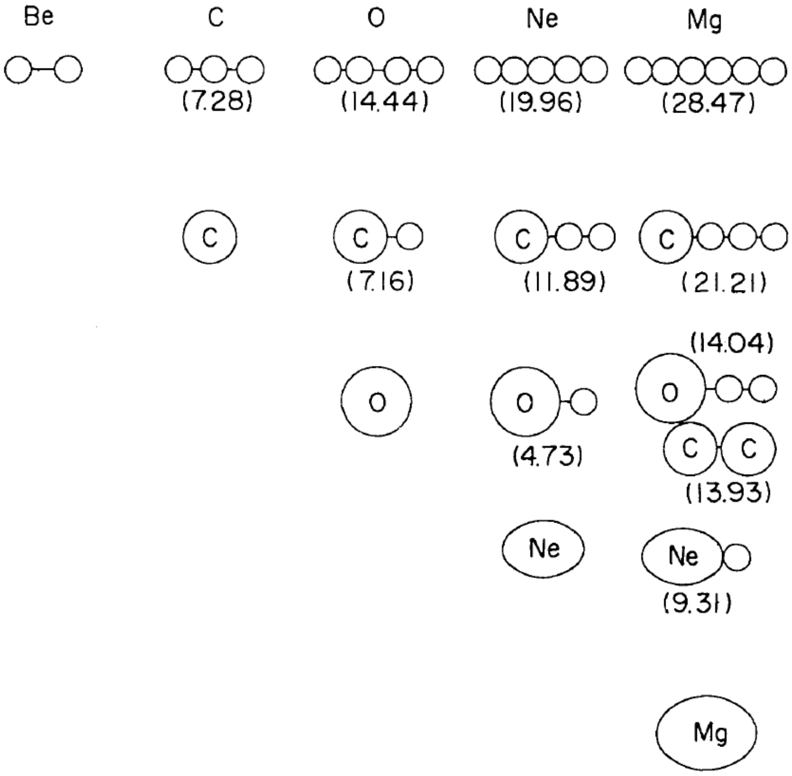

Figure 1.1: Ikeda diagram. Possible cluster structures are shown according to the threshold rule. Threshold energy for each decay mode is indicated in the parenthesis in MeV. Ground states of nuclei appear along a diagonal line. They are shell-model like states except for ^{8}Be. (From [2])

ground state.

1.2 Cluster models and *ab-initio* calculations

For theoretical descriptions of cluster states, microscopic and semi-microscopic cluster models have been extensively developed in the past [3–5]. The resonating group method (RGM) [6, 7] assumes a product form for the wave function composed of the internal wave functions of clusters and the inter-cluster wave function, taking full account of the anti-symmetrization. The generator coordinate method (GCM) has been also successfully applied to various cluster motions assuming harmonic oscillator shell-model wave functions for clusters [8]. One of semi-microscopic cluster models is the orthogonality condition model (OCM) which is considered to be an approximation of the RGM [9, 10]. In these microscopic and semi-microscopic models, the existence of clusters is assumed from the beginning. To understand mechanisms of emergence and disappearance of cluster structures, one should start with a model which

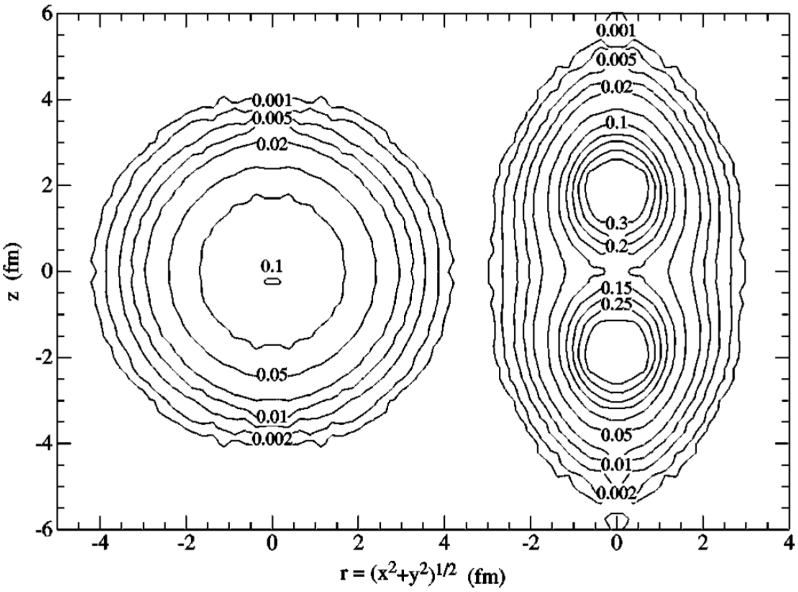

Figure 1.2: Contours of constant density, plotted in cylindrical coordinates, for the ground state of ^{8}Be. The left side is in the laboratory frame while the right side is in the intrinsic frame. (From [15])

does not assume any existence of clusters. Studies with the anti-symmetrized molecular dynamics (AMD) method [11–13] have contributed to substantial advances in this direction. In most calculations with microscopic cluster models and AMD, effective nucleon-nucleon forces are used. In the fermionic molecular dynamics (FMD) method, which is closely related to the AMD, a more realistic force produced by the unitary correlation operator method has been employed [14].

In last two decades, there have been significant advances in theoretical descriptions of light nuclei starting with realistic nucleon-nucleon force: the so-called *ab initio* approaches. The Green function Monte Carlo (GFMC) approach has been successful in describing the ground and some low-lying excited states of light nuclei [16]. The GFMC calculation describes the two α-cluster structure of ^{8}Be in the ground state [15]. Figure 1.2 shows the contour plot of density plotted in cylindrical coordinates, while the left side of the figure is in the laboratory frame. The right side of the figure is in the intrinsic frame. The intrinsic density exhibits two α-cluster. However, in spite of the success of description of cluster structure for ^{8}Be, the application of the GFMC method has been limited to nuclei whose mass number is less than or equal to 12, because the computational cost rapidly increases as the mass number increases. The no-core shell model (NCSM) has also been successful for the description of ground and low-lying excited states [17, 18]. However, descriptions of cluster states in the NCSM have not yet been satisfactory. For example, the calculated first excitation energy ($J^{\pi} = 0_2^+$) of ^{16}O by no-core full configuration (NCFC) approach, which is a similar approach to the NCSM, is about two times larger than that of measurement [19]. Recently there have been a number of attempts at the *ab initio* description of cluster structures in excited states. For example, a lattice calculation for the second 0^+ state of ^{12}C has been reported [20]. The no-core shell model combined with Monte Carlos basis generation method has also been developed [21].

1.3 Mean field theory

The nuclear self-consistent mean-field (SCMF) theory is one of the successful theoretical approaches for describing and predicting properties of nuclear ground states in a wide mass region of nuclear chart. It is known that calculated bare nucleon-nucleon force may not be used in the SCMF theory because of strong short range repulsion. Instead an empirical effective nucleon-nucleon force has been used. The use of the effective force is theoretically validated by Brückner G-matrix [22]. The Skyrme and Gogny interactions are often used in the SCMF theory [23–26]. The nuclear SCMF theory with these interactions is in many respects analogous to density functional theory, which has been developed in condensed matter theory and has been giving very successful descriptions of various many-electron systems. It has been known that the pairing correlations play an important role in nuclei. In order to take account pairing correlations, the Hartree-Fock-Bogoliubov theory has been developed [27]. The SCMF theory has been quite successful in describing ground state properties such as the binding energies, radii, and so on for a wide mass region of nuclear chart.

The SCMF model has been also applied for the descriptions of excited states. The random-phase approximation (RPA) is the small amplitude limit of time-dependent mean field approach [28]. The RPA is used to describe collective vibrations which represent a coherent motion of many nucleons. To take into account pairing correlations, quasi-particle RPA has been developed. Besides RPA, to describe properties of ground and excited states in a unified way, Generator Coordinate Method (GCM) superposing a number of Slater-determinants (SDs) has been developed [29]. The GCM is a fully variational method and has been successfully applied for various properties of nuclei. In order to perform the GCM calculations, however, we have to choose a few generator coordinates by physical intuition, as in the GCM of the cluster model. This is a disadvantage of the GCM.

1.4 Outline

There are two important ingredients in the *ab initio* descriptions of nuclear structures. One is to start with a Hamiltonian with a realistic nucleon-nucleon force that has a short-range repulsive core. The other is to obtain fully converged solutions for a given many-body Hamiltonian. Since cluster structures are characterized by long-range spatial correlations, simultaneous descriptions of both long- and short-range correlations are required for the *ab-initio* description of cluster states. This makes the problem computationally very challenging. In this thesis, we focus on the latter aspect of the above-mentioned problem; namely, on obtaining fully convergent solutions for a given many-body Hamiltonian, taking into accounts a variety of long-range correlations. We start not with a realistic nucleon-nucleon force but with an empirical effective interaction, the Skyrme force. We use a method developed by our group which was reported previously [30, 31]. We apply the method to the ^{12}C, ^{16}O, and ^{20}Ne nuclei and examine cluster structures in these nuclei. Since the Skyrme interaction is determined so as to reproduce nuclear properties of wide mass region, our calculations contain no empirical parameter specific to ^{12}C, ^{16}O, and ^{20}Ne nuclei.

As seen from Fig. 1.1, ^{12}C, ^{16}O, and ^{20}Ne nuclei are expected to show cluster structures in excited states. The 0_2^+ state of ^{12}C is known as three α-cluster state. In recent year, it has been proposed that the 0_2^+ state can be regard as a gas-like state of three α-particles with Bose condensation [32, 33]. The 0_2^+ state of ^{16}O nucleus is known as $\alpha+^{12}$C cluster state. Although many theoretical approaches has been applied to calculate the 0_2^+ state of ^{16}O nucleus, only the OCM and SM, which include parameters to fit the energy levels, succeed to reasonably reproduce the 0_2^+ state. The ground band of ^{20}Ne nucleus shows transitional behavior between mean-filed and $\alpha+^{16}$O cluster structures. Thus a comprehensive and simultaneous descriptions of the ground and excited states of ^{12}C, ^{16}O, and ^{20}Ne nuclei are very interesting. In this thesis, we will get converged solutions for a given many-body Hamiltonian for these nuclei and discuss the properties of the ground and excited states of these nuclei.

This paper is organized as follows. In chapter 2, we explain our method. We show the results of ^{12}C, ^{16}O, and ^{20}Ne nuclei in chapters 3, 4, and 5, respectively. In chapter 6, a summary is presented and discussed future problems.

Chapter 2

Formulation

We would like to describe structures of light nuclei by employing approach which gives fully convergent solutions for Skyrme Hamiltonian. For this purpose, we use newly developed configuration mixing approach, foundations of which were established in Ref. [30]. In Ref. [30], they use a simplified interaction, BKN. We apply this approach with more realistic Skyrme interaction and try to describe nuclear structures. In this approach, we take sufficiently model space which include cluster wave-functions and diagonalize the effective Hamiltonian in this model space. In the diagonalization of Hamiltonian, we employ projection technique in order to restore broken symmetry. In the following, we explain this approach to divide it into three steps: We first generate a number of Slater-determinants (SDs) in a stochastic way. These SDs are expected to span a sufficiently large model space to describe excited states with various cluster structures as well as low-lying states with shell-model-like structures. We then perform parity and angular momentum projections for the SDs. Finally we superpose them to diagonalize the Skyrme or Gogny Hamiltonian. First, we explain the first step which is to generate and select a sufficient number of SDs. Before presenting this step, we explain the SCMF model which is starting point of our approach.

2.1 Self-consistent mean-filed

2.1.1 Hartree-Fock method

The Hartree-Fock (HF) theory is based on approximation to the many-body wave-function: the wave function is represented by a single SD which is composed of single-particle wave functions ψ_i $(i = 1, \cdots, A)$,

$$\Psi(x_1, \cdots, x_A) = \frac{1}{\sqrt{N!}} \det\{\psi_i(x_j)\}, \tag{2.1.1}$$

where A in number of nucleons and x stand for space, spin, and iso-spin coordinates. This wave-function is satisfied anti-symmetric with regard to interchange of the position of two protons or neutrons. The determinant in Eq. (2.1.1) does not change to replace ψ_i for $\psi_i + c\psi_j$ (c is arbitrary number). In order to remove this uncertainty of single-particle wave-function, we choose the single-particle wave-functions ψ_i to be orthonormal set;

$$\langle\psi_i|\psi_j\rangle = \delta_{ij}. \tag{2.1.2}$$

We now introduce Lagrange multiplier e_{ij} for conserving orthonormality of single-particle wave-function and minimize expectation value of Hamiltonian with respect to single-particle wave-function,

$$\frac{\delta}{\delta\psi_i^*(x)}\left[\frac{\langle\Psi|\hat{H}|\Psi\rangle}{\langle\Phi|\Phi\rangle} - \sum_{ij} e_{ij}(\langle\psi_i|\psi_j\rangle - \delta_{ij})\right] = 0. \tag{2.1.3}$$

From this equation, we can be obtained the HF ground state, which corresponds to the lowest energy state in the model space represented by a single SD.

The Bonche *et al.* were developed numerical method for HF with representation of the three-dimensional (3D) Cartesian grid, where the spatial coordinates are discretized. We employ same representation. This representation allows us a flexible description of single-particle orbitals in arbitrary nuclear shapes. The grid spacing is taken to be $\Delta x = \Delta y = \Delta z = 0.8$ fm, and the entire grid points inside a sphere of radius $R_{max} = 8.0$ fm are adopted.

2.1.2 Imaginary time method

In order to obtain the HF ground state by numerical calculation, we often use imaginary time method. This method relate to the numerical technique for time-dependent HF equation,

$$i\hbar\frac{\partial\psi_i}{\partial t} = \hat{h}(t)\psi_i(t), \qquad (i = 1, \cdots, A) \tag{2.1.4}$$

where $\hat{h}(t)$ is single-particle Hamiltonian. In numerical calculation of time-dependent HF equation, if we write the state at a certain time $t = n\Delta t$ as $\{\psi_i^{(n)}\}$, the state, $\{\psi_i^{(n+1)}\}$, which is evolved infinitesimal time Δt from $t = n\Delta t$ is written as

$$|\psi_i^{(n+1)}\rangle = \exp\left[\frac{i}{\hbar}\Delta t\hat{h}\right]|\psi_i^{(n)}\rangle. \tag{2.1.5}$$

In imaginary time method, we replace Δt for $i\Delta\tau$, where $\Delta\tau$ is infinitesimal positive value, in Eq. (2.1.5). Thus, the energy of system is gradually decrease as the time τ is evolved. This procedure is called imaginary time method.

We show the example of imaginary time method for HF method. We prepare two SDs, Ψ composed of single-particle wave-functions ψ_i $(i = 1, \cdots, A)$ and $\Psi + \delta\Psi$ composed of $\psi_i + \delta\psi_i$. The expectation value of energy with respect to the SD $\Psi + \delta\Psi$ can be expressed by

$$E[\Psi + \delta\Psi] = E[\Psi] + \sum_{i=1}^{A}\int dx\frac{\delta E}{\delta\psi_i(x)}\delta\psi_i(x) + \sum_{i=1}^{A}\int dx\frac{\delta E}{\delta\psi_i^*(x)}\delta\psi_i^*(x) + O[\delta\psi_i^2], \tag{2.1.6}$$

where $E[\Psi] = \langle\Psi|\hat{H}|\Psi\rangle$. If we take

$$\delta\psi_i \equiv -\Delta\tau\frac{\delta E}{\delta\psi_i^*(x)}, \tag{2.1.7}$$

Eq. (2.1.6) is expressed as

$$E[\Psi + \delta\Psi] \approx E[\Psi] - 2\Delta\tau \sum_{i=1}^{A} \int dx \left| \frac{\delta E}{\delta \psi_i(x)} \right|^2 < E[\Psi]. \tag{2.1.8}$$

The Eq. (2.1.8) indicate that the expectation value of Hamiltonian is decreased as iteration of Eq. (2.1.7) is evolved. We note that the $\frac{\delta E}{\delta \psi_i^*(x)}$ in Eq. (2.1.7) is a definition for single-particle Hamiltonian $\hat{h}$.

2.1.3 Skyrme and Gogny interactions

In the SCMF, zero-range Skyrme interaction and the Gogny interaction are widely used. The Skyrme interaction is composed by the density- and momentum-dependent two-body terms:

$$\begin{aligned} \hat{V}_{Skyrme}(\vec{r}_1, \vec{r}_2) &= t_0 \left(1 + x_0 P_\sigma\right) \delta\left(\vec{r}_1 - \vec{r}_2\right) + \frac{1}{6} t_3 \rho^\alpha \left(1 + x_3 \hat{P}_\sigma\right) \delta\left(\vec{r}_1 - \vec{r}_2\right) \\ &+ \frac{1}{2} t_1 \left(1 + x_1 \hat{P}_\sigma\right) \left(\vec{k}^2 - \vec{k}^2\right) \delta\left(\vec{r}_1 - \vec{r}_2\right) + t_2 \left(1 + x_2 \hat{P}_\sigma\right) \overleftarrow{k} \cdot \delta\left(\vec{r}_1 - \vec{r}_2\right) \overrightarrow{k} \\ &+ iW_0 \left(\vec{\sigma}_1 + \vec{\sigma}_2\right) \cdot \overleftarrow{k} \times \delta\left(\vec{r}_1 - \vec{r}_2\right) \overrightarrow{k}, \end{aligned} \tag{2.1.9}$$

where $\hat{P}^\sigma$ is the spin exchange operator, and $\overleftarrow{k}$ and $\overrightarrow{k}$ are defined as

$$\overrightarrow{k} = \frac{\overrightarrow{\nabla}_1 - \overrightarrow{\nabla}_2}{2i}, \quad \overleftarrow{k} = -\frac{\overleftarrow{\nabla}_1 - \overleftarrow{\nabla}_2}{2i}. \tag{2.1.10}$$

Here, $\overrightarrow{k}$ acts on ket state and $\overleftarrow{k}$ acts on bra state. The some parameter sets of Skyrme interaction are given in Table A.1. The matrix element of $\hat{V}_{Skyrme}$ is shown in Sec. A.1 and the off-diagonal matrix element of $\hat{V}_{Skyrme}$ is shown in Sec. A.3.1. We use the Skyrme interaction to generate and prepare SDs and diagonalize of Hamiltonian. For the energy functional, we employ the SLy4 parameter set for the Skyrme interaction unless otherwise specified.

The Gogny interaction is constructed by a sum of two Gaussians with spin-isospin mixtures:

$$\begin{aligned} \hat{V}_{Gogny}(\vec{r}_1, \vec{r}_2) = & \sum_{i=1}^{2} \exp\left[-(\vec{r}_1 - \vec{r}_2)^2/\mu_i^2\right] \left(W_i + B_i \hat{P}^\sigma - H_i \hat{P}^\tau - M_i \hat{P}^\sigma \hat{P}^\tau\right) \\ & + iW_0 (\vec{\sigma}_1 + \vec{\sigma}_2) \cdot \overleftarrow{k} \times \delta(\vec{r}_1 - \vec{r}_2) \overrightarrow{k} \\ & + t_3 \rho^{1/3} \left(1 + \hat{P}^\sigma\right) \delta\left(\vec{r}_1 - \vec{r}_2\right), \end{aligned} \tag{2.1.11}$$

where $\hat{P}^\tau$ is the isospin exchange operator. The some parameter sets of Gogny interaction are given in Table A.2. The matrix element of $\hat{V}_{Gogny}$ is shown in App. A.2. We use Gogny interaction to perform diagonalization of Hamiltonian.

2.2 Generation of Slater-determinants

The first step is generation and selection of sufficient number of SDs, $\{\Psi_i\}$ $(i = 1.\cdots, M)$, which are expected to span a sufficiently large model span to describe various kinds of long-range correlations. For this purpose, we use imaginary-time method which is usually used to obtain a ground-state solution in the SCMF calculation. Here, we apply it for generation of many kinds of collective surfaces.

We start with initial SDs whose single-particle orbitals are described by Gaussian wave packets,

$$\phi_i(\vec{r}, \sigma) = e^{-\left|\vec{r}-\vec{R}_i(\sigma)\right|^2/a^2}. \tag{2.2.1}$$

The width parameter a is taken to be 2 fm and the center of the Gaussian wave packets, $\vec{R}_i(\sigma)$, are set by random numbers generated on the condition

$$\left|\vec{R}_i(\sigma)\right| < R_{max} - 1 \text{ fm}. \tag{2.2.2}$$

Then, we start the imaginary-time iterations with these initial SDs. During the imaginary-time iterations, we employ constraints to place the center of mass at the origin and to make the principal axes of nuclei parallel to the Cartesian axes. After sufficient number of iterations, the calculation reaches the self-consistent HF ground-state. Before reaching HF solution, many SDs which show various cluster structures and other important configurations for low-lying dynamics appear. We pick up and store these SDs, which will be used for the configuration mixing calculation. We repeat the imaginary-time calculation starting with different initial SDs until we obtain a sufficient number of SDs. We typically generate 50 SDs.

In order to span a wide model space by the limited number of SDs, the actual calculation is achieved as follows: The first SD adopted in the basis set $\{\Psi_i\}$ is the HF state, $\Phi_1 = \Phi_{HF}$. The second and following SDs are generated as follows: We examine the energy expectation value in a regular interval, typically every a hundred iterations. We do not adopt the SD until the energy expectation value is less than 30 MeV above the HF ground-state energy. Once the excitation energy fall below the threshold, we examine the overlap between a current SD Φ_c and previously selected ones Φ_i $(i = 1, \cdots, N)$. We calculate the overlap

$$\frac{\left|\langle\Phi_i|\hat{P}^\pi \hat{R}_n|\Phi_c\rangle\right|}{\sqrt{\left|\langle\Phi_i|\hat{P}^\pi|\Phi_i\rangle\right|}\sqrt{\left|\Phi_c|\hat{P}^\pi|\Phi_c\rangle\right|}} \quad (i = 1, \cdots, N), \tag{2.2.3}$$

where $\hat{P}^\pi$ is parity projection operator $\pi = \pm$ and $\hat{R}_n$ $(n = 1, \cdots, 24)$ are operators of rotations and inversions which may be easily achieved by changes of the coordinate axes. If the largest overlap value between Φ_c and Φ_i $(i = 1, \cdots, N)$ is less than 0.7, we adopt the SD Φ_c as a new member, $\Phi_{N+1} = \Phi_c$. When the imaginary-time iteration reaches the HF solution, we generate a new initial SD whose single particle wave function are described by Gaussian wave packets (2.2.1) and perform the imaginary-time iterations again. We repeat the procedure until a sufficient number of SDs is adopted. A few SDs are adopted during an imaginary-time iteration in the beginning. However, it is more and more difficult to obtain the new SD as a number of stored SDs are increases. We sometime cannot obtain any SDs.

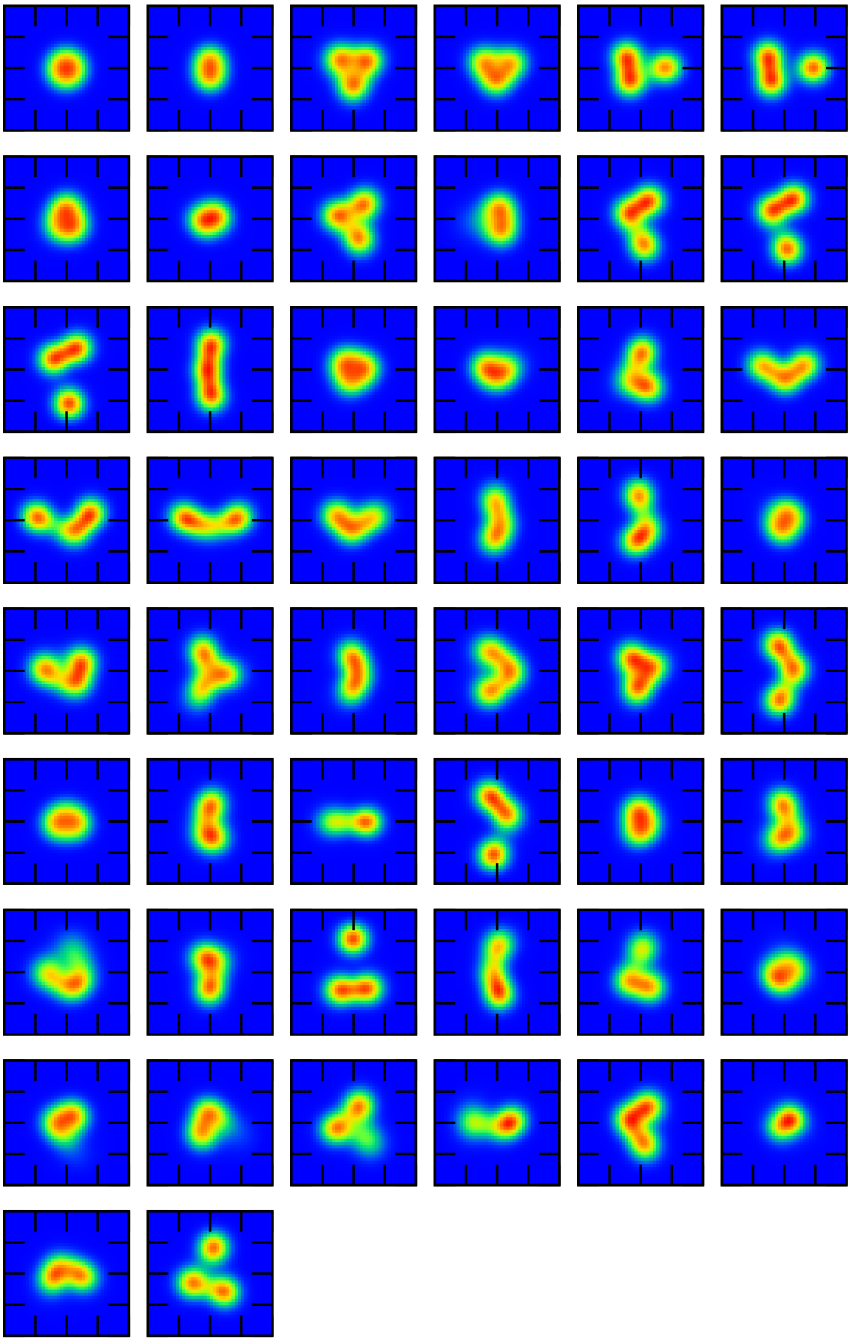

Figure 2.1: Color plots of nuclear densities of the stored SDs for ^{12}C. Lengths of a side are 16 fm.

In this way, we can store SDs which are linearly independent to each other and which are important to describe low-lying excitation states.

We show density distributions of 50 SDs generated in this procedure in Fig. 2.1. The HF solution for the ground state, which shows a spherical shape, is shown in upper-left corner. Other SDs in Fig. 2.1 show a variety of cluster structures. For example, some SDs show an equilateral triangular three-α structure, some show a three-α linear-chain, and some show a $^8\mathrm{Be} + \alpha$-like structure. We thus observe that the present procedure efficiently produces SDs with various cluster structures in an automatic manner.

2.3 Parity and angular momentum projections

The exact many-body Hamiltonian is invariant under some symmetry operations such as the particle number, the linear momentum, the space inversion, the angular momentum operators, and so on:

$$\left[\hat{H}, \hat{S}\right] = 0, \tag{2.3.1}$$

where $\hat{S}$ is symmetry operator. Therefore, the eigenvectors of $\hat{H}$ are simultaneously eigenstate of $\hat{S}$. Since the SDs prepared by the method in Sec. 2.2 are not usually eigenstate of parity and angular momentum, we should restore this broken symmetries. For this purpose, we use projection methods. We explain parity projection and angular momentum projection.

2.3.1 Parity projection

In order to restore the space inversion symmetry of Hamiltonian, from the wave function Φ, we produce the wave function $\Phi^{(\pm)}$ which the parity, positive $+$ or negative $-$, is determined:

$$\Phi^{(+)} \equiv \hat{P}^{+}\Phi = \frac{1}{2}(1+\hat{P}_r)\Phi, \qquad \Phi^{(-)} \equiv \hat{P}^{-}\Phi = \frac{1}{2}(1-\hat{P}_r)\Phi, \tag{2.3.2}$$

where $\hat{P}_r$ is space inversion operator. The $\Phi^{(\pm)}$ has space inversion symmetry.

2.3.2 Angular momentum projection

We can get eigenstate of squared and z-component of total angular momentum, J^2 and J_z, is constructed by operating following projection operator,

$$\hat{P}^{J}_{MK} = \frac{2J+1}{8\pi^2}\int d\Omega D^{J*}_{MK}(\Omega)\hat{R}(\Omega), \tag{2.3.3}$$

where $\hat{R}(\Omega)$ is the rotation operator for the Euler angels $\Omega = (\alpha, \beta, \gamma)$, and D^{J}_{MK} is the Wigner's D-function defined by

$$\hat{R}(\Omega) = e^{-i\alpha\hat{J}_z}e^{-i\beta\hat{J}_y}e^{-i\gamma\hat{J}_z}, \tag{2.3.4}$$

$$D^{J}_{MK}(\Omega) = e^{-i\alpha M}d^{J}_{MK}(\beta)e^{-i\gamma K}, \tag{2.3.5}$$

where J, M, and K are the total angular momentum, its projection onto the laboratory z-axis, and its projection onto the body-fixed z-axis, respectively.

We define the norm and Hamiltonian matrix elements between the projected SDs, $|\Phi_i\rangle$ and $|\Phi_j\rangle$ as

$$\hat{n}^{J\pi}_{iK,j,K'} \equiv \frac{2J+1}{8\pi^2}\int d\Omega D^{J*}_{KK'}(\Omega)\left\langle \Phi_i \left| e^{-i\alpha\hat{J}_z}\hat{P}^{\pi}e^{-i\beta\hat{J}_y}e^{-i\gamma\hat{J}_z} \right| \Phi_j \right\rangle \tag{2.3.6}$$

$$\hat{h}^{J\pi}_{iK,j,K'} \equiv \frac{2J+1}{8\pi^2}\int d\Omega D^{J*}_{KK'}(\Omega)\left\langle \Phi_i \left| e^{-i\alpha\hat{J}_z}\hat{H}\hat{P}^{\pi}e^{-i\beta\hat{J}_y}e^{-i\gamma\hat{J}_z} \right| \Phi_j \right\rangle. \tag{2.3.7}$$

Here, we use the formula

$$\hat{P}^{J\dagger}_{MK}\hat{P}^{J}_{MK'} = \hat{P}^{J}_{KK'}. \tag{2.3.8}$$

In Eqs. (2.3.6) and (2.3.7), we need the rotation of wave functions. It is achieved by successive operations of small angle rotations. For example, the rotation of a wave function ϕ over an angle γ around z-axis is archived by successive rotations of a small angle, $\Delta\gamma = \gamma/N_\gamma$, N_γ times.

$$e^{-i\Delta\gamma\hat{j}_z}\left|\phi\right\rangle = \left[e^{-i\Delta\gamma\hat{j}_z}\right]^{N_\gamma}\left|\phi\right\rangle . \tag{2.3.9}$$

To achieve the small-angle rotation, we employ the Taylor expansion method:

$$e^{-i\Delta\gamma\hat{j}_z}\left|\phi\right\rangle \approx \sum_{k=1}^{N_{max}} \frac{(-i\Delta\gamma\hat{j}_z)^k}{k!}\left|\phi\right\rangle . \tag{2.3.10}$$

Typically, we take $N_{max} = 4$ and $\Delta\gamma = \pi/90$.

In Eqs. (2.3.6) and (2.3.7), the $e^{-i\alpha\hat{J}_z}$ is operated on bra $\langle\Phi_i|$. The $e^{-i\beta\hat{J}_y}$ and $e^{-i\gamma\hat{J}_z}$ is operated on ket $|\Phi_j\rangle$. The integrals over Euler angles are evaluated as follows: Those over α, β, and γ are archived by the trapezoidal rule, taking 18 uniform grid points for $[0, 2\pi]$. The integral β is achieved with the Gauss-Legendre quadrature, taking 30 grid points for $[0, \pi]$.

2.4 Configuration mixing

The final procedure is diagonalization of the many-body Hamiltonian in the space spanned by the selected SDs. The SDs have been screened by their linear independence. However, calculating eigenvalues of the norm matrix for the SDs after the parity and angular momentum projections, we find a number of eigenvalues very close to zero or even slightly negative. The norm matrix is positive definite by definition. However, since we make numerical approximations in evaluating the norm matrix, it could contain negative eigenvalues. The approximations include use of the formula for the product of the projection operators, which is no longer exact if the integral over Euler angles is evaluated by the numerical quadrature. We also employ the three-dimensional Cartesian grid representation for the orbitals in which the rotational symmetry holds only approximately.

Inclusion of those configurations of very small norm eigenvalues would lead to numerical difficulties. Therefore, we reproduce the number of configurations according to the following procedures. First, we perform diagonalization in the $(2J + 1)$-multiplet with different K quantum numbers:

$$\sum_{K'} n^{J\pi}_{iK,iK'} v^{J\pi,i,\nu}_{K'} = e^{J\pi}_{i\nu} v^{J\pi,i\nu}_{K}, \quad (\nu = 1, \cdots, 2J + 1), \tag{2.4.1}$$

where $e^{J\pi}_{i\nu}$ and $v^{J\pi,i\nu}_{K}$ are eigenvalues and eigenvalues of the norm matrix, $n^{J\pi}_{iK,iK'}$. Then we construct a space spanned by the eigenvectors with the eigenvalue $e^{J\pi}_{i\nu} > 10^{-2}$, and define the normalized basis functions

$$\left|\Phi^{J\pi}_{i\nu}\right\rangle \equiv \frac{1}{\sqrt{e^{J\pi}_{i\nu}}} \sum_{K} v^{J\pi,i,\nu}_{K} \hat{P}^{J}_{MK}\hat{P}^{\pi}\left|\Phi_i\right\rangle . \tag{2.4.2}$$

After achieving the above procedure for all SDs, we define the following norm matrix between basis functions belonging to the different SDs:

$$\hat{n}^{J\pi}_{i\nu,j\nu'} \equiv \left\langle \Phi^{J\pi}_{i^n u} \right| \left. \Phi^{J\pi}_{j\nu'} \right\rangle . \tag{2.4.3}$$

Using this matrix, we examine the linear independence of the basis functions and reduce the number of bases as follows.

1. Calculate eigenvalues of 2×2 matrices composed of every possible pair of basis functions, $(i_1\nu_1)$ and $(i_2\nu_2)$. If the smaller eigenvalue is less than 10^{-3}. we remove the basis function with a smaller $e^{J\pi}_{i\nu}$.

2. Calculate the eigenvalues of 3×3 matrices composed of three basis functions $(i_1\nu_1)$, $(i_2\nu_2)$, and $(i_3\nu_3)$. If the smallest eigenvalue is less than 10^{-3}, we remove one of the three basis functions in the following procedure. We calculate eigenvalues of three 2×2 submatrices composed of all possible pairs of these three states, to find the pair whose smaller eigenvalue is the largest among the three. Then we remove one of the basis function of $(i_1\nu_1)$, $(i_2\nu_2)$, and $(i_3\nu_3)$ which does not belong to that pair. We repeat the procedure for all possible combinations of three basis functions.

3. Finally we calculate eigenvalues of the norm matrix $\hat{n}^{J\pi}_{i\nu,j\nu'}$ with basis functions which survived in the previous two screening steps. If we find the eigenvalue smaller than 10^{-3}, we remove one basis function in the following way. Denoting the number of basis functions as N, we construct the $(N-1) \times (N-1)$ submatrices removing one basis function $\Phi^{J\pi}_{i\nu}$ from the N basis. Apparently, N different choices of $(i\nu)$ are possible. We then calculate the smallest eigenvalue of the $(N-1) \times (N-1)$ submatrix, $\lambda^{(i\nu)}_{min}$. Among $\lambda^{(i\nu)}_{min}$ with different $(i\nu)$, we find the largest one, $\lambda^{(j,\nu')}_{min}$, and remove the basis function $\Phi^{J\pi}_{j\nu'}$ is reduced by one, from N to $N-1$. We repeat this process until the smallest eigenvalue of the norm matrix becomes larger than 10^{-3}.

After removing the overcomplete basis functions in this procedure, we achieve the configuration mixing calculation. Denoting the nth energy eigenvalues as

$$\left|\Phi^{J\pi}_{n}\right\rangle \equiv \sum_{i\nu} f^{J\pi,n}_{i\nu} \left|\Phi^{J\pi}_{i\nu}\right\rangle , \tag{2.4.4}$$

the generalized eigenvalue equation for the energy eigenvalues $E^{J\pi}_{n}$ and the coefficients $f^{J\pi,n}_{n}$ is given by

$$\sum_{j\nu} \left[\hat{h}^{J\pi}_{i\nu,j\nu'} - E^{J\pi}_{n} \hat{n}^{J\pi}_{i\nu,j\mu} \right] f^{J\pi,n}_{j\mu} = 0, \tag{2.4.5}$$

where $\hat{h}^{J\pi}_{i\nu,j\mu}$ is defined by

$$\hat{h}^{J\pi}_{i\nu,j\mu} \equiv \left\langle \Phi^{J\pi}_{i\nu} \right| \hat{H} \left| \Phi^{J\pi}_{j\mu} \right\rangle . \tag{2.4.6}$$

2.5 Matrix elements of nuclear interactions

In the last of this chapter, we show the matrix element of Hamiltonian $\langle\Phi|\hat{H}|\Phi\rangle$, which is need to perform imaginary time evolution and get $\hat{h}^{J\pi}_{i\nu,j\mu}$.

2.5.1 Skyrme interaction

First, we present the matrix elements of Skyrme interaction. The energy expectation value of a SD is written as

$$E_{HF}[\Phi] = \left\langle \Phi \left| \hat{H}_{Skyrme} \right| \Phi \right\rangle = \int d\vec{r} \mathcal{H}_{Skyrme}(\vec{r}), \tag{2.5.1}$$

where the local energy functional $\mathcal{H}_{Skyrme}$ is given by

$$\begin{aligned}
\mathcal{H}_{Skyrme} = {} & \frac{\hbar^2}{2m}\tau + B_1\rho^2 + B_2\sum_\tau \rho^{(\tau)2} \\
& + B_3\left(\tau\rho - \vec{j}^2\right) + B_4\sum_\tau\left(\tau^{(\tau)}\rho^{(\tau)} - \vec{j}^{(\tau)2}\right) \\
& + B_5\rho\nabla^2\rho + B_6\sum_\tau\left(\rho^{(\tau)}\Delta\rho^{(\tau)}\right) + B_7\rho^\alpha\rho^2 + B_8\rho^\alpha\sum_\tau\rho^{(\tau)2} \\
& + B_9\left[\rho\vec{\nabla}\cdot\vec{J} + \vec{j}\cdot\vec{\nabla}\times\vec{\rho} + \sum_\tau\left(\rho^{(\tau)}\vec{\nabla}\cdot\vec{J}^{(\tau)} + \vec{j}^{(\tau)}\cdot\vec{\nabla}\times\vec{\rho}^{(\tau)}\right)\right] \\
& + B_{10}\vec{\rho}^2 + B_{11}\sum_\tau\vec{\rho}^{(\tau)2} + B_{12}\rho^\alpha\vec{\rho}^2 + B_{13}\rho^\alpha\sum_\tau\vec{\rho}^{(\tau)2} \\
& + B_{14}\left(\vec{T}\cdot\vec{\rho} - \vec{J}^2\right) + B_{16}\sum_\tau\left(\vec{T}^{(\tau)}\cdot\vec{\rho}^{(\tau)} - \vec{J}^{(\tau)2}\right) \\
& + B_{15}\vec{\rho}\cdot\Delta\vec{\rho} + B_{17}\sum_\tau\vec{\rho}^{(\tau)}\cdot\Delta\vec{\rho}^{(\tau)},
\end{aligned} \tag{2.5.2}$$

where τ denote neutron or proton. The coefficients $B_i (i = 1, \cdots, 17)$ are defined as

$$\begin{aligned}
B_1 &= \frac{1}{2}t_0\left(1 + \frac{1}{2}x_0\right), & B_2 &= -\frac{1}{2}t_0\left(\frac{1}{2} + x_0\right), \\
B_3 &= \frac{1}{4}\left[t_1\left(1 + \frac{1}{2}x_1\right) + t_2\left(1 + \frac{1}{2}x_2\right)\right], & B_4 &= -\frac{1}{4}\left[t_1\left(\frac{1}{2} + x_1\right) - t_2\left(\frac{1}{2} + x_2\right)\right], \\
B_5 &= -\frac{1}{16}\left[3t_1\left(1 + \frac{1}{2}x_1\right) - t_2\left(1 + \frac{1}{2}x_2\right)\right], & B_6 &= \frac{1}{16}\left[3t_1\left(\frac{1}{2} + x_1\right) + t_2\left(\frac{1}{2} + x_2\right)\right], \\
B_7 &= \frac{1}{12}t_3\left(1 + \frac{1}{2}x_3\right), & B_8 &= -\frac{1}{12}t_3\left(\frac{1}{2} + x_3\right), \\
B_9 &= -\frac{1}{2}W_0, \\
B_{10} &= \frac{1}{4}t_0x_0, & B_{11} &= -\frac{1}{4}t_0,
\end{aligned}$$

$$
\begin{aligned}
B_{12} &= \frac{1}{24} t_3 x_3, & B_{13} &= -\frac{1}{24} t_3, \\
B_{14} &= \frac{1}{8}\left(t_1 x_1 + t_2 x_2\right), & B_{15} &= -\frac{1}{32}\left(3t_1 x_1 - t_2 x_2\right), \\
B_{16} &= -\frac{1}{8}\left(t_1 - t_2\right), & B_{17} &= \frac{1}{32}\left(3t_1 + t_2\right).
\end{aligned}
$$

The energy functional Eq. (2.5.2) is composed of several densities, which are written by using single-particle wave function as

$$\rho(\vec{r}) = \sum_i \sum_\sigma |\phi_i(\vec{r},\sigma)|^2, \tag{2.5.3a}$$

$$\rho^{(\tau)}(\vec{r}) = \sum_{i\in\tau} \sum_\sigma |\phi_i(\vec{r},\sigma)|^2, \tag{2.5.3b}$$

$$\tau(\vec{r}) = \sum_i \sum_\sigma |\vec{\nabla}\phi_i(\vec{r},\sigma)|^2, \tag{2.5.3c}$$

$$\tau^{(\tau)}(\vec{r}) = \sum_{i\in\tau} \sum_\sigma |\vec{\nabla}\phi_i(\vec{r},\sigma)|^2, \tag{2.5.3d}$$

$$J_\mu(\vec{r}) = \sum_{\lambda\mu\nu} \epsilon_{\lambda\mu\nu} J_{\mu\nu}(\vec{r}), \tag{2.5.3e}$$

$$J_{\mu\nu}(\vec{r}) = \frac{1}{2i} \sum_i \sum_{\sigma\sigma'} \left[\phi_i^*(\vec{r},\sigma)\partial\mu\phi_i(\vec{r},\sigma') - \partial_\mu\phi_i^*(\vec{r},\sigma)\phi_i(\vec{r},\sigma')\right] \left\langle\sigma|\sigma_\nu|\sigma'\right\rangle, \tag{2.5.3f}$$

$$J_\mu^{(\tau)}(\vec{r}) = \sum_{\lambda\mu\nu} \epsilon_{\lambda\mu\nu} J_{\mu\nu}^{\tau}(\vec{r}), \tag{2.5.3g}$$

$$J_{\mu\nu}^{(\tau)}(\vec{r}) = \frac{1}{2i} \sum_{i\in\tau} \sum_{\sigma\sigma'} \left[\phi_i^*(\vec{r},\sigma)\partial_\mu\phi_i(\vec{r},\sigma') - \partial_\mu\phi_i^*(\vec{r},\sigma)\phi_i(\vec{r},\sigma')\right] \left\langle\sigma|\sigma_\nu|\sigma'\right\rangle, \tag{2.5.3h}$$

$$\vec{\rho}(\vec{r}) = \sum_i \sum_{\sigma\sigma'} \phi_i^*(\vec{r},\sigma)\phi_i(\vec{r},\sigma') \left\langle\sigma|\vec{\sigma}|\sigma'\right\rangle, \tag{2.5.3i}$$

$$\vec{\rho}^{(\tau)}(\vec{r}) = \sum_{i\in\tau} \sum_{\sigma\sigma'} \phi_i^*(\vec{r},\sigma)\phi_i(\vec{r},\sigma') \left\langle\sigma|\vec{\sigma}|\sigma'\right\rangle, \tag{2.5.3j}$$

$$\vec{j}(\vec{r}) = \frac{1}{2i} \sum_i \sum_\sigma \left[\phi_i^*(\vec{r},\sigma)\vec{\nabla}\phi_i(\vec{r},\sigma) - \vec{\nabla}\phi_i^*(\vec{r},\sigma)\phi_i(\vec{r},\sigma)\right], \tag{2.5.3k}$$

$$\vec{j}^{(\tau)}(\vec{r}) = \frac{1}{2i} \sum_{i\in\tau} \sum_\sigma \left[\phi_i^*(\vec{r},\sigma)\vec{\nabla}\phi_i(\vec{r},\sigma) - \vec{\nabla}\phi_i^*(\vec{r},\sigma)\phi_i(\vec{r},\sigma)\right], \tag{2.5.3l}$$

$$\vec{T}(\vec{r}) = \sum_i \sum_{\sigma\sigma'} \vec{\nabla}\phi_i^*(\vec{r},\sigma)\cdot\vec{\nabla}\phi_i(\vec{r},\sigma') \left\langle\sigma|\vec{\sigma}|\sigma'\right\rangle, \tag{2.5.3m}$$

$$\vec{T}^{(\tau)}(\vec{r}) = \sum_{i\in\tau} \sum_{\sigma\sigma'} \vec{\nabla}\phi_i^*(\vec{r},\sigma)\cdot\vec{\nabla}\phi_i(\vec{r},\sigma') \left\langle\sigma|\vec{\sigma}|\sigma'\right\rangle. \tag{2.5.3n}$$

2.5.2 Gogny interaction

We show the matrix element of Gogny Hamiltonian, which has finite range Gaussians. Since numerical calculation with three-dimensional mesh representation is not suitable for finite range interaction, the performing calculation of this matrix element in our method has trouble. We discuss how to reduce computational cost.

In the following discussion, we neglect the degree of freedom of spin for simplicity. The expectation value of Hartree term for $\hat{V}$ is given by

$$V_H = \int d\vec{r} \int d\vec{r}' \rho(\vec{r})\rho(\vec{r}')v(|\vec{r} - \vec{r}'|), \tag{2.5.4}$$

where

$$\rho(\vec{r}) = \sum_i \phi_i^*(\vec{r})\phi_i(\vec{r}). \tag{2.5.5}$$

Here, i is orbital number and the integral of $\vec{r}$ and $\vec{r}'$ is performed to all of the space. Similarly, the expectation value of Fock term for $\hat{V}$ is given by

$$V_F = \int d\vec{r} \int d\vec{r}' \rho(\vec{r}, \vec{r}')\rho(\vec{r}', \vec{r})v(|\vec{r} - \vec{r}'|), \tag{2.5.6}$$

where

$$\rho(\vec{r}, \vec{r}') \equiv \sum_i \phi_i^*(\vec{r})\phi(\vec{r}'). \tag{2.5.7}$$

The numerical calculation of expectation values demand higher calculation cost, because both expectation values (Eqs. 2.5.4 and 2.5.6) include sextuple integral; three dimensions of $\vec{r}$ and $\vec{r}'$. Above two, the expectation value of Fock term is more difficult than that of Hartree term, because we have to calculate $\rho(\vec{r}, \vec{r}')$ (Eq. (2.5.7)) to the number of mesh points for $\vec{r}$ and $\vec{r}'$. In order to reduce computational cost, we develop two methods: Finite spherical lattice and Fourier transform. Below we describe these two methods in order.

Finite spherical lattice

Since the potential v is finite range interaction, the strength of potential become smaller as $|\vec{r} - \vec{r}'|$ is larger. Namely, in Eq. (2.5.6), we can neglect some integration points of $\vec{r}'$ which is far from the point $\vec{r}$. In actual calculation, the integral for $\vec{r}$ is performed on all mesh points, and the integral for $\vec{r}'$ is performed on the points inside a sphere, the center of which locate at $\vec{r}$ and the radius of which is R_f. The schematic picture of this method is shown in Fig. 2.2. The mesh points inside circle is integral points for $\vec{r}'$.

In the Gogny force, the V_F converges if the R_f takes about 3 fm (see Appendix B.1). Numerical cost of this method is proportion to number of mesh points for $\vec{r}$, mesh points inside the sphere for $\vec{r}'$, and orbital numbers, A.

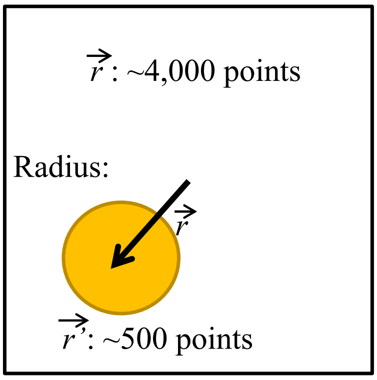

Figure 2.2: Schematic picture for Finite spherical lattice

Fourier transform

We rewrite the Eq. (2.5.6) as

$$\begin{aligned} V_F &= \sum_{i,j} \int d\vec{k} v(\vec{k}) \\ &\times \int d\vec{r} \rho_{ij}(\vec{r}) \text{exp}[i\vec{k} \cdot \vec{r}] \int d\vec{r}' \rho_{ji}(\vec{r}') \text{exp}[-i\vec{k}\vec{r}'], \end{aligned} \tag{2.5.8}$$

where

$$\rho_{ij}(\vec{r}) \equiv \phi_i^*(\vec{r})\phi_j(\vec{r}). \tag{2.5.9}$$

Here, we use the Fourier transform of the potential v

$$v(\vec{r} - \vec{r}') = \int d\vec{r} v(\vec{k}) \text{exp}[-i\vec{k} \cdot (\vec{r} - \vec{r}')]. \tag{2.5.10}$$

From the Eq. (2.5.8), we perform Fourier transform square of number of orbits times. Therefore, numerical cost of this method is proportion to the square of number of orbit, A^2. As shown in Appendix B.1, the numerical cost of Fourier transform method is higher than that of Finite spherical lattice method for nuclei whose mass number is at least 12 or more. In present paper, we adopt Finite spherical lattice method, because numerical cost of this method is lower than that of Fourier transform method.

Chapter 3

Results: ^{12}C

3.1 Structure of ^{12}C

Among light nuclei, the ^{12}C nucleus is one of interesting systems for the reasons described below. In the jj coupling shell-model picture, the ground state wave function should be dominated by the $p_{3/2}$ closed shell configuration. Indeed, the self-consistent Hartree-Fock (HF) solutions with most Skyrme interactions show a spherical shape with the $p_{3/2}$ closed shell configuration. However, the ^{12}C nucleus is known to show a rotational band structure built on the ground state, indicating a deformed intrinsic shape in the ground state. In excited states, a variety of cluster structures are known to appear. The 0_2^+ state just above the three-α decay threshold is an important resonant state for the triple-α fusion reaction. The existence of the Hoyle state is essential for the nuclear synthesis of carbon in helium-burning red giant stars. The state was originally predicted by Fred Hoyle in the 1950s to address of question as to on the observed abundances of heavier element in universe [34]. After that Dunbar and co-workers found the state in experiment of nuclear reaction, and they found that the excitation energy is almost same as predicted value by Fred Hoyle [35]. The state was named Hoyle state after Fred Hoyle. It has been found recently that Hoyle state is well described by a Bose condensed wave function of three-α particles which is called the THSR wave function [32, 33]. Namely, they suggest that the 0_2^+ state of ^{12}C has a gas-like structure of three-α clusters with Bose condensation. The appearance of three-α linear-chain structure in excited states was suggested by Morinaga in 1966 [36]. Recent microscopic cluster models predict that the 0_3^+ state is a candidate for the linear-chain like structure [13, 14].

3.2 Convergence of results: Statistical treatment

In principle, the configuration-mixing calculation with a sufficient number of SDs provides unique and convergent solution. However, superposing a great number of non-orthogonal SDs causes numerical difficulties.

In the present calculation, we adopt 50 SDs for the configuration mixing calculation. It is difficult to increase the number of SDs. Further increase of the number of SDs may produce unphysical solutions whose energies are few tens MeV lower than the ground-state energy of

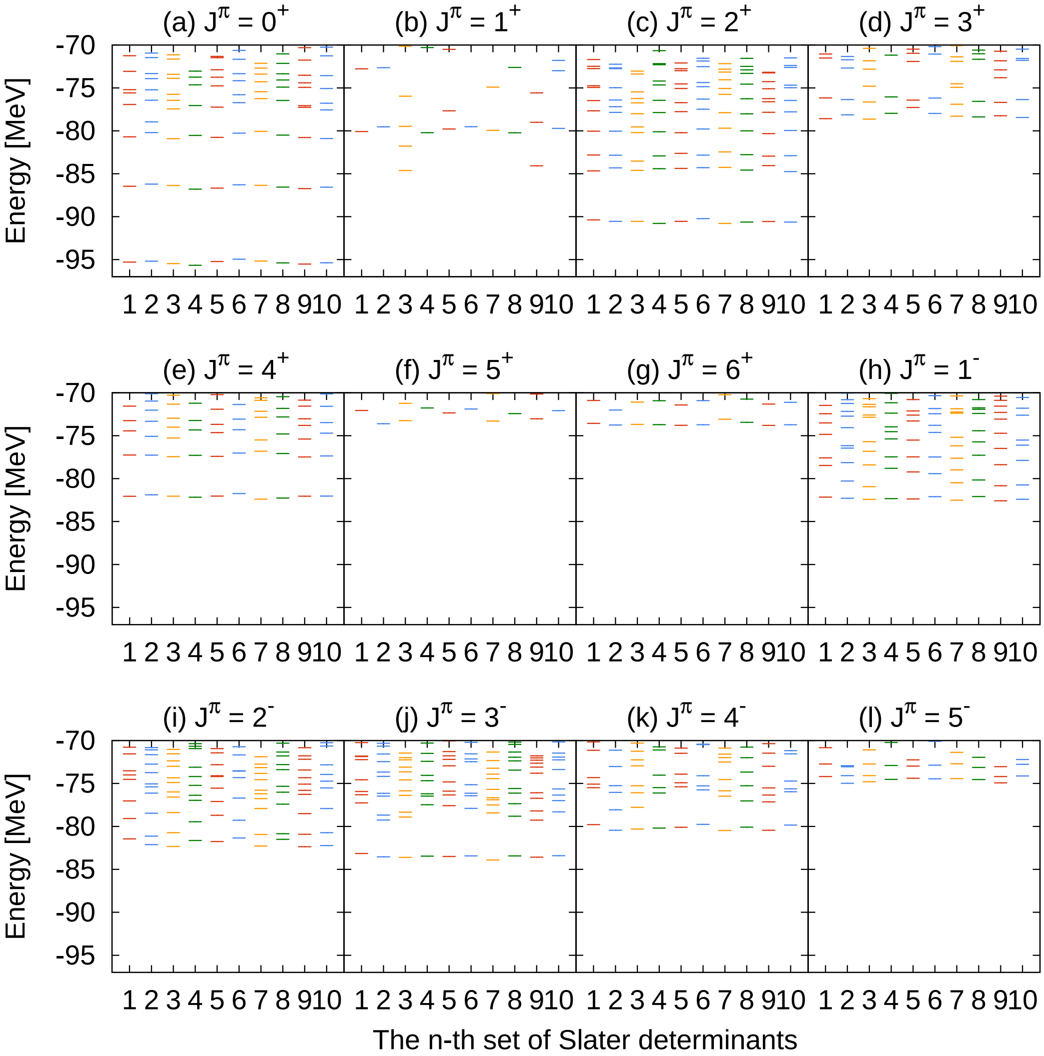

Figure 3.1: Energy levels of the ^{12}C nucleus for $J^\pi = 0^+$, 1^+, 2^+, 3^+, 4^+, 5^+, 6^+, 1^-, 2^-, 3^-, 4^-, and 5^-. Calculations employing ten different sets of SDs are shown. See the text for details.

the HF solution. This is possibly due to accumulations of numerical errors by the violation of rotational symmetries in the three dimensional grid representation, insufficient accuracy in numerical quadrature, and so on.

Because of the difficulty, we will not attempt to examine the convergence of the energy levels by increasing the number of SDs. Instead, we prepare several sets of the SDs and calculate energy levels for each set. If the calculated energy levels are close to each other among the different sets of SDs, one may conclude that the calculated energy levels are reliable. In practice, we prepare ten sets, each of which is composed of 50 SDs. The ten sets of SDs are prepared in the procedure explained in Sec. 2.2. Different seeds for the random numbers, which are used to prepare initial state in Eq. (2.2.1), are employed to generate the different sets.

In Fig. 3.1, we show the energy levels of the ^{12}C nucleus for the ten sets calculated in the procedure explained in Chap. 2. The energy levels are shown for $J^\pi = 0^+$, 1^+, 2^+, 3^+, 4^+, 5^+, 6^+, 1^-, 2^-, 3^-, 4^-, and 5^-.

Let us examine the calculated energy levels of $J^\pi = 0^+$ [Fig. 3.1 (a)]. The lowest level is located around -95 MeV. The difference of energies among the ten sets is smaller than 1 MeV. The second excited state appears again around -86 MeV. The difference among the ten sets is again around 1 MeV. The third excited state appears around -81 MeV. We may state that the energies of these three lowest states are calculated reliably, since the variation is rather small. However, energies of the fourth excited state do not show a good convergence. For example, the energy levels of the second set give the energy around -79 MeV, close to the third state. However, the energy in the seventh set is substantially high, approximately -76 MeV. We thus conclude that we can obtain reliable excitation energies and wave functions for the lowest three levels for $J^\pi = 0^+$.

The energy levels of $J^\pi = 2^+$ in Fig. 3.1(c) indicate that the energies of the lowest four states are reliable with a small variation. For $J^\pi = 3^+$ and 4^+ states [Figs. 3.1(d) and 3.1(e)], the lowest two states may be reliable. For $J^\pi = 5^+$ and 6^+ states [Figs. 3.1(f) and 3.1(g)], the lowest state may be reliable. However, the calculated energies of $J^\pi = 1^+$ states show strong variation among the ten sets even for the lowest state, 3.1(b). This may be due to the fact that the J^π components of the wave function disappear in early stages of the imaginary-time iterations, since components of high-lying levels quickly decay by the imaginary-time propagation. For the negative-parity levels, only the lowest level for each J^π may be reliable. The energies of second lowest levels show a large variation among the ten sets for $J^\pi = 1^-$, 2^-, 3^-, 4^-, and 5^- [Figs. 3.1(h)-3.1(l)].

For physical quantities such as energies, transition strengths, and radii, we calculate statistical averages and standard deviations among the ten sets. The average energy for the nth level of the J^π state is defined by

$$\overline{E}_n^{J\pi} = \frac{1}{N_s} \sum_{i=1}^{N_s} E_{n,i}^{J\pi}, \tag{3.2.1}$$

where i specifies a set among the ten sets, $N_s = 10$. The average excitation energies are calculated as $\overline{E}_n^{J\pi} - \overline{E}_0^{J\pi}$, which will be shown in Figs. 3.2 and 3.3. We also calculate standard deviation of the energies which will be shown by the error bars in the figure. The standard deviation is defined by

$$\sigma_n^{J\pi} = \sqrt{\frac{1}{N_s} \sum_{i=1}^{N_s} \left(E_{n,i}^{J\pi} - \overline{E}_n^{J\pi} \right)^2}. \tag{3.2.2}$$

The average values and the standard deviations for the transition strength and radii are evaluated in the same way.

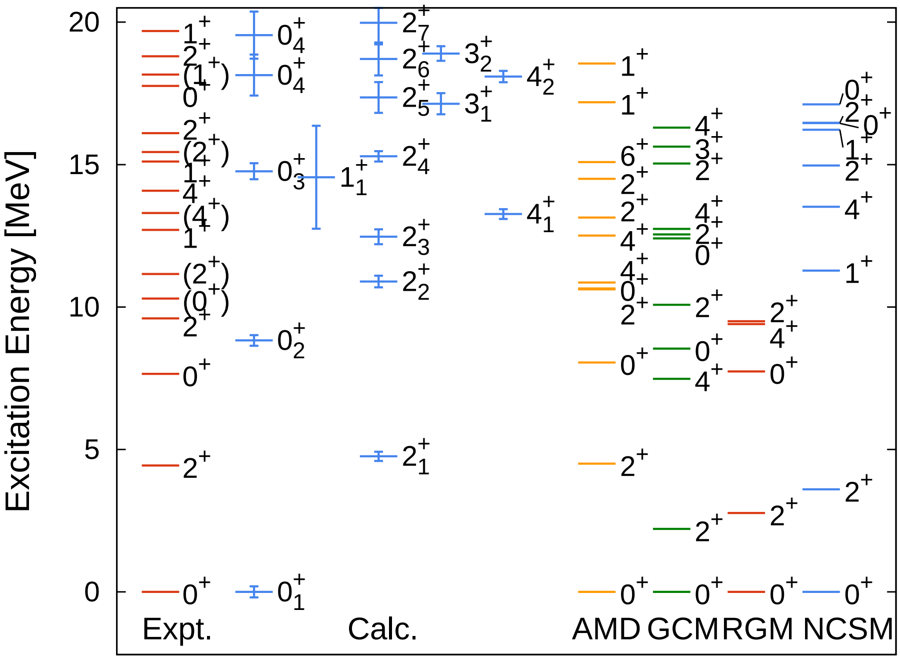

Figure 3.2: Excitation energies of positive-parity for ^{12}C are shown. The energies are obtained by averaging over ten configurations. The standard deviations of the energies are also shown by error bars. We also show the results of AMD [13], GCM [37], RGM [38], and NCSM [39]. Experimental data are taken from Refs. [40–46]. See the text for details.

3.3 Energy levels

We show calculated excitation spectra of positive- and negative-parities in Figs. 3.2 and 3.3, respectively. In the figures, averaged energies over ten sets are shown with error bars as the standard deviation. Our calculated results are compared with measurements and other theories, AMD, GCM, RGM, and NCSM.

In the Skyrme HF calculation, the binding energy of ^{12}C is 90.6 MeV, in reasonable agreement with the measured value, 92.2 MeV. In our configuration-mixing calculation, the correlation energy is 4.7 ± 0.2 MeV. The ground-state energy including the correlation is 95.3 ± 0.2 MeV, slightly lower than the measured value.

Calculated excitation energies of 0^+_1, 2^+_1, and 4^+_1, which are known as ground rotational band, are in good agreement with measurements. For the reproduction of the ground-state band, the configuration-mixing is essential since the ground-state solution in the HF calculation is spherical for ^{12}C with the Skyrme SLy4 interaction. The excitation energy of 2^+_1 state is well reproduced by the present calculation, AMD, and NCSM. However, microscopic α-cluster models (GCM and RGM) provide too low excitation energies. The former models (present, AMD, and NCSM) take into account the spin-orbit interaction, while it is not included in the latter models (GCM and RGM) in which existence of the three α-clusters is

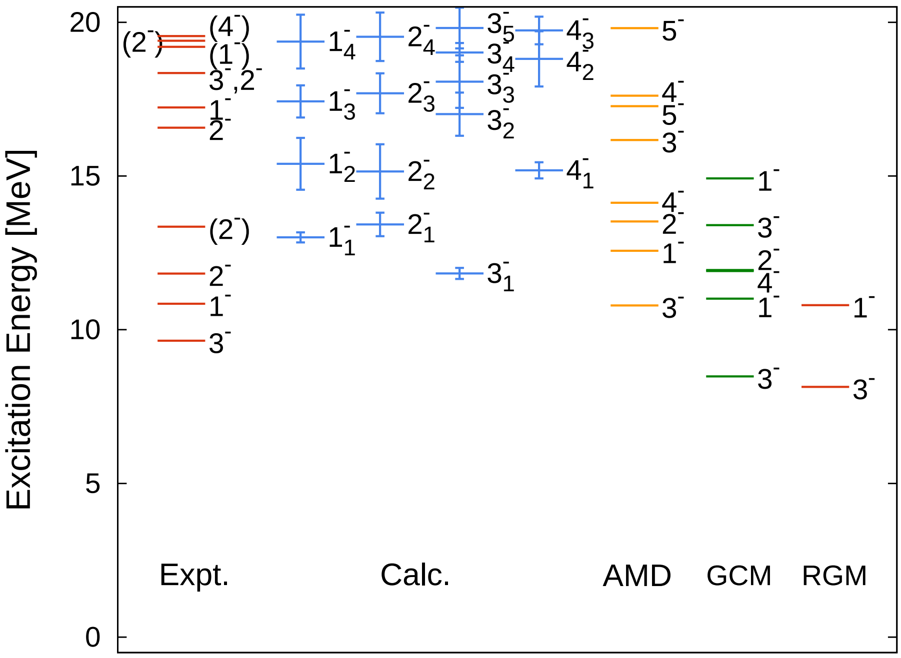

Figure 3.3: Excitation energies of negative-parity for ^{12}C are shown. The same explanation as that in Fig. 3.2 applies to others.

assumed. This indicates that a proper inclusion of the spin-orbit interaction is important for a good description of the ground rotational band.

The 0_2^+ state, which is known as the Hoyle state, has been attracting much attention recently since it has been shown that this state can be understood as the Bose condensed state of three α-particles [33]. Our calculation gives a reasonable description of this state, though the excitation energy is slightly overestimated by about 1 MeV. Although recent *ab-initio* approaches have been successful for the ground-state band, a satisfactory description for the 0_2^+ state adequately. Recently, attempts of *ab-initio* description of for this state have been undertaken by several groups.

Recently, a new 2^+ state has been found experimentally at about 10 MeV excitation energy [41–44]. This state was interrupted as the excited state built on the 0_2^+ state. In [43, 44], a possible splitting of the 2^+ states was suggested. In our calculation, these two state, 2_2^+ and 2_3^+, appear just above the 0_2^+ state. However, as we will discuss in Sec. 3.4, these two states 2_2^+ and 2_3^+ in our calculation seem not to correspond to a rotational excited state of the Hoyle state.

In Fig. 3.2, three states, 0_3^+, 2_4^+, and 4_2^+, follow a rotational energy sequence. The calculated ration of $[E(4^+) - E(2^+)]/[E(2^+) - E(0^+)]$ is 3.22, close to the rotational limit of 3.33. Small standard deviations of the energies of these states indicate the reliability of the calculation. As will be discussed in Sec. 3.4, these states are connected by strong $B(E2)$ transition. In Sec. 3.7, we will show that this band corresponds to a three α-linear-chain

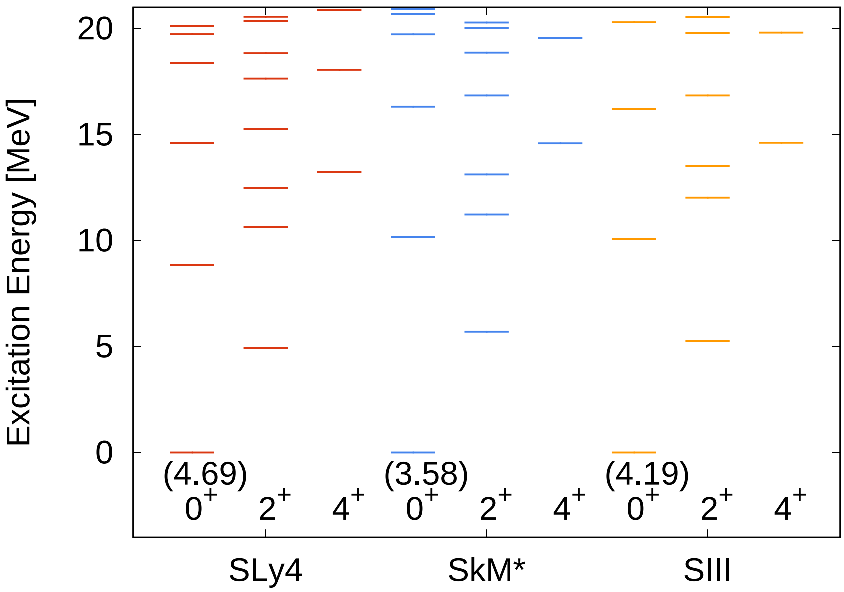

Figure 3.4: Energy levels of positive-parity for ^{12}C employing different parameter sets of Skyrme force, SLy4, SkM* and SIII. The number in parentheses is the correlation energy in the ground state, $E_{\mathrm{HF}} - E_{\mathrm{gs}}$, in unit of MeV. In the calculation, the same set of SDs is employed.

state.

For the negative-parity states, we have obtained solid results only for the lowest energy state for each J^π (Sec. 3.2). Our calculation reproduces the measurements by 2-3 MeV.

Finally we mention how the calculated energy levels depend on interactions. In Figs. 3.4 and 3.5 we show the excitation energies of positive- and negative-parity states with different sets of the Skyrme interaction, SLy4, SkM*, and SGII. The same set of SDs is employed in all calculations. The correlation energies in the ground states are shown as well inside the parentheses. The comparison shows that basic features of the spectra do not depend much on the choice of the Skyrme parameters. We conclude that the excitation energies are not sensitive to choice of interaction for almost all the states below 15 MeV.

3.4 Transition strength

Calculated $B(E2)$, $B(E3)$, and $M(E0)$ values, the average values and the standard deviations, are shown in Table 3.1. In our calculated values, we do not employ any effective charges. The $B(E2)$ transition strength between 2_1^+ and 0_1^+ states is well reproduced by our calculation. It is consistent with results of other theories. The standard deviation is small, about 3% indicating that our calculated value is well converged.

The $B(E2)$ transition between 0_2^+ and 2_1^+ is calculated as $13.6 \pm 1.2 e^2\mathrm{fm}^4$, which is in

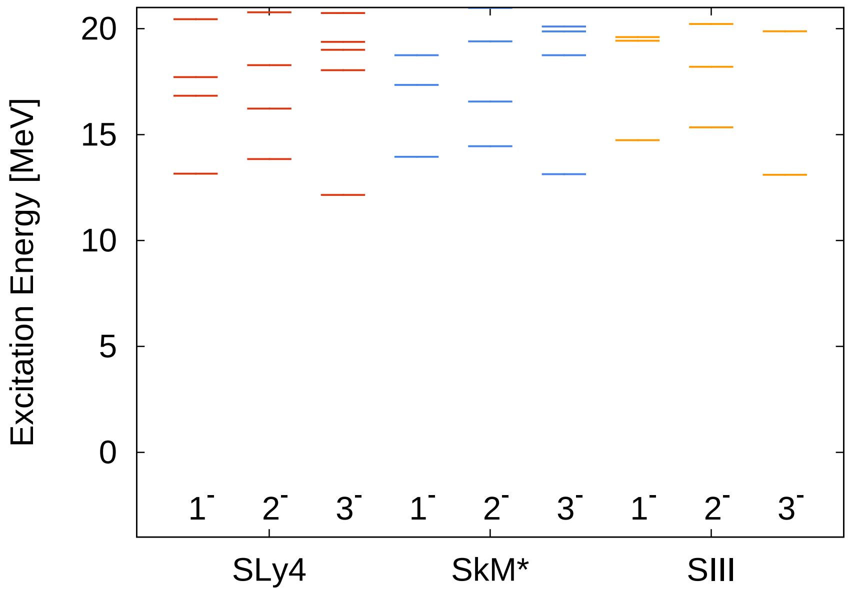

Figure 3.5: Energy levels of negative-parity for ^{12}C employing different parameter sets of Skyrme force, SLy4, SkM* and SIII. In the calculation, the same set of SDs is employed.

excellent agreement with the measured value, $13\pm2e^2\mathrm{fm}^4$, while the rate is strikingly different from the measured value by other theories. In Ref. [13], it is argued that this transition strength is sensitive to the α-breaking effect. A good representation of this transition strength by our calculation indicates that our calculation reasonably takes account of the α-cluster components in the states.

As mentioned in Sec. 3.3, there appear two 2^+ states, 2_2^+ and 2_3^+, above the 0_2^+ state in our calculation. These states might correspond to the 2^+ state at approximately 10 MeV which was discovered recently [41–44]. It was suggested to be a candidate of a rotationally excited state built on the 0_2^+ state. In the present calculation, however, the $B(E2)$ transition strength between 2_2^+ and 0_2^+ is small as seen in Table 3.1. The rate between 0_2^+ and 2_2^+ states is also small. The $B(E2)$ rate from the 0_2^+ state is the largest for the 2_4^+ state, which is regarded as a rotationally excited state built on the 0_3^+ sate, as will be mentioned in the following paragraph. These observations suggest that the 2_3^+ and 2_4^+ states in the present calculation do not correspond to a rotationally excited state on the 0_2^+ state.

As we discussed in Sec. 3.3, the states of 0_3^+, 2_4^+, and 4_2^+ follow the rotational energy sequence. The calculated transition strengths of $B(E2;2_4^+\to0_3^+)$ and $B(E2;4_2^+\to2_4^+)$ are very large. The calculated ratio of $B(E2;4_1^+\to2^+)/B(E2;2_1^+\to0^+)$ is 1.44 ± 0.38, close to the rotational limit of 1.43. These results strongly support that these states indeed constitute a rotational band. In Sec. 3.7, we will show that this band is dominated by the three α-linear-chain structure. In the AMD calculation [13], strong $B(E2)$ values are reported in the transition among 0_3^+, 2_2^+, and 4_2^+ states. Since the states corresponding to 2_2^+ and 2_3^+ in our calculation seem not to be present in the AMD calculation, we put these $B(E2)$ values

Transitions	Expt.	Calc.	AMD	GCM	RGM	NCSM	THSR
$B(E2;2_1^+\to 0_1^+)$	7.6±0.4	8.6 ±0.2	8.5	8.0	9.3	4.146	9.06
$B(E2;4_1^+\to 2_1^+)$		13.4±0.5	16				10.73
$B(E2;0_2^+\to 2_1^+)$	13±2	13.6±1.2	25.5	3.5	5.5		4.71
$B(E2;2_2^+\to 0_2^+)$		0.17±0.23					
$B(E2;2_3^+\to 0_2^+)$		5.9±0.7					
$B(E2;2_4^+\to 0_2^+)$		10±1	100*				391
$B(E2;2_4^+\to 0_3^+)$		91±13	310*				
$B(E2;4_2^+\to 2_4^+)$		131±22	600*				
$B(E3;3_1^-\to 0_1^+)$	107±14	77±4		99	124		
$M(E0;0_1^+\to 0_2^+)$	5.4±0.2	4.5±0.2	6.7	6.6	6.7		6.50

Table 3.1: $B(E2)$, $B(E3)$ and $M(E0)$ values of ^{12}C in units of e^2fm^4, e^2fm^6 and $e$fm^2 respectively. Experimental and calculated values are shown in the first and second column, respectively. For comparison, results of the AMD[13], GCM[37], RGM [38], NCSM [39], and THSR are shown. Values in THSR are calculated with the same model as Ref. [33]. The values indicated by * correspond to $B(E2;2_2^+\to 0_2^+)$, $B(E2;2_2^+\to 0_3^+)$ and $B(E2;4_2^+\to 2_2^+)$ in Ref. [13]. See text for details. Experimental data are taken from Refs. [40].

by AMD at the places of $B(E2;2_4^+\to 0_3^+)$ and $B(E2;4_2^+\to 2_4^+)$ in Table 3.1. In the Ref. [13], these states are considered as the three α-linear-chain states. The large $B(E2)$ values are qualitatively consistent of the transition strengths are much smaller in the present calculation.

For negative-parity states, experimental data for $B(E3;3_1^-\to 0_1^+)$ are available. The present calculation gives $77\pm 4e^2\text{fm}^6$, which is slightly smaller than the measured value, $107\pm 14e^2\text{fm}^6$.

Finally, we discuss the $M(E0)$ transition strength between 0_2^+ and 0_1^+ states. In the studies by cluster models, it has been argued that the magnitude of this transition strength reflects the spatial extension of the 0_2^+ state [47]. Our calculated value, $4.5\pm 0.2e\text{fm}^2$, is slightly smaller than the measured value, $5.4\pm 0.2e\text{fm}^2$. In contrast, microscopic cluster models and AMD have reported an opposite feature, slightly larger values, $6.6-6.7e\text{fm}^2$, than measurements [13, 37, 38]. The THSR model also predicts a similar value, $6.5e\text{fm}^2$. The measured value, $5.4\pm 0.2e\text{fm}^2$ [40], is located between our result and those of the other calculations.

3.5 Radii

We next examine root-mean-square (rms) radii of the ground and excited states. Since our wave function does not allow an exact separation of the center-of-mass motion from the internal one, we estimate an approximate correction for the radius due to the center-of-mass motion, and subtract it from the calculated values. We assume a harmonic oscillator motion for the center-of-mass (see Appendix. B.2). The value of the correction in this model is estimated to be 0.07 fm in the harmonic oscillator shell model. The calculated radii after the

J^π	Expt.	Calc.	AMD	FMD	GCM	RGM	THSR
0_1^+	2.31(2)	2.52±0.01	2.53	2.39	2.40	2.40	2.39
0_2^+		2.73±0.02	3.27	3.38	3.40	3.47	3.80
0_3^+		3.20±0.05	3.98	4.62	3.52		
2_1^+		2.60±0.01	2.66	2.50	2.36	2.38	2.36
2_2^+		2.55±0.01					
2_3^+		2.64±0.01					
2_4^+		3.21±0.05	3.99*	4.43*	3.52*	4.0*	5.4*

Table 3.2: Mass rms radii of the ground and excited states of ^{12}C. The experimental data is taken from Ref. [48]. For comparison, we show the results of AMD [13], FMD [49], GCM [37] , RGM [38], and THSR. The values indicated by * are radii reported for the $J^\pi = 2_2^+$ in the references. See text for details.

correction are shown in Table 3.2.

Our calculated value in the ground state is 2.52 ± 0.01 fm. This value is somewhat larger than the measured value, 2.31 ± 0.02 fm. In the HF calculation, the radius is given by 2.24 fm. Our configuration-mixing calculation, therefore, slightly increases the radius. Comparing with other theories, our value is larger than those of GCM and FMD, and is comparable to the value of AMD.

For the 0_2^+ state, we find a significant different between the radius of the present calculation and the others. Our calculated radius is 2.73 ± 0.02 fm, which is larger than the radius in the ground state. However, this is much smaller than the other calculations which give more than 3 fm [13, 33, 37, 38, 49]. In the recent AMD+GCM calculation [50], a radius of 2.9 fm was reported, similar to ours. It has been found that the interaction used in the AMD calculation [51]. The radius of the 0_2^+ state decreases as the strength of the spin-orbit interaction increases. This dependence is understood as follows [51]. If the strength of the spin-orbit interaction is weak, the ground-state wave function contains a substantial amount of the three α-cluster component. Then, 0_2^+ wave function, which is dominated by dilute three α components, spatially expands to ensure the orthogonalization to the ground state. As the spin-orbit interaction increases, the three α component decreases in the ground state, which allows the 0_2^+ wave function to include a more compact three α structure. This results in decrease of the radius in 0_2^+ state, which may explain the discrepancy in the 0_2^+ radius between our calculation and other theories. It should be noted again that our calculated value for the $M(E0)$ transition strength is smaller than those predicted by other theories. We also note that an indirect measurement of radius for the 0_2^+ state using diffraction inelastic scattering [52] was reported, giving 2.89 ± 0.04 fm.

For the 0_3^+ state, our calculated radius is 3.20 ± 0.05 fm, which is much larger than the radii of 0_1^+ and 0_2^+ states. This is again smaller than those by other theories listed in Table 3.2, while it is similar to the value (3.26 fm) in Ref. [50].

For the 2_1^+ state, our calculated radius is slightly larger than that of the ground state. Other theories report almost the same or a slightly larger radius for this state.

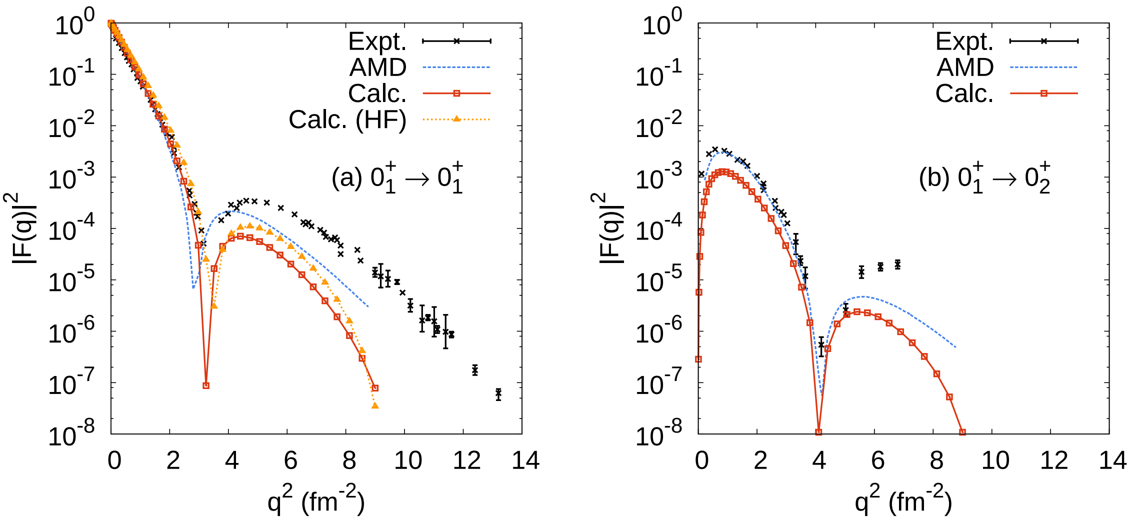

Figure 3.6: Squared elastic form factors for the ground state (left) and $0_1^+ \to 0_2^+$ inelastic form factor (right) are shown. Our calculated results are compared with the HF calculation with a single SD, measurements [53–56], and the AMD calculation [57]. Here, the results using the first set of SDs in Fig. 3.1 are used.

For the 2_2^+ and 2_3^+ states, our calculated radii are slightly larger than that of the ground state, and are slightly smaller than that of the 0_2^+ state. The radius of the 2_4^+ state is large and almost the same that of 0_3^+. This is consistent with a picture that they belong to the same rotational band as discussed in Sec. 3.4. As we mentioned in Sec. 3.4, there is no level corresponding to our 2_2^+ and 2_3^+ states in the AMD calculation. Therefore we put the radius of 2_2^+ state in Table 3.1. We also put those in other cluster model calculations at the place of the 2_4^+ state.

3.6 Charge form factors

A charge form factor from the initial state $|J_i, M_i\rangle$ to the final state $|J_f, M_f\rangle$ is defined as follows:

$$\left|F_{J_i\to J_f}(q^2)\right|^2 = \frac{1}{Z}\frac{1}{2J_i+1}\sum_{M_i,M_f}\left|\left\langle J_f M_f \left| \sum_k \frac{1+\tau_z(k)}{2} e^{i\vec{q}\cdot\vec{r}_k} \right| J_i M_i \right\rangle\right|^2 F_p^2(q^2) F_{cm}^2(q^2) \tag{3.6.1}$$

where Z is the proton number and $\vec{q}$ is the transferred moment. $F_p(q^2)$ is a correction factor for the proton size for which we employ $F_p(q^2) = \exp[-a_p^2 q^2/6]$ with $a_p = 0.813$ fm. To correct the center-of-mass motion, we simply assume that the center-of-mass motion is separated and described by the harmonic oscillator wave function of the same oscillator constant,$\hbar\omega = 41A^{-1/3}$ MeV, for both initial and final states. Thus, this lead to $F_{cm}(q^2) = \exp[q^2 b^2/2A]$ with $b = 1.66$ fm.

In Fig. 3.6, we show charge form factors for the elastic (a) and inelastic $0_1^+ \to 0_2^+$ (b) processes. Red solid curves show our results, blue dashed curves show the results of AMD calculation [58], and crosses with error bars show experimental date [53–56]. For the elastic form factor we also show that of Skyrme HF solution in the ground state.

In the small momentum transfer region $q^2 < 2\mathrm{fm}^{-2}$, the elastic form factor is well reproduced by the calculation. For $q^2 > 2\mathrm{fm}^{-2}$, our calculation underestimates the form factor, though the position of the dip at around $3\mathrm{fm}^{-2}$ is reproduced well. The inelastic form factor for the $0_1^+ \to 0_2^+$ transition is underestimated for a whole momentum transfer region. The position of the dip at around $4\mathrm{fm}^{-2}$ is reproduced well.

We show results by the AMD calculation in Fig. 3.6. They are in good agreement with measured values, although the dip position in elastic form factor is located at a somewhat smaller q^2 value. Microscopic cluster calculations also reproduce the form factors well [37, 38].

The underestimation of the elastic form factor at large q^2 value indicates that the density in our calculation lacks a high-momentum component. Since the HF solution gives a better description for the form factor at high momentum, the superposition of a number of SDs turns out to increase the diffuseness in the nuclear surface, making the density distribution function $\rho(\vec{r})$ smoother. As for the underestimation in the inelastic form factor of the $0_1^+ \to 0_2^+$ transition, a possible reason is the difference in the character of the wave function between the 0_1^+ and 0_2^+ states. As we discussed with the radii, a rather small radius of 0_2^+ state in our calculation may indicate a small fraction of three α component in the ground state. The inelastic form factor may be reduced if the correlation structures are different between two states. It has been argued that the magnitude of this form factor at small q^2 is quite sensitive to the radius of the 0_2^+ state [59]: the magnitude of the form factor at small q^2 reduces as the radius of the 0_2^+ state increases. Our result here is opposite, however. The radius of 0_2^+ state in our calculation is smaller than those by cluster models, and the magnitude of the inelastic form factor is also small. The reasons for these discrepancies are apparently not well settled. This certainly requires further investigation.

3.7 Analysis of wave functions

In order to clarify what kind of correlations are included in the wave function after configuration-mixing, $\Psi_n^{J\pi}$, we calculate the overlap between the energy eigenstate and the projected single SD state,

$$P_n^{J\pi,iK} = \left| \frac{\left\langle \Phi_i \left| \hat{P}_{MK}^{J\dagger} \hat{P}^{\pi} \right| \Psi_n^{J\pi} \right\rangle}{\sqrt{\left\langle \Phi_i \left| \hat{P}_{KK}^{J\dagger} \hat{P}^{\pi} \right| \Phi_i \right\rangle}} \right|^2 \tag{3.7.1}$$

and find the SDs which have large overlap values with $\Psi_n^{J\pi}$. We show density distributions of the SDs visualize the correlations included.

In the following, we use the sequential number of the SDs which we assigned in Sec. 2.2, using the result of the first set of SDs in Fig. 3.1. We also show the K quantum number of the SD and the value of the overlap, $P_n^{J\pi,iK}$, in Eq. (3.7.1).

0_1^+			2_1^+			4_1^+		
SD	K	P	SD	K	P	SD	K	P
15	0	0.90	4	0	89.36	4	0	0.89
7	0	0.87	15	0	88.51	15	0	0.81
8	0	0.85	29	0	82.44	29	0	0.77
31	0	0.85	2	0	76.47	7	0	0.77
2	0	0.82	7	0	75.21	29	1	0.73
42	0	0.80	48	0	72.63	15	1	0.71
24	0	0.80	47	0	65.76	3	0	0.70
4	0	0.79	8	0	64.22	47	0	0.70
16	0	0.79	10	1	63.85	48	0	0.70
35	0	0.77	44	1	63.63	2	0	0.70

Table 3.3: The sequential number, the K-value, and the squared overlap value are shown for the SDs which dominate in the wave function of the ground rotational band.

3.7.1 The ground rotational band

In Table 3.3, we show the sequential number of the SDs which have large overlap values with the wave function of the ground rotational band, 0_1^+, 2_1^+, and 4_1^+. The overlap values $P_n^{J\pi,iK}$ defined by Eq, (3.7.1) and K values are shown as well. Since the SDs are nonorthogonal, the sum of the overlap values is not equal but much larger than unity.

In the ground state 0_1^+, the 15th SD has the largest overlap, showing 0.90 for the overlap value. In 2_1^+ and 4_1^+ states, the 4th SD is the largest component and the 15th SD is the second largest. To illustrate the nuclear distributions of the SDs in the yz, zx, and xy planes in Fig. 3.7. As seen from the figure, they both show oblate deformed shapes.

The self-consistent HF solution is assigned to the first SD (number 1). We should note that it does not appear in the top ten components of the ground state. Its overlap value with 0_1^+ is about 0.7. For ^{12}C, the self-consistent HF solution with the SLy4 interaction is spherical with $p_{3/2}$ closed shell configuration. The spherical solution cannot describe the rotational band observed in the measurement. As shown in Fig. 3.2 and Table 3.1, our calculation accurately reproduces the energy levels and the $B(E2)$ transitions among the states of the ground rotational band. This good reproduction is achieved by a superposition of SDs of deformed shapes.

3.7.2 Negative-parity states

In Table 3.4, we show sequential numbers of the SDs which have large overlap values with the wave function of the negative-parity states 3_1^-, 1_1^-, and 2_1^-. We find the 4th SD, which appears in the ground rotational band, also dominates in the negative-parity states. Other SDs which dominate in the negative-parity states are 21, 29, and 47th.

We show the density distributions of these three SDs in Fig. 3.8. All of these SDs have similar oblate shapes with three-α-like structure. A close look at the densities reveals that

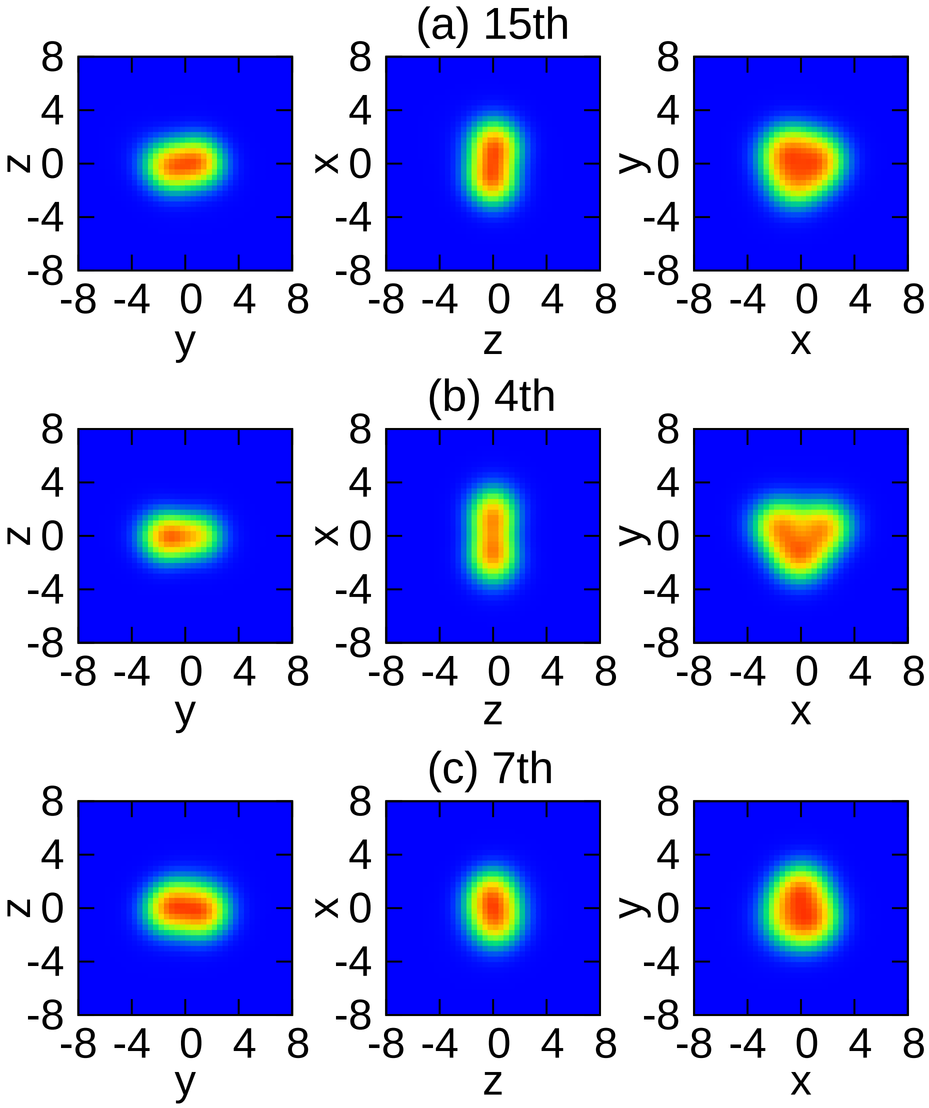

Figure 3.7: Contour plots of the density distributions of the 15th, 4th, and 7th SDs, which are the major components of the ground state rotational band.

the 4th and the 29th SDs have a compact configuration, while the 21th and the 47th SDs show spatially more extended three-α configuration forming an obtuse-angled triangle.

3.7.3 0_2^+, 2_2^+, and 2_3^+ states

In Table. 3.5, we show sequential numbers of the SDs which have large overlap values with the wave function of the state 0_2^+, 2_2^+, and 2_3^+.

We first examine the Hoyle state, 0_2^+. Compared with the cases of the ground rotational

1_1^-			2_1^-			3_1^-			4_1^-		
SD	K	P	SD	K	P	SD	K	P	SD	K	P
4	1	0.77	21	1	0.77	29	3	0.81	29	3	0.79
47	1	0.76	4	1	0.75	4	3	0.81	47	3	0.77
18	1	0.75	47	1	0.72	47	3	0.76	4	3	0.76
21	1	0.75	22	1	0.70	15	3	0.67	25	2	0.66
22	1	0.74	18	1	0.70	21	3	0.64	41	3	0.64
29	1	0.68	29	1	0.70	3	1	0.64	3	3	0.61
11	1	0.67	11	1	0.62	48	3	0.62	5	2	0.60
25	1	0.60	48	1	0.55	9	3	0.61	9	3	0.59
46	1	0.58	46	1	0.54	41	1	0.56	48	3	0.57
33	1	0.57	33	1	0.54	33	3	0.55	21	1	0.55

Table 3.4: The sequential number, the K-value, and the squared overlap value P are shown for the SDs which dominate in the wave function of the negative-parity states 1_1^-, 2_1^-, 3_1^- and 4_1^-.

band and the negative-parity states, the maximum value of the overlap is rather small, less than 0.5. This indicates that the superposition of a large number of SDs is essential to describe the 0_2^+ state. This is consistent with the cluster-model calculations [37, 38] and the picture of the α-condensed state for the 0_2^+ [33].

We show in Fig. 3.9 the density distributions of the SDs which have the largest and second largest overlaps with the 0_2^+ state, namely, the 9th and the 28th SDs. These SDs have well developed cluster structures of three-α-particles.

Regarding the 2_2^+ and the 2_3^+ states, we find that a number of configurations contribute to these states, as in the case of 0_2^+ state. These SDs in 2_2^+ and 2_3^+ states are more or less similar. However, they are very different from those in the 0_2^+ state. This is consistent with our observation that the $B(E2)$ transition strengths between 0_2^+ and 2_2^+ states and between 0_2^+ and 2_3^+ states are rather small (see Sec. 3.4).

3.7.4 Linear-chain states

As seen in Sec. 3.4, 0_3^+, 2_4^+, and 4_2^+ states are connected by the intense $B(E2)$ values. In Table 3.6, the sequential numbers of the SD which have large overlap values with the wave function of these states are shown. The 30th, the 40th and the 19th SDs are commonly included in the three states. We show in Fig. 3.10 the density distributions of the 30th and the 40th SDs. They clearly show a bent linear-chain structure of three-α-parities.

3.8 Mixing of three-alpha configurations

Some of the present results in Sec.3.3, 3.4, and 3.5 are found to be qualitatively different from those of AMD and microscopic cluster models. For example, the radius of the 0_2^+ state is much

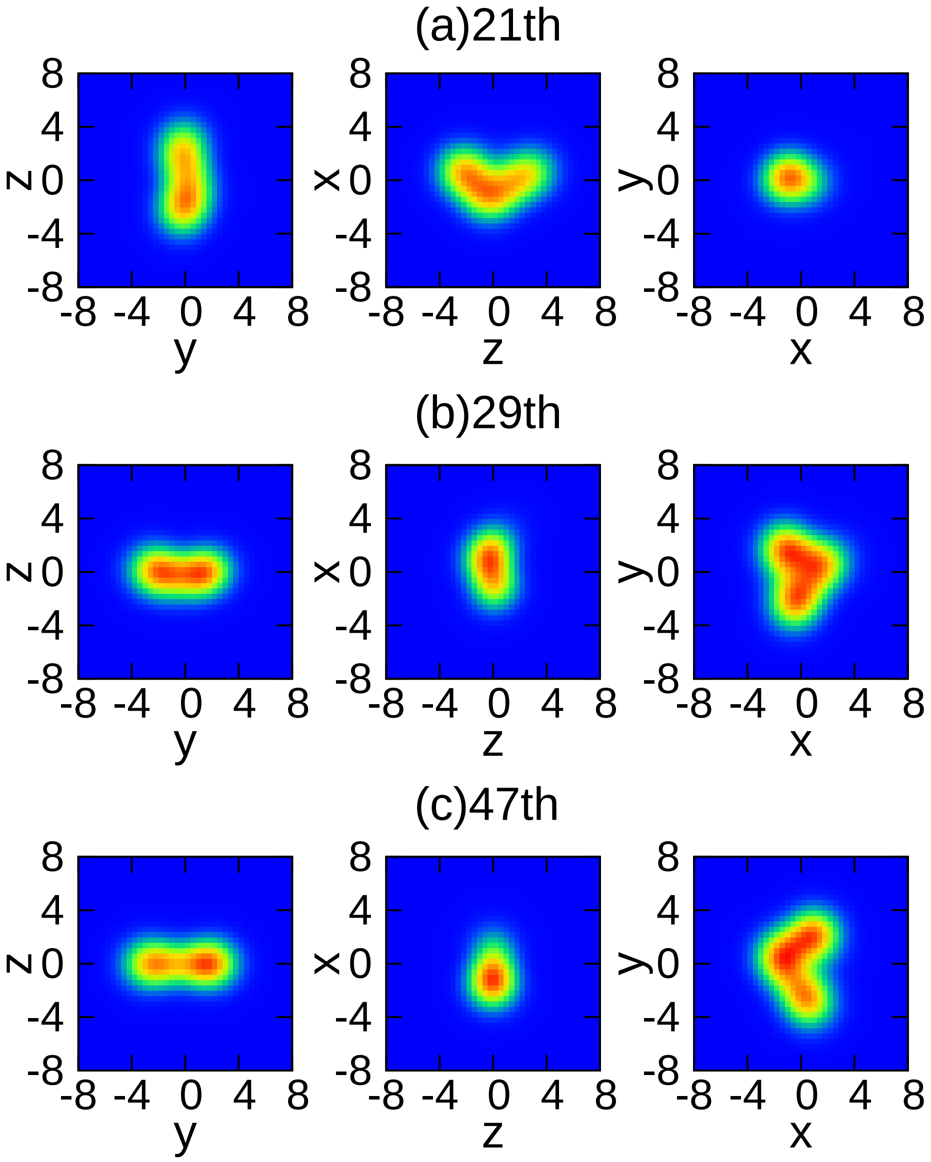

Figure 3.8: Contour plots of the density distributions of the 21th, 29th, and 47th SDs, which are the major components of the negative-parity states 1^1-, 2_1^-, 3_1^-, and 4_1^-.

smaller in our calculation. The charge form factor at large momentum transfer is described much better by other theories than ours. These facts may indicate that the imaginary-time propagation may not sufficiently produce a certain class of α-cluster wave functions.

In order to check whether explicit inclusion of α-cluster configurations brings big changes in the current results, we perform configuration-mixing calculations including the wave functions similar to those employed in the microscopic-cluster-model of Ref. [37].

0_2^+			2_2^+			2_3^+		
SD	K	P	SD	K	P	SD	K	P
9	0	0.46	16	2	0.74	15	2	0.50
28	0	0.45	35	0	0.58	7	2	0.41
3	0	0.41	43	0	0.56	8	2	0.40
5	0	0.39	42	0	0.56	31	0	0.39
33	0	0.39	31	2	0.56	16	0	0.31
11	0	0.36	7	1	0.54	32	0	0.23
47	0	0.35	32	2	0.52	43	2	0.22
26	0	0.34	49	0	0.41	10	2	0.20
45	0	0.33	36	2	0.41	35	2	0.19
41	0	0.32	43	1	0.36	4	2	0.19

Table 3.5: The sequential number, the K-value, and the squared overlap value are shown for the SDs which dominate in the wave function of the 0_2^+, 2_2^+ and 2_3^+.

The 31 SDs of the α-cluster wave functions are used in the GCM calculation in Ref. [37]. We place the α-particle wave functions at the same positions as those of Ref. [37]. In Ref. [37], the single-particle wave functions of the SDs are Gaussian wave packets. Instead of the Gaussian wave packets, we employ the HF orbitals of the α-particles. In Fig. 3.11, we show density distributions of selected SDs among those 31 SDs.

In Fig. 3.13, we show excitation spectra from configuration mixing calculations using the 31 SDs. The left panel shows our calculation using the SLy4 interaction [Fig. 3.13(a)]. The middle panel shows the GCM calculation using Volkov No.I force [37] [Fig. 3.13(b)]. The results for the ground rotational bands are similar to each other. In fact, in both calculations, the moment of inertia is too large. The 0_2^+ state appears at around 7 MeV in our calculation, slightly lower than that of Ref. [37].

In the parentheses in Fig. 3.13, we show the calculated binding energies in the ground state. The absolute values of the binding energies are very different between the result of our calculation and that of Ref. [37]. In our calculation using SLy4 interaction, the binding energy is 75.1 MeV and is much smaller than the value shown in Fig. 3.1. A major part of the difference comes from the spin-orbit interaction which makes a small contribution in the calculation using the α-cluster wave function only.

We next perform a configuration mixing calculation employing both the 50 SDs prepared by the imaginary-time method and the 31 SDs of three-α configuration. In Fig. 3.13, we compare the three calculations: the configuration mixing calculation using 50 SDs prepared by the imaginary time method (IT), the configuration-mixing calculation using 31 SDs three-α configuration (3α), and the configuration-mixing calculation using both (IT+3α). The calculation labelled by three-α is the same as that shown in the left part of Fig. 3.13, except that the total energies are plotted here.

After mixing, both configurations of the imaginary-time and the three-α, we find the results are very close to the calculation using the imaginary-time configurations only. Namely,

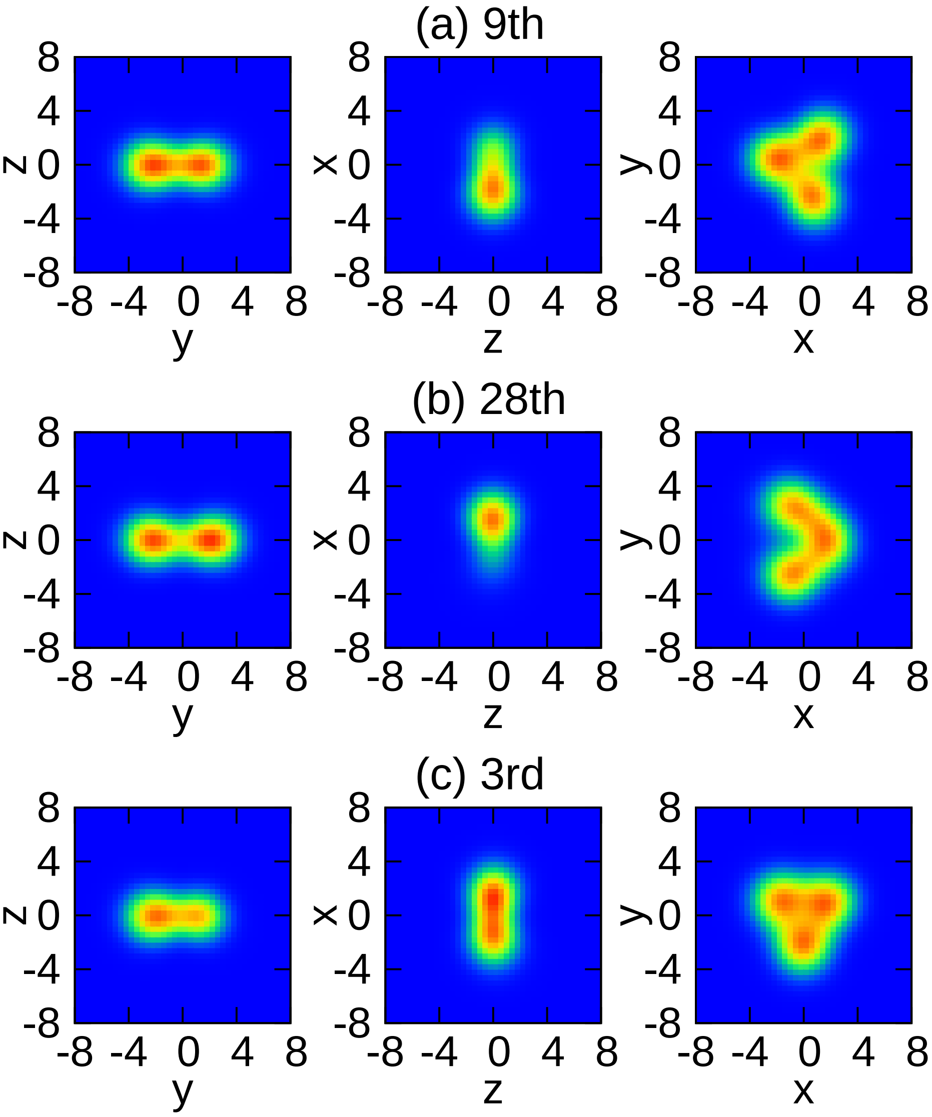

Figure 3.9: Contour plots of the density distributions of the 9th, 28th, and 3rd SDs, which are major components in the 0_2^+ state.

31 SDs of the three-α wave functions do not mix with those prepared by the imaginary-time method. This is due to the large energy difference between those two sets of configurations.

In the calculation using configurations generated by the imaginary-time method, the contribution of the spin-orbit interaction to the binding energy is as large as 17 MeV with SLy4. This large energy gain is missing in the pure three-α configurations.

In Table 3.7, we show the calculated radii and $M(E0)$ transition strengths. Using the 31 SDs of three-α wave functions, our calculation gives large values for both the 0_1^+ and 0_2^+ states. The radius of the 0_2^+ state is 3.31 fm, close to the value by the GCM calculation, 3.4 fm.

0_3^+			2_4^+			4_2^+		
SD	K	P	SD	K	P	SD	K	P
30	0	0.70	40	0	0.78	40	0	0.75
40	0	0.67	30	0	0.72	30	0	0.75
19	0	0.65	19	0	0.71	18	0	0.66
20	0	0.42	18	0	0.68	19	0	0.62
23	0	0.38	11	0	0.59	34	0	0.43
18	0	0.38	23	0	0.58	20	0	0.43
14	0	0.38	12	0	0.48	11	1	0.42
12	0	0.37	34	0	0.47	23	0	0.41
11	0	0.25	22	0	0.39	14	0	0.40
22	0	0.17	20	0	0.39	11	0	0.39

Table 3.6: The sequential number, the K-value, and the squared overlap value P are shown for the SDs which dominate in the wave function of the 0_3^+, 2_4^+ and 4_2^+.

	Expt.	IT	IT + 3α	3α	3α(Uegaki)
radius(0_1^+)	2.31±0.02	2.53	2.54	2.80	2.40
radius(0_2^+)		2.76	2.73	3.31	3.40
$M(E0; 0_2^+ \to 0_1^+)$	5.4± 0.2	4.57	4.13	8.72	6.6

Table 3.7: Radii (fm) and $M(E0)$ ($e$fm^2) calculated in various model spaces. Results of GCM calculation [37] is also shown. See text for details.

The $M(E0)$ value is also large, 8.72 $e$fm^2, even larger than the three-α GCM calculation [37]. However, in the configuration-mixing calculation using both configurations, our calculated values are very close to the calculation using the 50 SDs prepared by the imaginary-time method. This result is consistent with the fact that the energy spectra is very little affected by adding the three-α wave functions.

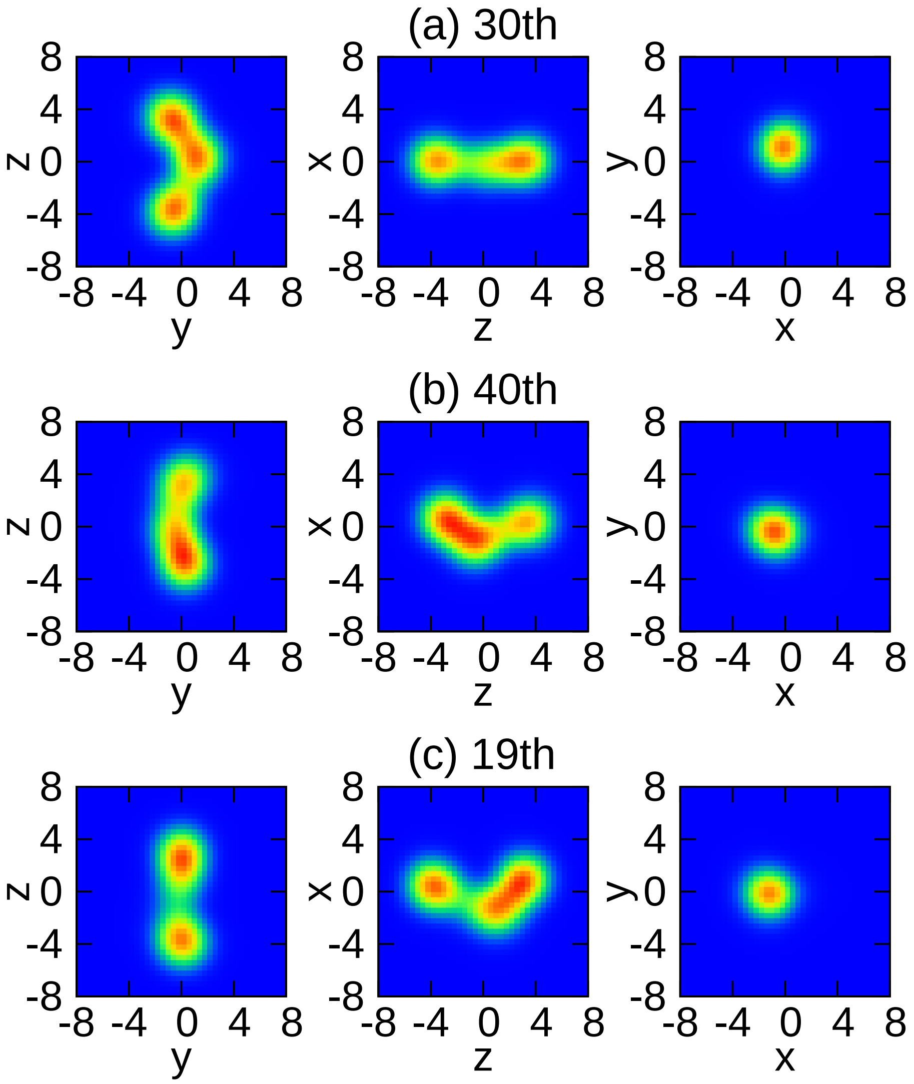

Figure 3.10: Contour plots of the density distributions of the 30th, 40th, and 19th SDs, which are the major components of the 0_3^+, 2_4^+, and 4_2^+ states.

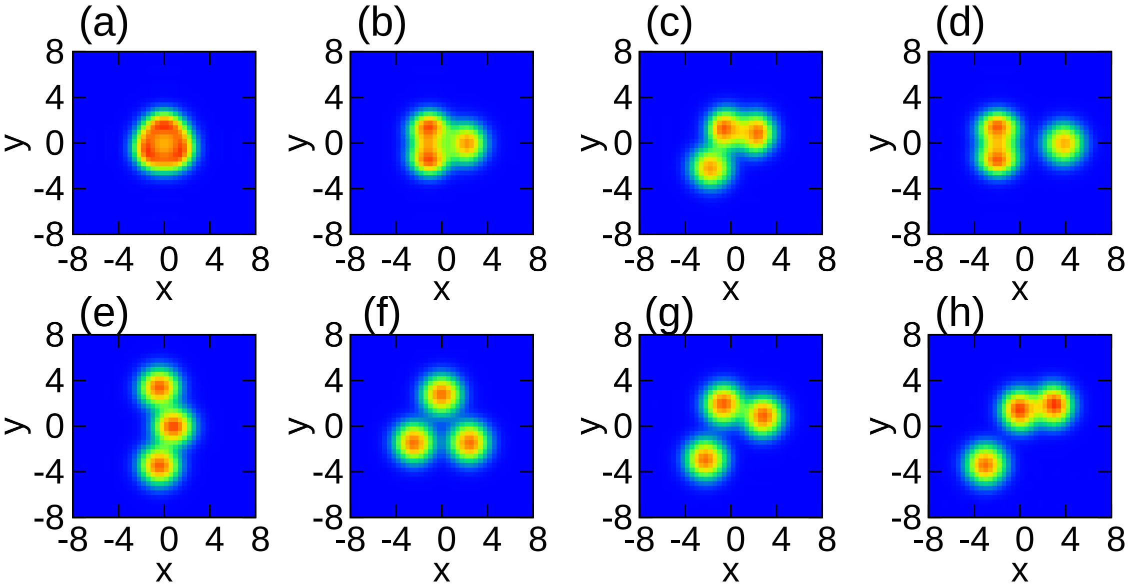

Figure 3.11: Density distributions of some SDs out of 31 SDs which are used in Ref. [37]. Units of vertical and horizontal axes are fm.

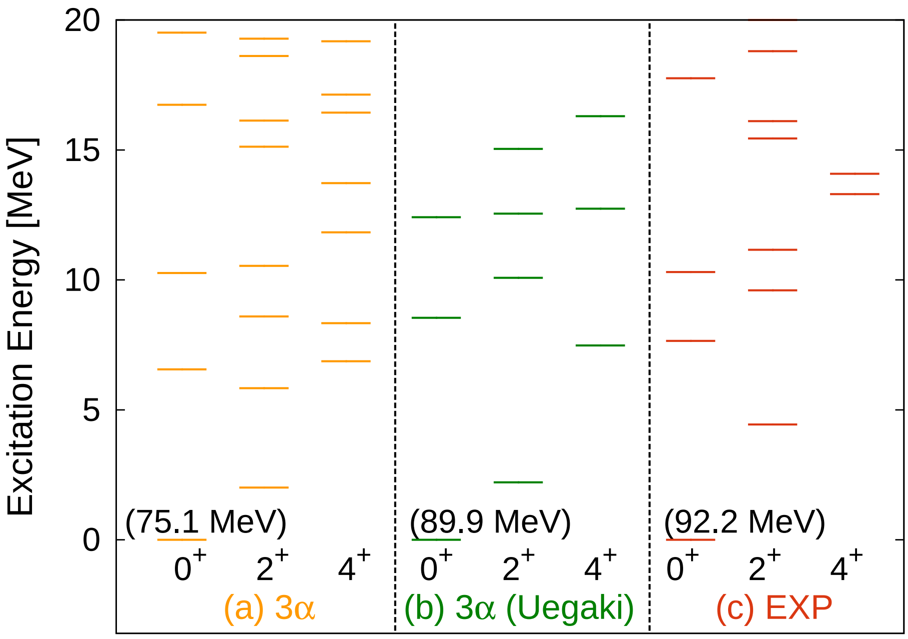

Figure 3.12: Energy levels of ^{12}C employing 3α SDs with Skyrme SLy4 interaction (a), the results of GCM calculation of Ref. [37] (b), and experiments (c).

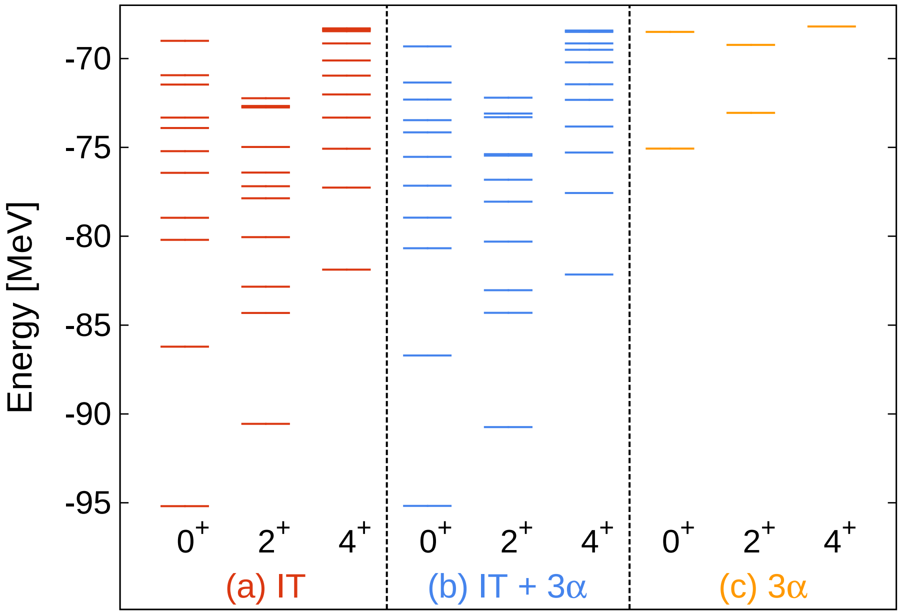

Figure 3.13: Energy levels of ^{12}C in the configuration mixing calculation with the SDs constructed by the imaginary-time evolution (IT), and 3α, and all of these configurations (IT+3α). See text for details.

Chapter 4

Results: ^{16}O

4.1 Structure of ^{16}O

The ^{16}O nucleus is a double magic nucleus and the ground state has a double-closed shell structure. Because of the double-closed shell structure, it is expected that shell model (SM) is appropriate to describe ^{16}O. However, though the lowest excited state is the 0_2^+ state in measurements, SM expects that the lowest excited state is a 1p-1h negative-parity state. Since the excitation energy of the first positive-parity in SM should be at around $2\hbar\omega \approx 30$ MeV if mean-field does not change drastically, 0_2^+ state cannot be understood by the mean-field picture. Because of this reason, the 0_2^+ state has been called 'the mysterious 0^+ state'. In the weak coupling model which assumes that holes and four particles interact weakly, it was argued that the α-particle correlation is important to describe the 0_2^+ state [60]. The model space of SM had been expanded in advanced studies of ^{16}O and $(0+2+4)\hbar\omega$ shell model calculation using all $p-sd$ orbitals was performed [61]. This shell model well reproduced many excited states in ^{16}O. However the gap between $0p_{3/2}$ and $0p_{1/2}$ was adjusted to reproduce the energy spectrum of ^{16}O. In recent year, the shell model calculation for ^{16}O in the full $p-sd$ model space was performed [62]. They argue that shell gap become small due to correlation energy.

Cluster models has been extensively applied to ^{16}O. The OCM has been successful in describing the ground and excited state of ^{16}O [63–65]. However, OCM is not completely microscopic but includes empirical parameters. The RGM and GCM calculations have been achieved as well, though failed to reproduce excitation energy of 0_2^+ state; They estimate the excitation energy about two times higher than the experimental value [66, 67]. Although the OCM, RGM, and GCM assume existence of clusters in advance, the AMD calculation does not assume any clusters [68]. The AMD well reproduces the excitation energies of negative-parity states. However, AMD calculation fails to reproduce the excitation energy of 0_2^+ state at correct position; The calculated excitation energy is about 13 MeV, which is larger than the measured value, 6.05 MeV. In recent years, Funaki and others [69–71] performed the 4-α OCM calculation. They show that 0_6^+ is 4-α particle condensed state which are up to around the four α-cluster threshold at 14.4 MeV.

In the last ten years, the *ab-initio* calculation was performed for ^{16}O. There are NCSM, NCFC, and Coupled-Cluster (CC) calculations [18, 19, 72–79]. However, the most calculations are only applied to the ground state of ^{16}O; only a few model calculations are performed for the excited states of ^{16}O. These calculations cannot reproduce the excitation energy of 0_2^+ state. In the NCFC calculation [19] with JISP-16, the excitation energy of 0_2^+ is about 13 MeV, which is two times larger than the measured value, 6.05 MeV. In the CC calculation [75], the excitation energy of 0_2^+ is also two times larger than the measured value.

4.2 Convergence of results: Statistical treatment

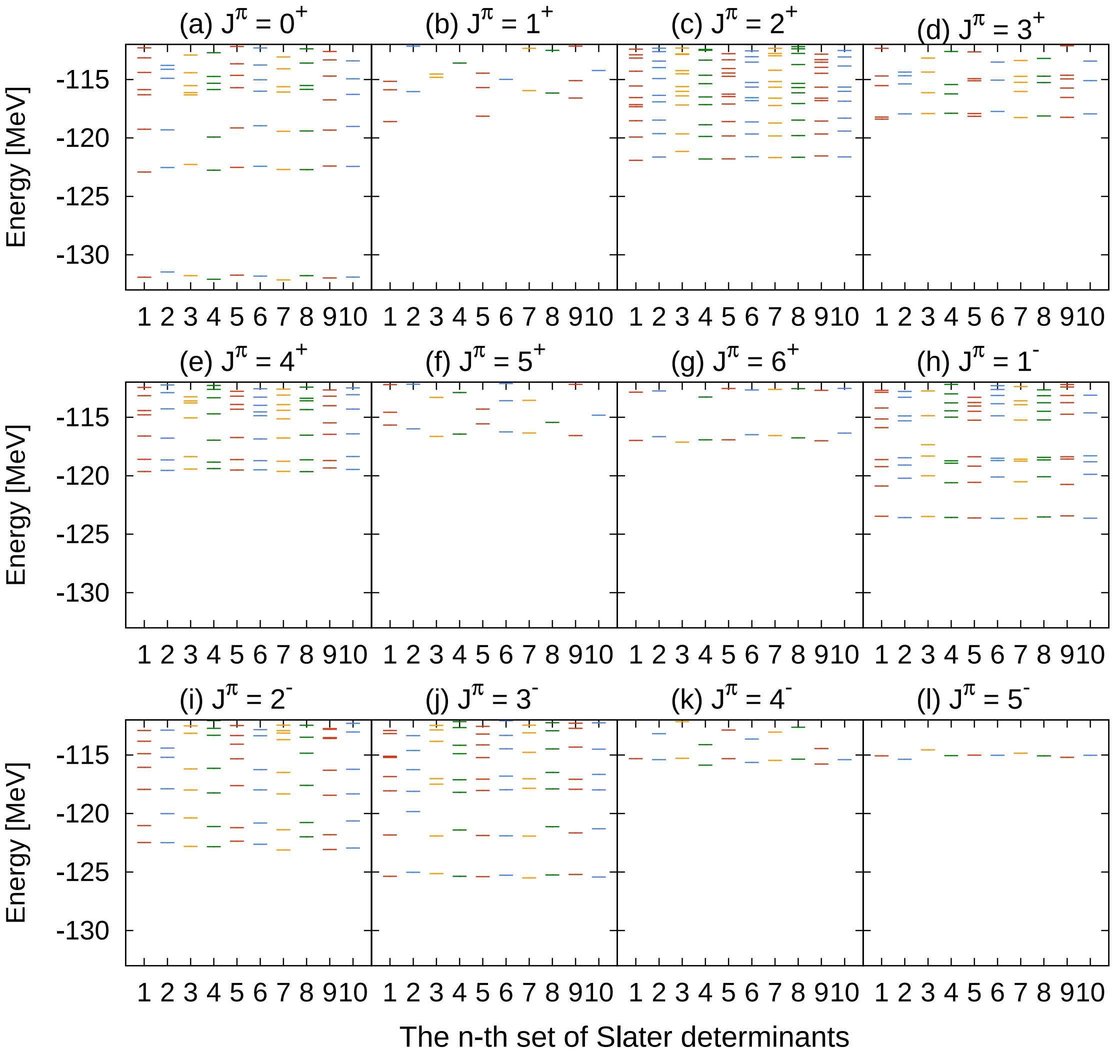

Figure 4.1: Energy levels of the ^{16}O nucleus for $J^\pi = 0^+, 1^+, 2^+, 3^+, 4^+, 5^+, 6^+, 1^-, 2^-, 3^-, 4^-$ and 5^-. Calculations employing ten different sets of SDs are shown. See the text for details.

In this section, we examine the convergence of the energy levels for ^{16}O in the same method as Sec. 3.2. We prepare ten sets of the SDs and calculate energy levels for each set. If the calculated energy levels are close to each other among the ten different sets of SDs, one may conclude that the calculated energy levels are reliable. These ten sets of SDs are composed of 50 SDs, which are prepared in the procedure explained in Sec. 2.2. Different seeds for the random numbers, which are used to prepare initial states in Eq. (2.2.1), are employed to generate the different sets.

In Fig. 4.1, we show the energy levels of the ^{16}O nucleus for the ten sets calculated in the procedure explained in Sec. 2.2. The energy levels are shown for $J^\pi = 0^+$, 1^+, 2^+, 3^+, 4^+, 5^+, 6^+, 1^-, 2^-, 3^-, 4^-, and 5^-.

First, we examine the calculated energy levels of $J^\pi = 0^+$ in Fig. 4.1(a). The lowest energy level is located around -132 MeV. The variation of energy levels among ten sets is less than 0.5 MeV. The second excited state appears around -123 MeV. The difference of energies among ten sets is again less than 0.5 MeV. Since the variation is rather small, we may state that the energies of these two lowest states are calculated reliably. However, the energies of third excited state do not show a good converge. The third excited state of the third set appears around -117 MeV, although the energy levels of the others sets give the energy at -119 MeV. We thus conclude that we can obtain reliable excitation energies and wave functions for the lowest two levels for $J^\pi = 0^+$ and the third level might be located around -119 MeV.

The energy levels of $J^\pi = 2^+$ and 4^+ in Figs. 4.1(c) and 4.1(e) indicate that the energies of the lowest two states are reliable with a small deviation. The third energy level of $J^\pi = 2^+$ and 4^+ of the third set is located above that of the other sets. This situation is same as the $J^\pi = 0^+$ case. For $J^\pi = 3^+$, 5^+, and 6^+ states [Figs. 4.1(d), 4.1(f), and 4.1(g)], the lowest state may be reliable. However, the calculated energies of $J^\pi = 1^+$ states show strong variation among the ten sets even for the lowest states [Fig. 4.1(b)]. The same circumstance can be seen the energy levels of ^{12}C in Fig. 3.1.

For $J^\pi = 1^-$, 2^-, and 3^- states, the lowest two states are small variation among ten sets [Figs. 4.1(h)-(j)]. For the $J^\pi = 4^-$ and 5^- states, only the lowest state is small variation [Figs. 4.1 (k) and (l)]. We then conclude that, for the negative-parity levels, the lowest two states may be reliable for $J^\pi = 1^-$, 2^-, and 3^- states [Figs. 4.1(h) and 4.1(i)], and only the lowest state is reliable for $J^\pi = 4^-$ and 5^- states [Figs. 4.1(k) and 4.1(l)]. As in the results for ^{12}C, we calculate statistical averages and standard deviations among the ten sets for physical quantities for ^{16}O.

4.3 Energy levels

We show calculated excitation spectra of positive- and negative-parities in Figs. 4.2 and 4.3, respectively. In the figures, average value of energies over ten sets are shown with error bars as the standard deviation. The error bars only show the lowest four states to make it easier to look. Our calculated results are compare with measurement [80] and other theories, AMD [68], OCM [63], and SM [61]. The basis of AMD calculation is generated by energy variation constrained to matter quadrupole deformation parameter β. The OCM is α+^{12}C cluster

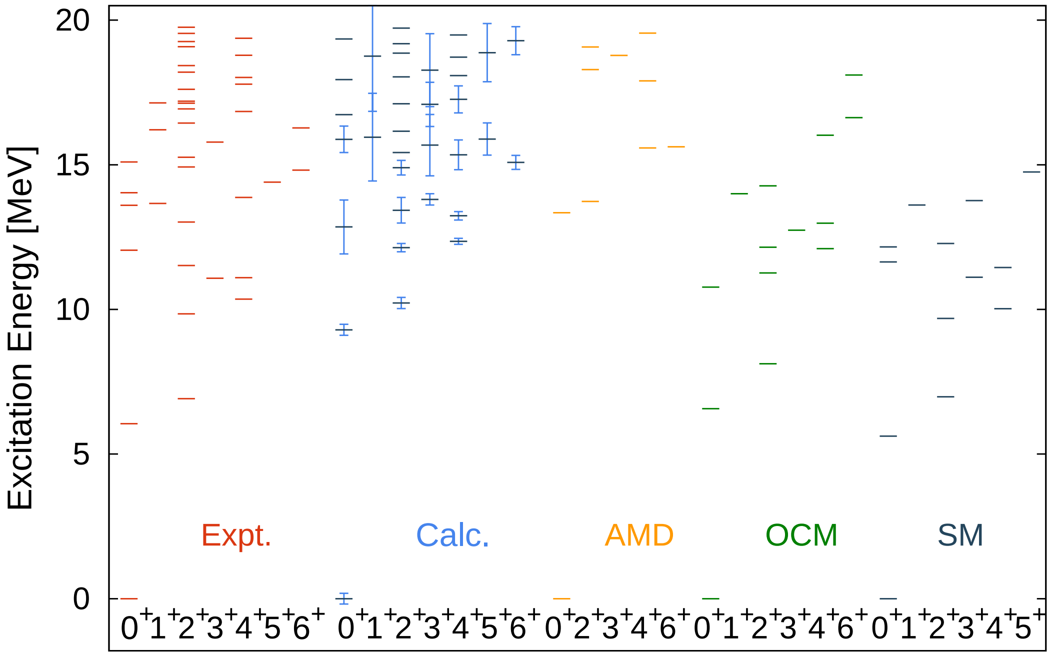

Figure 4.2: Excitation energies of positive-parity for ^{16}O are shown. The energies are obtained by averaging over ten configurations. The standard deviations of the energies are also shown by error bars. The error bars only show the lowest four states. We also show the results of AMD [68], α+^{12}C OCM [63], and SM [61] from left to right. Experimental data are taken from Refs. [80]. See the text for details.

coupling model, in which 0^+, 2^+, and 4^+ states of ^{12}C are coupled with the relative motion between α and ^{12}C. The SM is full non-spurious $(0 + 2 + 4)\hbar\omega$ shell model.

In the Skyrme-HF calculation, the binding energy of ^{16}O is 128.49 MeV, which is good agreement with the measured value, 131.86±0.20 MeV. In our configuration mixing calculation, the correlation energy is 4.7±0.2 MeV. The ground-state energy including the correlation is 131.86±0.20 MeV. The difference between the ground-state energy after configuration-mixing and that of measured value may be improved by readjustment of the Skyrme parameter set.

In Fig. 4.2, four states 0^+_2, 2^+_1, 4^+_2, and 6^+_2, follow a rotational energy sequence. Small standard deviations of the energies of these states indicate the reliability of the calculation. As will be discussed in Sec. 4.4, these states are connected by strong $B(E2)$ transitions. In Sec. 4.7, we will show that this band corresponds to α+^{12}C cluster state. Unlike present results, the 0^+_2, 2^+_1, 4^+_1, 6^+_1 states follow a rotational energy sequence by OCM. The difference in order of levels in OCM and present calculations can be also seen in AMD; the 4^+_2 state belong to the rotational band in AMD.

The calculated excitation energy of 0^+_2 state is about 9 MeV, which is about 3 MeV larger than the experimental value, 6.0494±0.0010 MeV. The excitation energy of 0^+_2 stat is well

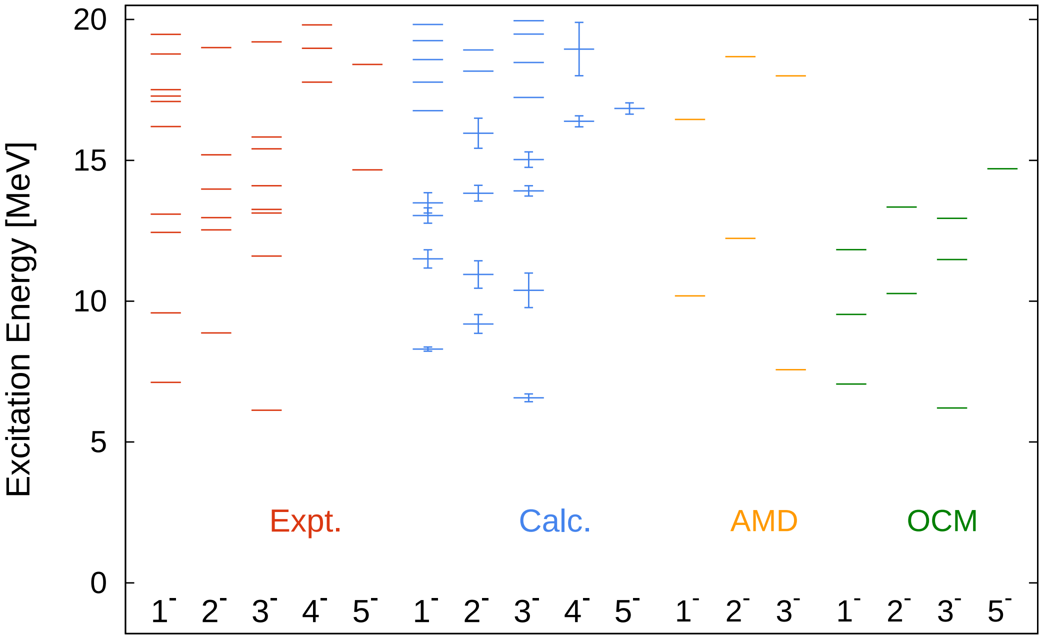

Figure 4.3: Excitation energies of negative-parity for ^{16}O are shown. The same explanation as that in Fig. 4.2 applies to others.

reproduced by the OCM and SM. However, the OCM and SM contains empirical parameters specific to ^{16}O. Namely in the OCM a potential strength is determined to adjust to fit the energy levels, and in the SM, four single-particle energy splittings are determined by a direct fitting to the energy levels. Although the present and AMD is no empirical parameters specific to ^{16}O, the present and AMD provide too high excitation energies. However, our calculated excitation energy of 0_2^+ state is much better than that of AMD.

In recent years, Funaki and others [69–71] performed the 4-α OCM calculation, and indicate that 0_6^+ is α-particle condensed state which are up to around the four α-cluster threshold at 14.4 MeV. However, the present calculation do not give a converged solution for the 0_6^+.

For the negative-parity state, we have obtained solid results for the lowest energy state for each J^π sector (Sec. 4.2). The excitation energies of lowest 1^-, 2^-, 3^-, and 4^- states overestimate the experimental data. On the contrary, 5^- state underestimate the experimental data. The excitation energies for lowest states are more reasonable than the AMD calculations.

Finally we mention how the calculated energy levels depend on interactions. In Figs. 4.4 and 4.5 we show the excitation energies of positive- and negative-parity states with different sets of the Skyrme interaction, SLy4, SGII, SIII, and SkM*, and Gogny D1S interaction. The same set of SDs is employed in all calculations. The correlation energies in the ground states are shown as well inside the parentheses. The comparison shows that the excitation energies of Skyrme SkM* is different from that of the other forces; The energy levels of Skyrme SkM*

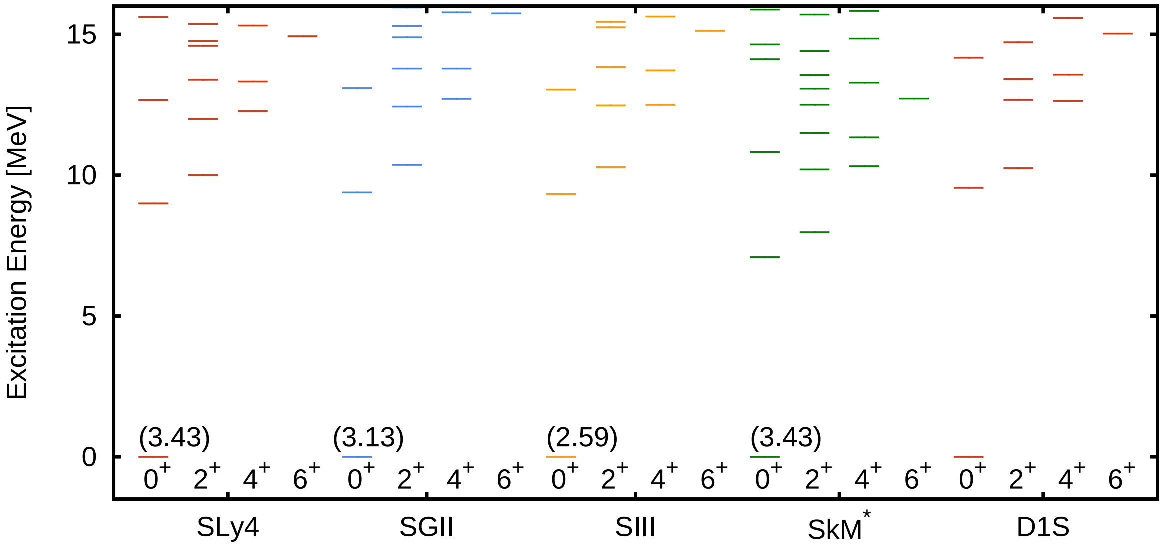

Figure 4.4: Energy levels of positive-parity for ^{16}O employing different parameter sets of Skyrme forces, SLy4, SkM* and SIII, and Gogny D1S force. The number in parentheses is the correlation energy in the ground state, $E_{\rm HF} - E_{\rm gs}$, in unit of MeV. In the calculation, the same set of SDs is employed.

is much higher than that of any other forces, although the level spaces between each levels in excited states are almost the same when comparing the excitation spectra of all forces. The reasons for the difference outcome between Skyrme SkM* and the other forces are not clear. We conclude that the level spaces in excited states do not sensitive to choice of interaction for almost all, although excitation energies from the ground state may change to choice of interaction.

4.4 Transition strength

Calculated $B(E2)$, $B(E3)$, and $M(E0)$ values for ^{16}O, the average values and the standard deviations, are shown in Table 4.1. We do not employ any effective charges in our calculated values. The order of magnitude of $B(E2)$ transition strength between 2_1^+ and 0_1^+ is good agreement with the measured value by our approach, AMD, and SM, although the magnitude of transition strength between 2_1^+ and 0_1^+ is underestimated.

The calculated transition strength of $B(E2; 2_1^+ \to 0_2^+)$ and $B(E2; 4_1^+ \to 2_1^+)$ which have the α+^{12}C structure is lower than the measured value. This underestimation of transition strengths is also seen AMD and OCM calculations, although the values of the OCM calculation is more reasonable. In the AMD calculation, 4_1 and 4_3^+ correspond to 4_2 and 4_1^+ in experiment data. The 4_2^+ state did not identify the state of measured value. The underestimation of the AMD calculation is primarily due to fragment of $E2$ transition strengths for $B(E2; 4_2^+ \to 2_1^+)$, $B(E2; 4_3^+ \to 2_2^+)$, and $B(E2; 2_2^+ \to 0_2^+)$. The values cal-

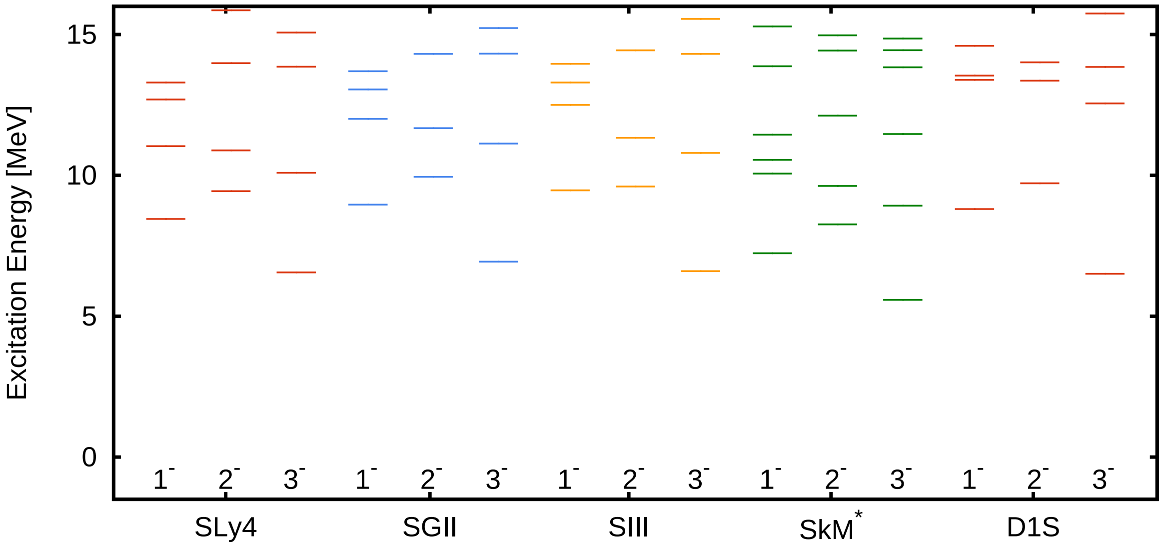

Figure 4.5: Energy levels of negative-parity for ^{16}O employing different parameter sets of Skyrme force, SLy4, SkM* and SIII, and Gogny D1S force. In the calculation, the same set of SDs is employed.

culated by the AMD are $B(E2; 4_2^+ \to 2_1^+) = 21e^2\mathrm{fm}^4$, $B(E2; 4_3^+ \to 2_2^+) = 49e^2\mathrm{fm}^4$, and $B(E2; 2_2^+ \to 0_2^+) = 21e^2\mathrm{fm}^4$. This fragmentation can also see in the present calculation. The $B(E2; 2_2^+ \to 0_2^+)$, $B(E2; 4_2^+ \to 2_2^+)$, and $B(E2; 4_3^+ \to 2_1^+)$ have large values in our calculation. As will be mentioned at Sec. 4.7, the calculated 6_2^+ also have the α+^{12}C structure. In fact, the transition strength of $B(E2; 6_2^+ \to 4_2^+)$ is very large. The $B(E2; 2_2^+ \to 0_1^+)$, $B(E2; 2_3^+ \to 0_1^+)$, and $B(E2; 2_3^+ \to 0_2^+)$ is well reproduced the measurements.

The calculated $B(E2; 1_1^- \to 3_1^-)$, $B(E2; 2_1^- \to 3_1^-)$, and $B(E2; 2_1^- \to 1_1^-)$ underestimate the measurements in all of the methods. The present values are larger than the values of the AMD, and smaller than the values of the OCM. The 1_3^- and 3_3^- states are considered a parity-doublet partner of the ground state as we will discuss later in Sec. 4.7. The transition strengths between these states are rather large. The $E3$ transition between 3_1^- and 0_1^+ is in good agreement with the experimental data. However, the OCM provide too small transition strength.

Calculated $M(E0)$ values, the average values and the standard deviations, are shown in Table 4.2. Calculated $M(E0; 0_1^+ \to 0_2^+)$ is slightly larger than the measured value. On the other hand, this value is slightly underestimated by the 4-α OCM and α+^{12}C. The measured value is between the two. The $M(E0; 0_1^+ \to 0_3^+)$ is rather small, although the standard deviation is rather large. All calculated $M(E0; 0_1^+ \to 0_3^+)$ is smaller than the measured value. As mentioned in Sec. 4.3, it is argue that 0_6^+ state is candidate for α-particles condensed state in [69–71]. In the Refs. [69–71], calculated $M(E0; 0_1^+ \to 0_6^+)$ is rather small, about 1 $e\mathrm{fm}^2$. However, our calculation does not provide solid solution for 0_6^+ (Sec. 4.2).

Transitions	Expt.	Calc.	AMD	α+^{12}C OCM
$B(E2; 2_1^+ \to 0_1^+)$	7.4 ± 0.2	3.4±0.3	4.2	2.20
$B(E2; 2_1^+ \to 0_2^+)$	65 ± 7	50±8	40	60.2
$B(E2; 2_2^+ \to 0_1^+)$	0.074±0.007	0.072±0.14	1.0	0.247
$B(E2; 2_2^+ \to 0_2^+)$	2.9±0.7	7.0±0.8	21	9.68
$B(E2; 4_1^+ \to 2_1^+)$	156±14	5.7±3.3	9.1	102
$B(E2; 4_2^+ \to 2_1^+)$	2.4 ± 0.7	45±11	21	
$B(E2; 4_1^+ \to 2_2^+)$		14.5±2.8		
$B(E2; 4_3^+ \to 2_1^+)$		25±5	29	
$B(E2; 2_3^+ \to 0_1^+)$	3.6 ± 1.2	1.9±0.6	0.65	1.21
$B(E2; 2_3^+ \to 0_2^+)$	7.4 ± 1.2	7.3±2.4	1.6	1.20
$B(E2; 6_1^+ \to 4_1^+)$		14±5		67.1
$B(E2; 6_1^+ \to 4_2^+)$		7.5±2.7		45.1
$B(E2; 6_2^+ \to 4_1^+)$		3.9±3.9		80.8
$B(E2; 6_2^+ \to 4_2^+)$		53±21		14.3
$B(E2; 1_1^- \to 3_1^-)$	50 ± 12	31±1	20	25.5
$B(E2; 2_1^- \to 3_1^-)$	19.6 ± 1.7	8.5±1.3	4.2	13.8
$B(E2; 2_1^- \to 1_1^-)$	24.7±3.6	6.6±2.0	3.1	15.1
$B(E2; 3_3^- \to 1_3^-)$		34±11		
$B(E3; 3_1^- \to 0_1^+)$	205 ± 11	175±9		29.6

Table 4.1: The $B(E2)$ and $B(E3)$ values of ^{16}O in units of e^2fm^4 e^2fm^6 respectively. Experimental and calculated values are shown in first and second column, respectively. For comparison, we show the results of AMD [68] and α+^{12}C OCM [63]. Our 4_1^+ and 4_2^+ states correspond with 4_2^+ and 4_1^+ states in the measurement. The same can be said of 6_1^+ and 6_2^+ states. The 4_3^+ and 4_1^+ states in AMD correspond with 4_1^+ and 4_2^+ states in the experimental data. Experimental data are taken from [80].

4.5 Radii

We next examine rms radii of the ground and excited states for ^{16}O. For comparison, results of 4-α OCM [69], THSR [70], and α+^{12}C OCM [63] are shown. As mentioned in Sec. 3.5, our wave function does not allow an exact separation of the center-of-mass motion from the internal one. We therefore estimate an approximate correction for the radius due to the center-of-mass motion, and subtract it from the calculated values. In addition to correction of center-of-mass motion, we take into account proton size effect. The corrections of center-of-mass motion and proton size effect cancel each other for the opposite sign. The calculated radii after the corrections are shown in Table 4.3.

Our calculated value in the ground state is 2.84 ± 0.007 fm. This value is somewhat larger than that of the measured value, 2.710 ± 0.015 fm. In the HF calculation, the radius is given by 2.74 fm, which is in good agreement with measured value. Our configuration-mixing calculation, therefore, slightly increases the radius. The 4-α OCM reproduces the

transitions	Expt.	Calc.	4-α OCM	THSR	α+^{12}C OCM
$M(E0;0_1^+ \to 0_2^+)$	3.55 ± 0.21	2.97 ± 0.15	3.9	9.8	3.88
$M(E0;0_1^+ \to 0_3^+)$	4.03 ± 0.09	2.59 ± 1.77	2.4		3.50

Table 4.2: The $M(E0)$ values of ^{16}O in units of $e$fm^2. Experimental and calculated are in shown in the first and second column, respectively. For comparison, we show the 4-α OCM [69], THSR [70], and α+^{12}C OCM [63].

J^π	Calc.	4-α OCM	THSR	α+^{12}C OCM
0_1^+	2.91 ± 0.005	2.7	2.5	2.5
0_2^+	3.14 ± 0.03	3.0	3.1	2.9
0_3^+	3.10 ± 0.02	3.1		2.8

Table 4.3: The charge radii of the ground and excited state of ^{16}O. For comparison, we show the results of 4-α OCM [69], THSR [70], and α+^{12}C OCM [63]. The experimental radius of ground state is 2.710±0.015 fm [81].

measurements. The radius of the ground-state is somewhat smaller than the measured value by THSR and α+^{12}C OCM.

For the 0_2^+ state, our calculated radius is 3.14 ± 0.03 fm, which is slightly larger than the radius of the ground state. The other theories also predict small expansion of radius from ground state. For the 0_3^+ state, our calculated radius is 3.10 ± 0.02 fm, which is almost same as the radius of 0_2^+ states. Comparing with other theories, our value is larger than those of α+^{12}C OCM, and is comparable to the value of 4-α OCM.

As mentioned in Secs. 4.3 and 4.4, the 0_6^+ state is thought to composed of a gas of weakly interacting α-particles of the condensate type [69–71]. In the Refs. [69–71], the radius of 0_6^+ is more than 5 fm, which is the largest in radii of 0_4^+, 0_5^+, and 0_6^+. However, our approach does not give a converged solution of 0_6^+ state as shown in the Sec. 4.2.

4.6 Charge form factors

We show the charge form factors for elastic and inelastic $0_1^+ \to 0_2^+$ processes of ^{16}O in Fig. 4.6. We correct the center-of-mass and proton size effect in the same evaluation of charge factor for ^{12}C in Sec. 3.6. Both effects cancel each other. We also show that of Skyrme HF solution in the ground state.

In the small momentum transfer region $q < 2\text{fm}^{-1}$, the elastic form factor is nearly well reproduced by the calculation. In the high momentum transfer region $q > 2\text{fm}^{-1}$, the elastic form factor is underestimated. This underestimation is also seen in the ^{12}C [31]. However, the form factor for the HF state is larger than that for the 50 SDs in ^{12}C, which do not same as the present result for ^{16}O. The reason of the discrepancy of charge form factor in

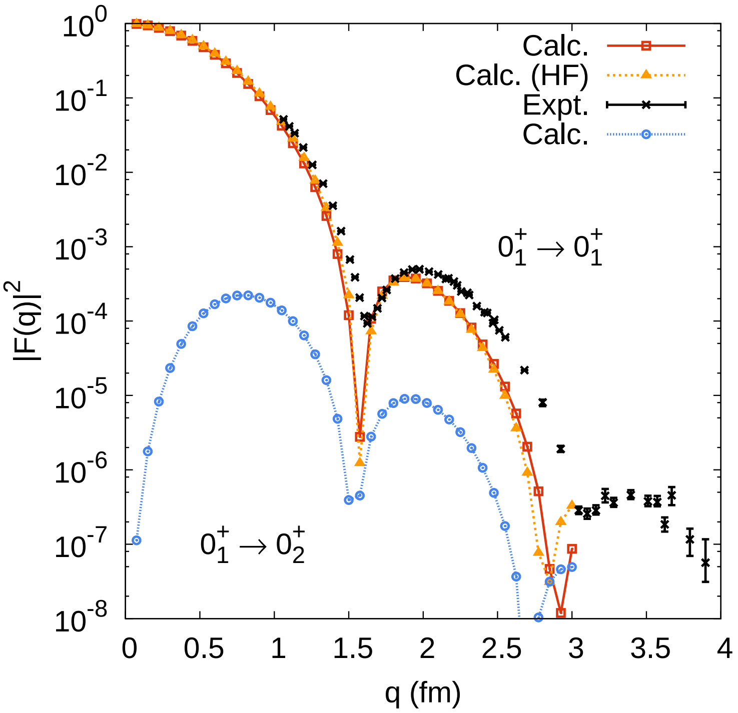

Figure 4.6: Squared elastic form factor for the ground state and $0_1^+ \rightarrow 0_2^+$ inelastic form factor are shown. Our calculated results are compared with the HF calculation with a single SD and measurements [53]. Here, the results using the first set of SDs in Fig. 4.1 are used.

$q > 2\text{fm}^{-1}$ is not clear. The interaction might not be good. The inelastic $0_1^+ \rightarrow 0_2^+$ form factor has two peak around $q = 0.7$ and 1.8 fm. The dip position around $q = 1.5$ fm of inelastic form factor is slightly smaller than that of elastic form factor.

4.7 Analysis of wave functions

We discussed what kinds of correlations include in the wave function after configuration mixing. We calculate overlaps between the energy eigenstate and projected SDs as Eq. (3.7.1). We show the density distributions of the SDs to see the correlations included mainly. In the following, we use the sequential number of the SDs which indicates the adopted ordering in Sec. 2.2. The 1st SD is the HF ground state.

4.7.1 The ground state and $K^\pi = 0^\pm$ bands

In Table 4.4, we show the sequential number of the SDs which have large overlap values with the wave function of the states, $0_1^+, 2_1^+, 4_2^+, 6_2^+, 1_3^-$, and 3_3^-. The overlap values $P_n^{J\pi,iK}$ which is defined as Eq. (3.7.1) and K values are shown. Since the SDs are nonorthogonal, the sum of the overlap is not unity.

0_2^+			2_1^+			4_2^+			6_2^+		
SD	K	P	SD	K	P	SD	K	P	SD	K	P
31	0	0.66	4	0	0.69	14	0	0.70	31	0	0.78
14	0	0.64	14	0	0.69	13	0	0.69	14	0	0.72
4	0	0.63	42	0	0.68	42	0	0.66	42	0	0.68
42	0	0.63	46	0	0.66	45	0	0.53	4	0	0.63
46	0	0.56	45	0	0.61	46	0	0.50	46	0	0.52
37	0	0.55	31	0	0.60	31	0	0.45	32	0	0.48
32	0	0.43	13	0	0.59	4	0	0.39	45	0	0.45
15	0	0.39	3	0	0.57	15	0	0.37	15	0	0.42
5	0	0.39	37	0	0.57	6	4	0.36	34	0	0.41
24	0	0.38	24	0	0.56	20	0	0.35	5	0	0.34

1_3^-			3_3^-			0_1^+		
SD	K	P	SD	K	P	SD	K	P
31	0	0.67	4	0	0.49	8	0	0.94
4	0	0.62	31	1	0.45	50	0	0.94
37	0	0.59	31	0	0.44	6	0	0.93
46	0	0.56	37	0	0.44	26	0	0.93
32	0	0.46	42	1	0.39	11	0	0.93
14	0	0.41	4	1	0.38	18	0	0.92
24	0	0.40	14	1	0.37	20	0	0.91
5	0	0.40	46	1	0.35	17	0	0.91
42	0	0.37	42	0	0.31	47	0	0.90
13	0	0.29	5	0	0.29	30	0	0.90

Table 4.4: The SDs which dominate in the ground and $K^\pi = 0^+$ and 0^- bands, the K value, and the squared overlap between each SD and the wave function after configuration mixing are shown.

In 0_1^+ state, many SDs have large overlap. The HF state, which corresponds to first SD, has 0.81 for the overlap value in this state. As will be noted from the Table 4.4, many SDs have rather large overlap more than 0.9, and the HF state is not in the top 10 of the component of 0_1^+. In order to illustrate the nuclear shape of SDs which are large components of 0_1^+ state, we show the contour plots of the density distributions of these SDs in yz, zx and xy planes in Fig. 4.7. As seen from the figure, the ground state 0_1^+ show the slightly deformed shapes. The 0_1^+ state has different structure from the Skyrme HF state which show a spherical structure.

In Sec. 4.4, we showed that 0_2^+, 2_1^+, 4_2^+, and 6_2^+ are connected by the strong $B(E2)$ values. We find the 31th SD has the largest overlap in 0_2^+ and 6_2^+ states and 14th SD is the second largest. In 2_1^+ state, 4th SD is the largest component and the 14th SD is the second largest. In 4_2^+ state, 14th SD is the largest component. As we show in Table 4.1, the $B(E2; 3_3^- \rightarrow 1_3^-)$

1_1^-			2_1^-			3_1^-		
SD	K	P	SD	K	P	SD	K	P
8	0	0.81	2	1	0.87	6	3	0.90
6	0	0.81	6	2	0.72	6	2	0.90
20	1	0.77	18	1	0.66	6	0	0.88
26	1	0.74	6	0	0.65	2	1	0.87
18	1	0.73	20	1	0.65	26	0	0.87
2	1	0.73	11	0	0.63	2	0	0.86
6	1	0.71	26	1	0.62	50	0	0.83
50	0	0.71	26	0	0.61	26	1	0.81
17	1	0.70	8	0	0.61	33	0	0.81
26	0	0.70	3	1	0.61	20	1	0.81

Table 4.5: The SDs which dominate in the lowest negative-parity states, the K value, and the squared overlap between each SD and the wave function after configuration mixing are shown.

value is strong. The 1_3^- and 3_3^- states also have large overlap with 31th and 4th SDs which are also large component with $0_2^+, 2_1^+, 4_2^+$, and 6_2^+ states. We show the contour plots of the density distributions of 31th, 4th, and 14th SDs in Fig. 4.8. All of these SDs have the α+^{12}C structure. The 31th and 4th SDs show a prominent cluster structure and 14th SD show a slightly broken cluster structure. The 14th SD have large overlap over 0.6 to positive-states, 0_2^+, 2_1^+, 4_2^+, and 6_2^+, though the 14th SD have small overlap about 0.4 to negative-parity state, 1_3^- and 3_3^-.

4.7.2 The particle-hole excitation states

In Table 4.5, we show the sequential numbers of the SDs which have large overlap values with the wave function of the negative-parity states 1_1^-, 2_1^-, and 3_1^-, which are known to be particle-hole excitations. We find the 6th SD dominates in the negative-parity. The 6th and 8th are large component in the ground state. The 2nd SD is the largest component in the 2_1^- state. We show the density distributions of these three SDs in Figs. 4.7 and 4.9. All of these SDs have similar deformed shape.

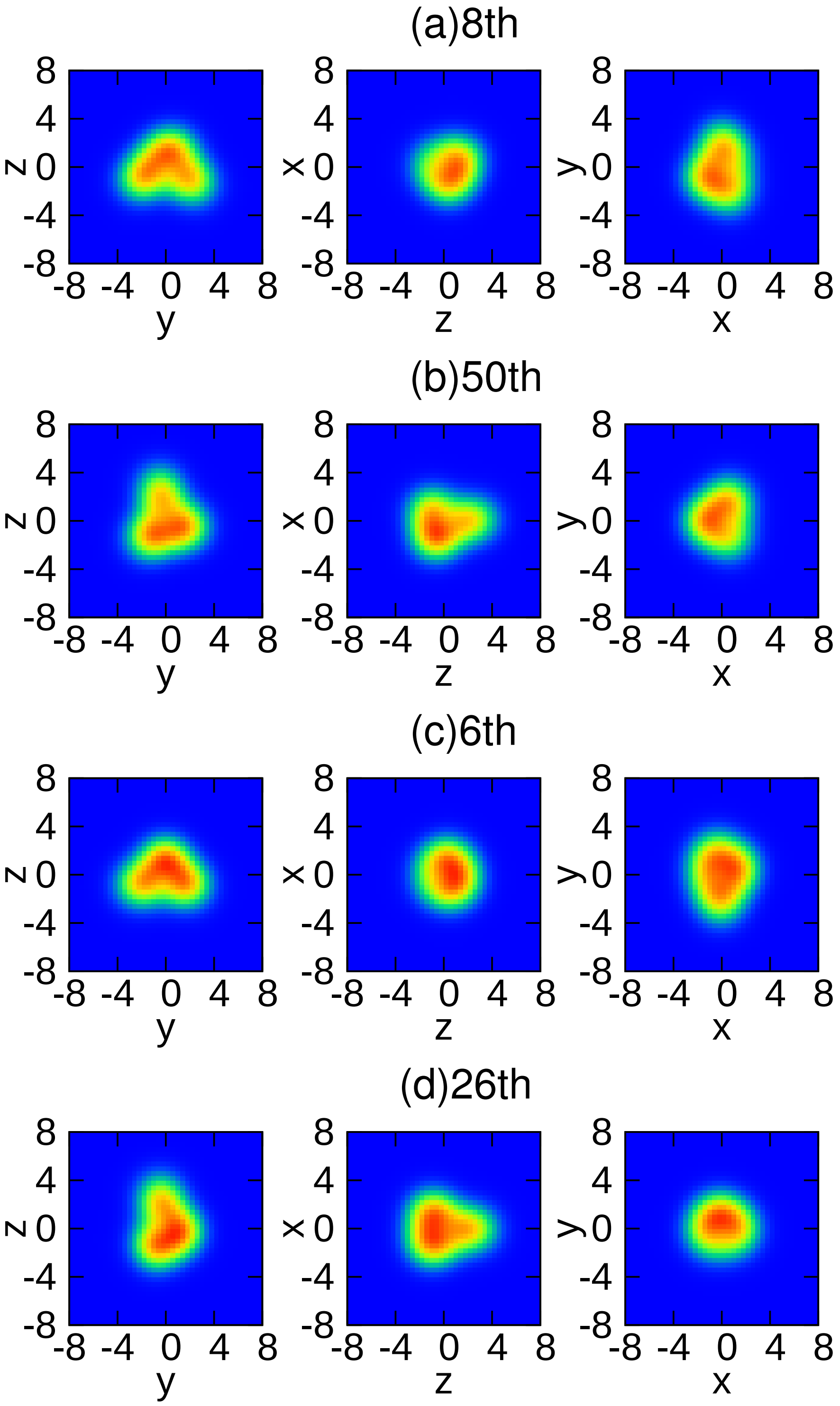

Figure 4.7: Contour plots of the density distribution of the 8th, 50th, 6th, and 26th SDs, which are major components of the ground state 0_1^+ for ^{16}O.

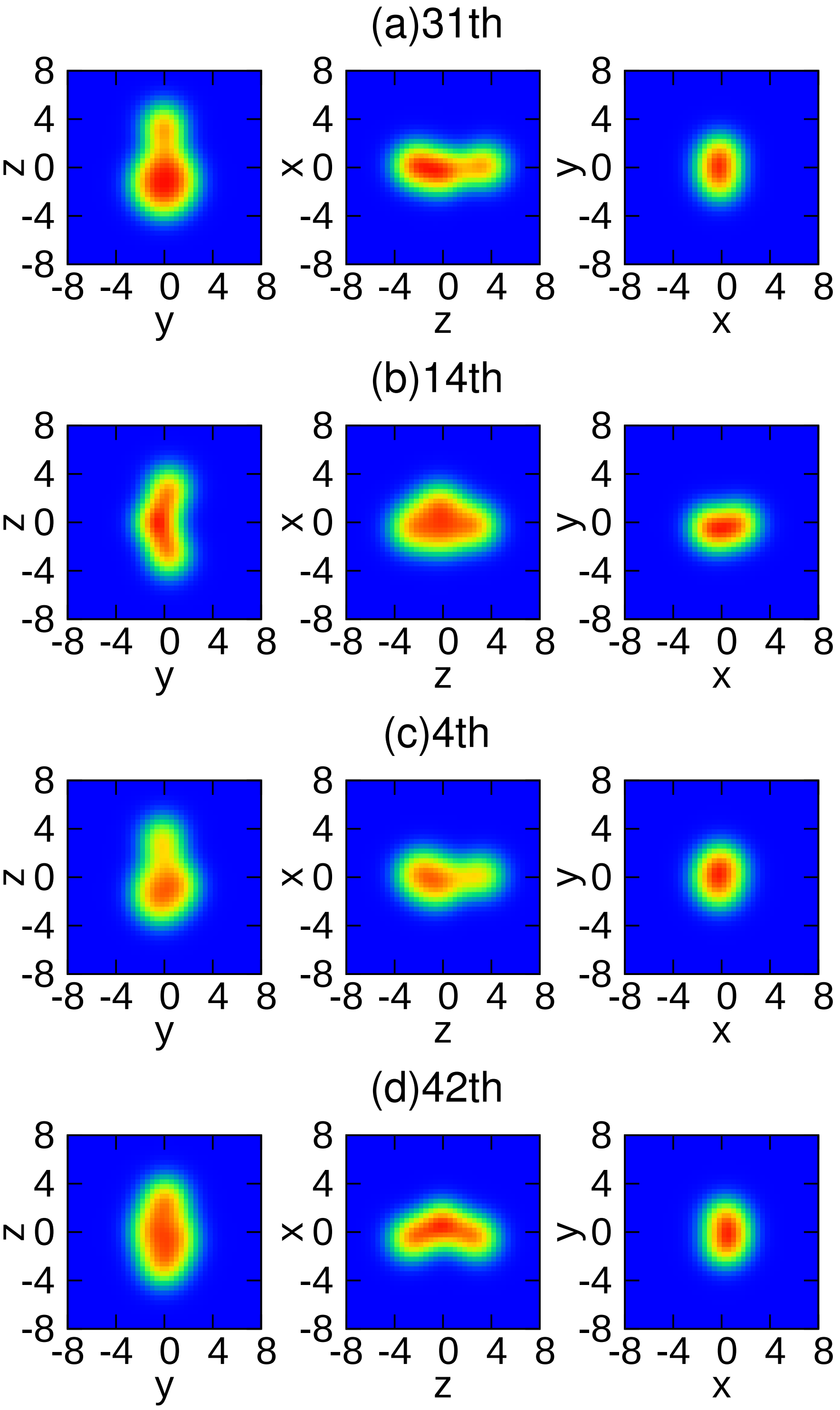

Figure 4.8: Contour plots of the density distribution of the 31th, 14th, 4th, and 42th SDs, which are major components of 0_2^+, 2_1^+, 4_2^+, 6_2^+, 1_3^-, and 3_3^- for ^{16}O.

(a) 2nd

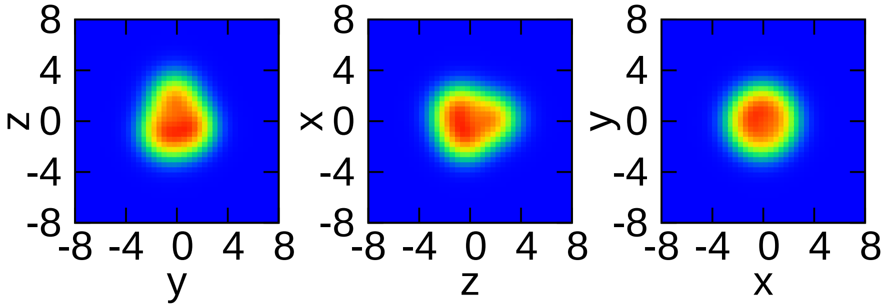

(b) 20th

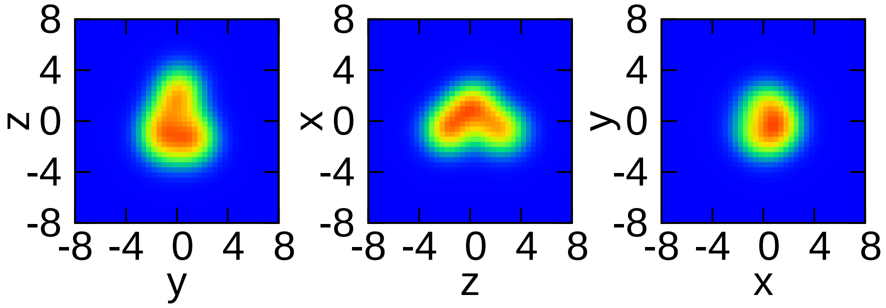

(c) 18th

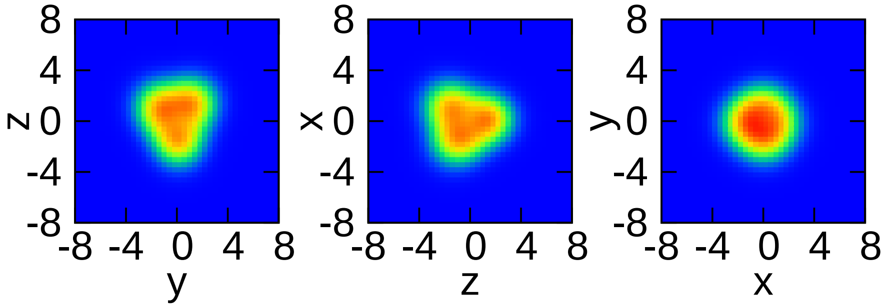

Figure 4.9: Contour plots of the density distribution of the 2nd, 20th, and 18th SDs, which are major components of the negative-parity states 1_1^-, 2_1^-, and 3_1^- for ^{16}O.

Chapter 5

Results: ^{20}Ne

5.1 Structure of ^{20}Ne

Based on understanding of cluster models, ^{20}Ne nucleus shows transitional character between mean-field like and α+^{16}O cluster-like structures. The $T = 0$ states of ^{20}Ne below about 10 MeV excitation can be classified into $K^\pi = 0_1^+$, 0_2^+, 0_3^+, 0_4^+, 0^- and 2^- bands. The $K^\pi = 0_1^+$ and $K^\pi = 0^-$ bands are regarded as inversion doublet partner [82]. The $K^\pi = 0^-$ states show the well-developed α+^{16}O cluster structure. On the other hand, $K^\pi = 0_1^+$ rotational band show transitional character between mean-field like and α+^{16}O cluster structure. This is because the difference of ground state energy and the α+^{16}O breakup threshold is 4.7 MeV, which is smaller than other nuclei like 7.2 MeV between the ground state of ^{16}O and α+^{12}C threshold energy.

Many theoretical approaches have been applied to the structures of ^{20}Ne. Results by SM calculations are in good agreement with measured values for the low-lying states [83–85]. However, the SM calculation employs some effective charge to calculate transitional strengths. The MF calculation is applied only to the $K^\pi = 0^+$ rotational band. The excitation energies of the rotational band states are in good agreement with measurement. The microscopic and semi-microscopic cluster models, RGM, OCM, and GCM well reproduce the experimental data [86–92]. The microscopic and semi-microscopic cluster models assume the existence of some clusters. The AMD calculation, which does not assume any clusters, was applied to ^{20}Ne [93–95]. In Ref. [95], deformed-basis AMD was applied to ground and excited states of ^{20}Ne and reproduces the $K^\pi = 0_1^+$, 0_4^+, 0^-, and 2^- bands. The *ab-initio* UCOM+FMD calculation well reproduced the $K^\pi = 0_1^+$ rotational band [96].

5.2 Convergence of results: Statistical treatment

In this section, we examine the convergence of the energy levels of ^{20}Ne. As in ^{12}C (Sec. 3.2) and ^{16}O (Sec. 4.2), we discuss convergence by using ten different sets of SDs. We prepare ten sets of the SDs and calculate energy levels for each set. If the calculated energy levels are close to each other among the ten different sets of SDs, one may conclude that the calculated energy levels are reliable. These ten set of SDs are composed of 50 SDs, which are prepared

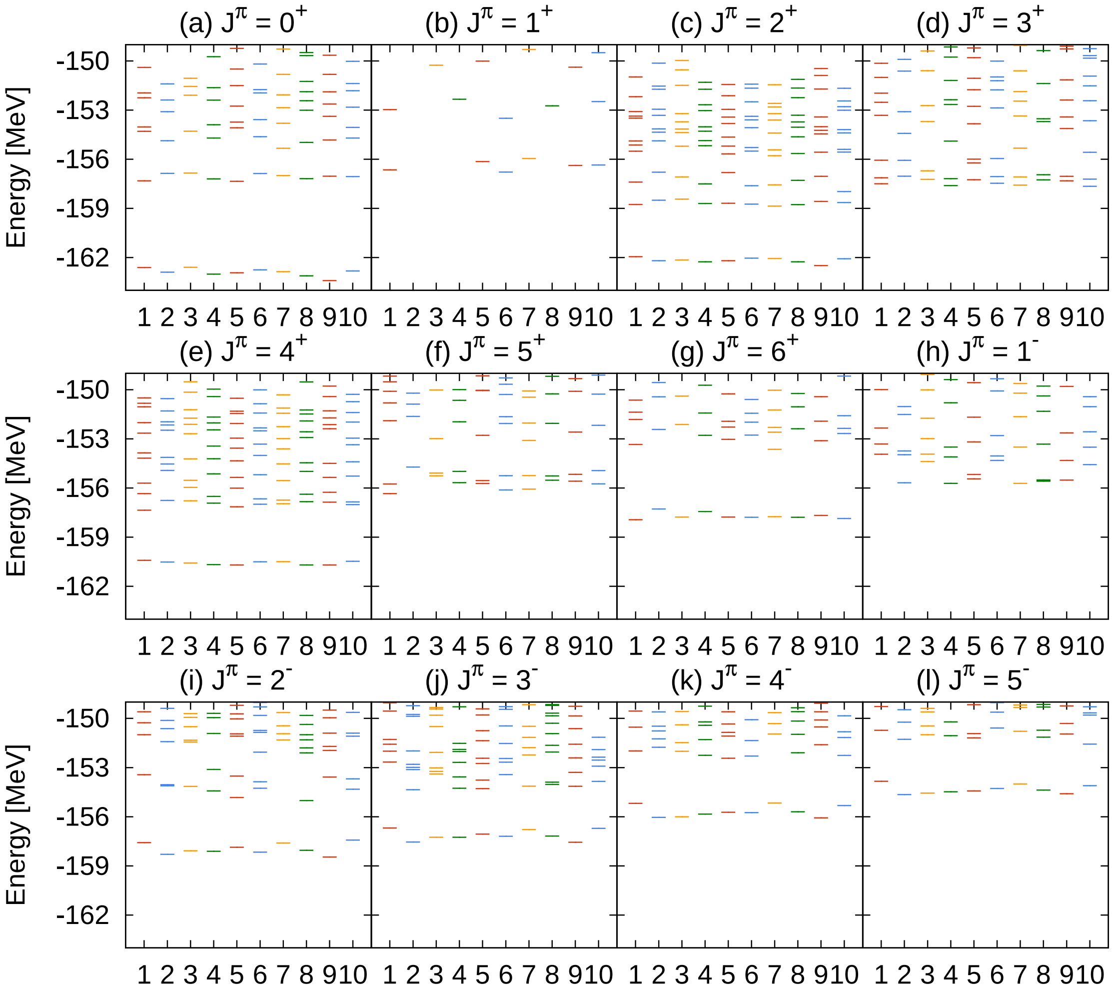

Figure 5.1: Energy levels of the ^{20}Ne nucleus for $J^\pi = 0^+$, 1^+, 2^+, 3^+, 4^+, 5^+, 6^+, 1^-, 2^-, 3^-, 4^- and 5^-. Calculations employing ten different sets of SDs are shown. See the text for details.

by the procedure explained in Sec. 2.2. Different seeds for the random numbers, which are used to prepare initial states in Eq. (2.2.1), are employed to generate the different sets.

In Fig. 5.1, we show the energy levels of the ^{20}Ne nucleus for the ten sets calculated in the procedure explained in Sec. 2.2. The energy levels are shown for $J^\pi = 0^+$, 1^+, 2^+, 3^+, 4^+, 5^+, 6^+, 1^-, 2^-, 3^-, 4^-, and 5^-.

We examine the calculated energy levels of $J^\pi = 0^+$ in Fig. 5.1(a). The lowest energy level is located around -163 MeV. The difference among the ten sets is less than 1 MeV. The second energy level appears around -157 MeV. The difference of energies among ten sets is again less than 1 MeV. The third excite state is located around -155 MeV. The difference among the ten sets is about 1.5 MeV, which is a little larger than that of the lowest and second lowest energy levels. We then may state that the energies of these three lowest states are calculated reliably, although the energies of the third excited state is inferior reliability than that of the lowest and second lowest excited states.

The energy levels of $J^\pi = 2^+$ in Fig. 5.1(c) indicate that the energies of lowest two or three states are reliable with a small variation. For $J^\pi = 3^+$ and 4^+ states [5.1(d) and 5.1(e)], the lowest two states are reliable. The energy levels of 5^+ and 6^+ in Figs. 5.1(f) and 5.1(g) indicate that only the lowest energy level is reliable. However, the calculated energies of $J^\pi = 1^+$ states vary greatly according to the set of SDs even for the lowest states [Fig. 5.1 (b)]. This may be same reason as the energy levels of $J^\pi = 1^+$ for ^{12}C in Fig. 3.1 and for ^{16}O in Fig. 4.1.

For the $J^\pi = 1^-$ state [Fig. 5.1 (h)], the lowest energy level may be located around -156 MeV, although there is no corresponding the lowest energy level of some set of SDs like second, third, seventh, and tenth. The energy levels of $J^\pi = 2^-$, 3^-, 4^-, 5^-, and 6^- indicate that lowest state for each J^π may be reliable. The energies of the second lowest state show a large variation among the ten sets [Figs. 5.1(i)-5.1(l)].

For physical quantities like energies, transition strengths, and radii, we calculate statistical averages and standard deviation among the ten sets as with the physical quantities of ^{20}Ne. We show the physical quantities as average values and the standard deviation as errors.

5.3 Energy levels

We show calculated excitation spectra of positive- and negative-parities in Figs. 5.2 and 5.3. In the figures, the average values are shown with the error bars. The error bars only show the lowest four states. For comparison, we also show the results of AMD [95], RGM [86], and SM [85]. Although not specified in the figure, the SM provide six energy levels between 4_2^+ and 8_1^+. The AMD is employed localized triaxially deformed Gaussian as the single-particle wave packet and is performed superposition of many different deformed SDs. The RGM is one-channel resonating group method for α+^{16}O system. The SM is taken in full *sd* configurations.

First, we discuss the ground-state band of $0_1^+, 2_1^+, 4_1^+$, and 6_1^+. These states are connected by strong $E2$ transition strengths showed in next section [Sec. 5.4]. In Sec. 5.7, we will show that this band corresponds to a α+^{16}O state. In the Skyrme HF, the binding energy is 157.2 MeV, which is smaller than measurement, 160.65 MeV. The ground state energy after configuration mixing is -162.9 ± 0.2 MeV, which is larger than measurement. The correlation energy is 5.7 ± 0.2 MeV. The readjustment of the Skyrme parameter set is might be resolved the difference between the ground-state energy after configuration-mixing and that of the measured value. Such refinement of the force will be an important issue in our future studies. The moment of inertia of the ground band is overestimated the measurements. These tendencies are also found the results of AMD and RGM calculations. On the other hand, the SM calculation well reproduces the excitation energy of these states. If we take account of the paring correlation, the overestimation of moment of inertia might be improved.

For the negative-parity states, we have obtained reliable results only for the lowest energy state for each J^π [Sec. 5.2] except $J^\pi = 1^-$ state. For the 1_1^- and 3_2^- states, the states are

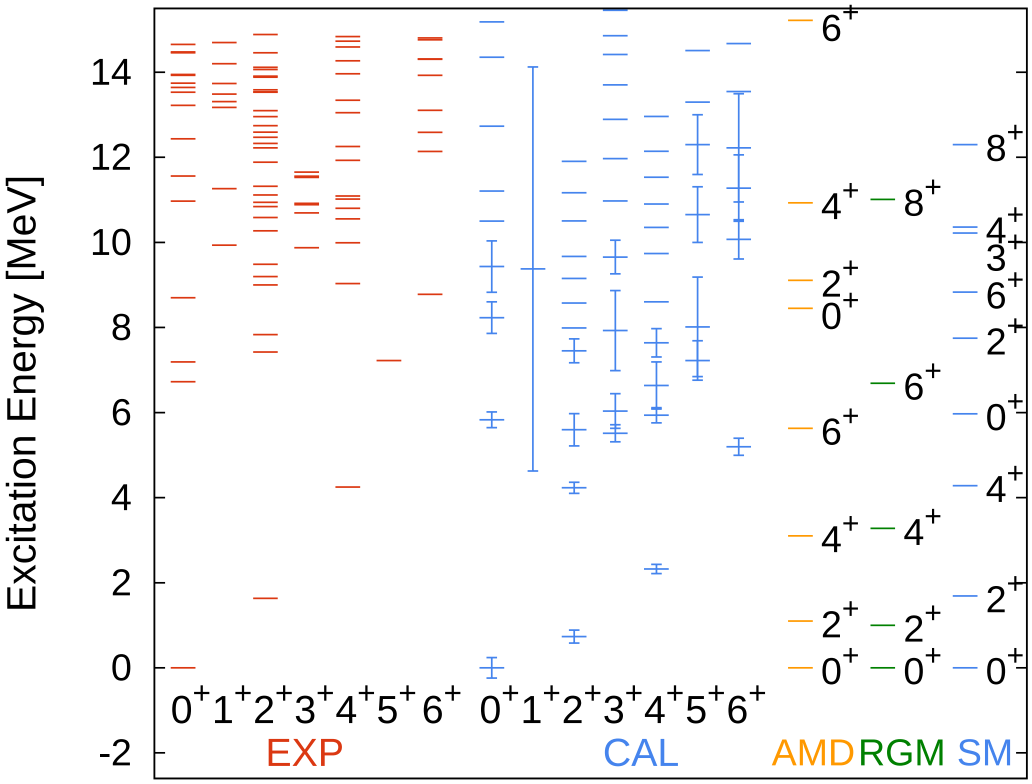

Figure 5.2: Excitation energies of positive-parity are shown. The energies are obtained by averaging over ten configurations. The standard deviations of the energies are also shown by error bars. The error bars only show the four lowest states. We also show the results of AMD [95], RGM [86], and SM [85]. Experimental data are taken from Refs. [80]. See the text for details.

considered as parity-doublet partner of the ground-state band. However, our calculation does not give a converged solution for these states.

For the 2_1^-, 3_1^-, 4_1^-, 5_1^-, and 6_1^- states, the states are considered to show $(0p)^{-1}(sd)^{-5}$ structure. The error bars for these states are smaller than those of other levels. The excitation energies are in good agreement with measurements. The AMD calculation gives higher excitation energies for the states.

We mention how the calculated energy levels depend on interactions. In Figs. 5.4 and 5.5 we show the excitation energies of positive- and negative-parity states with different sets of the Skyrme interaction, SLy4, SGII, SIII, and SkM*, and Gogny D1S interaction. The same set of SDs is employed in all calculations. The correlation energies in the ground states are shown as well inside the parentheses. The comparison shows that basic features of the spectra do not depend much on the choice of the Skyrme parameters. However the second lowest states for $J^\pi = 0^+$, 2^+, 4^+, and 6^+ of Gogny D1S interaction are higher than that of Skyrme interactions. We conclude that the excitation energies for the ground-state band and

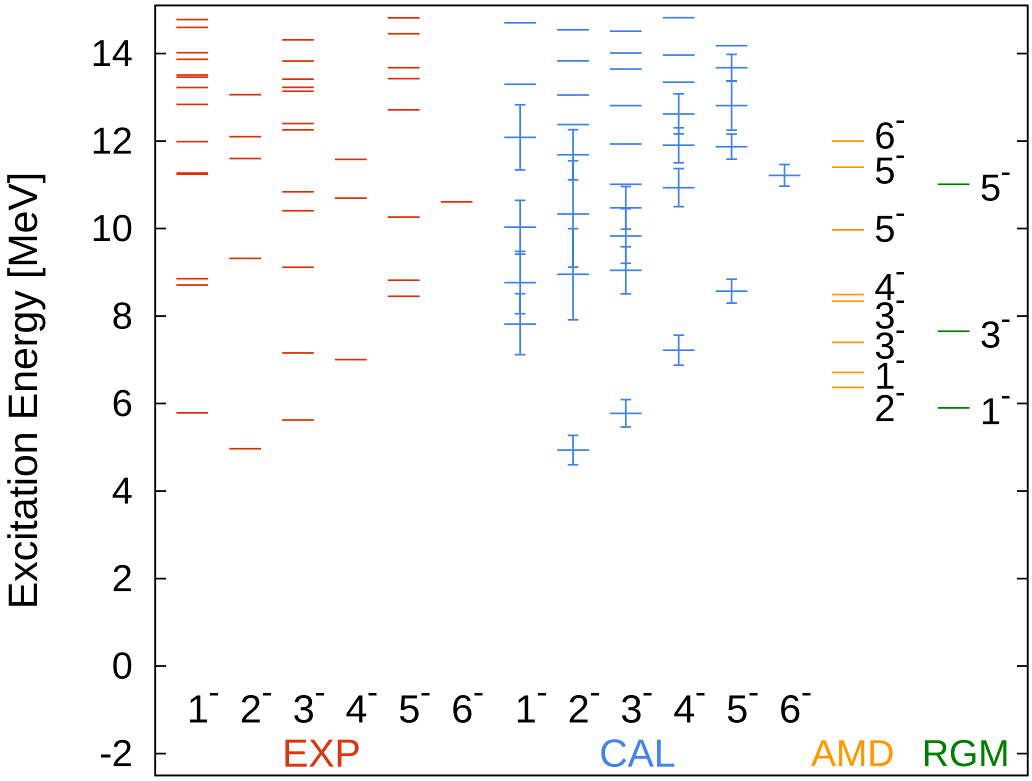

Figure 5.3: Excitation energies of negative-parity are shown. The same explanation as that in Fig. 5.2 applies to others.

negative-parity are not sensitive to choice of interaction. However, the excitation energies of second or higher states is depend on choice of interaction.

5.4 Transition strength

We show the average values and the standard deviations of $B(E2)$ and $B(E3)$ values are shown in Table. 5.1. The units of $B(E2)$ and $B(E3)$ are $e^2\text{fm}^4$ and $e^2\text{fm}^6$, respectively. For comparison, we also show the values of PPSHF [97], AMD [95], 5α GCM [92], α+^{16}O OCM [87], RGM [86], and shell Model [98]. The RGM and SM are introduced effective charge.

As we discussed in Sec. 5.3, states of 0_1^+, 2_1^+, 4_1^+, and 6_1^+ follow the ground-state band sequence. The $B(E2; 2_1+ \to 0_1^+)$, $B(E2; 4_1^+ \to 2_1^+)$ and $B(E2; 6_1^+ \to 4_1^+)$ are reproduced by all model.

The $K^\pi = 2^-$ band which starts from the 2^- state show a rotational spectrum. This band is known to have a $(0p)^{-1}(sd)^5$ structure. These states correspond to 2_1^-, 3_1^-, 4_1^-, and 5_1^-. The errors of measured transition strength between these states are rather large. The transition strengths between these states are well described by the present, PPSHF, AMD,

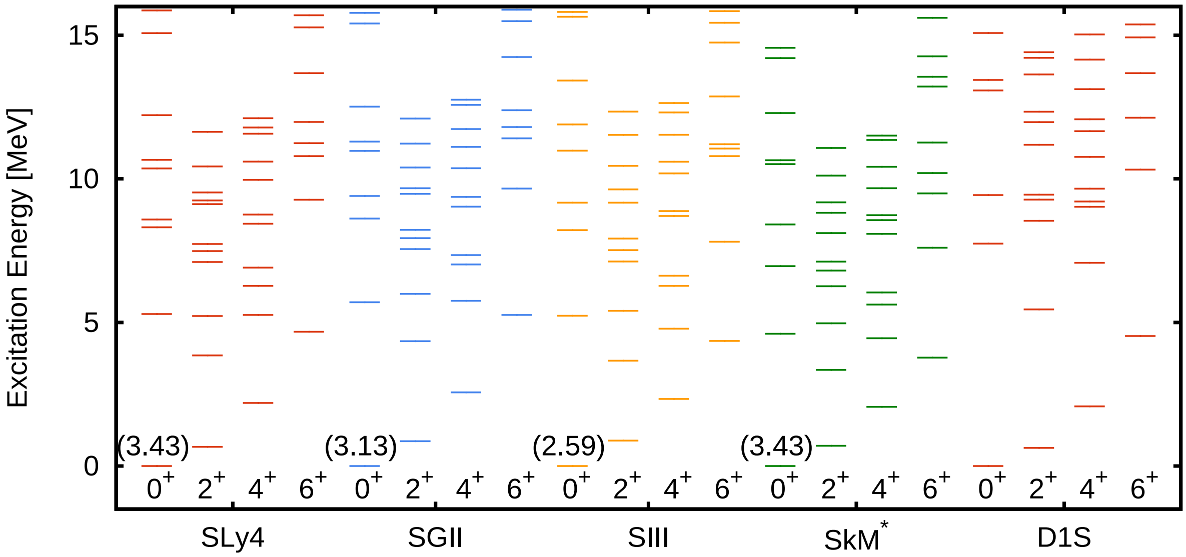

Figure 5.4: Energy levels of positive-parity for ^{20}Ne employing different parameter sets of Skyrme forces, SLy4, SGII, SIII, and SkM*, and Gogny D1S force. The number in parentheses is the correlation energy in the ground state, $E_{\rm HF} - E_{\rm gs}$, in unit of MeV. In the calculation, the same set of SDs is employed.

GCM, OCM, RGM, and SM. Our results are somewhat larger than the other theoretical one.

The calculated $B(E2; 3_2^- \rightarrow 1_1^-)$ is smaller than the measured value. However, the standard deviation of the value is very large, be cause the excitation energies of 3_2^- and 1_1^- states fluctuate large as shown in Sec. 5.2. The $E2$ strength for the seventh set of SDs is $128e^2$fm^4, which is very similar as the measurement. Same thing can be seen as $B(E2; 5_2^- \rightarrow 3_2^-)$. The value of seventh set of SDs is $140e^2$fm^4.

The $B(E3; 2_1^- \rightarrow 2_1^+)$ is reproduced by our approach and OCM calculation. The calculated $B(E3; 3_1^- \rightarrow 0_1^+)$ underestimate the measurement in our calculation and OCM. Our result is larger than value of OCM and closes the measured value.

5.5 Radii

We next examine rms radii of the ground and excited states for ^{20}Ne. For comparison, results of mean-field calculation with variation after projection (MF(VAP)) [100], MF with variation before projection (MF(VBP)) [101], 5α GCM [92], and α+^{16}O RGM [86] are shown. As mentioned in Sec. 3.5 and Sec. 4.5, our wave function does not allow an exact separation of the center-of-mass motion from the internal one. We therefore subtract an approximate correction for the radius due to the center-of-mass motion from the calculated values. In addition to correction of center-of-mass motion, we take into account proton size effect. The corrections of center-of-mass motion and of proton size effect cancel each other for the opposite

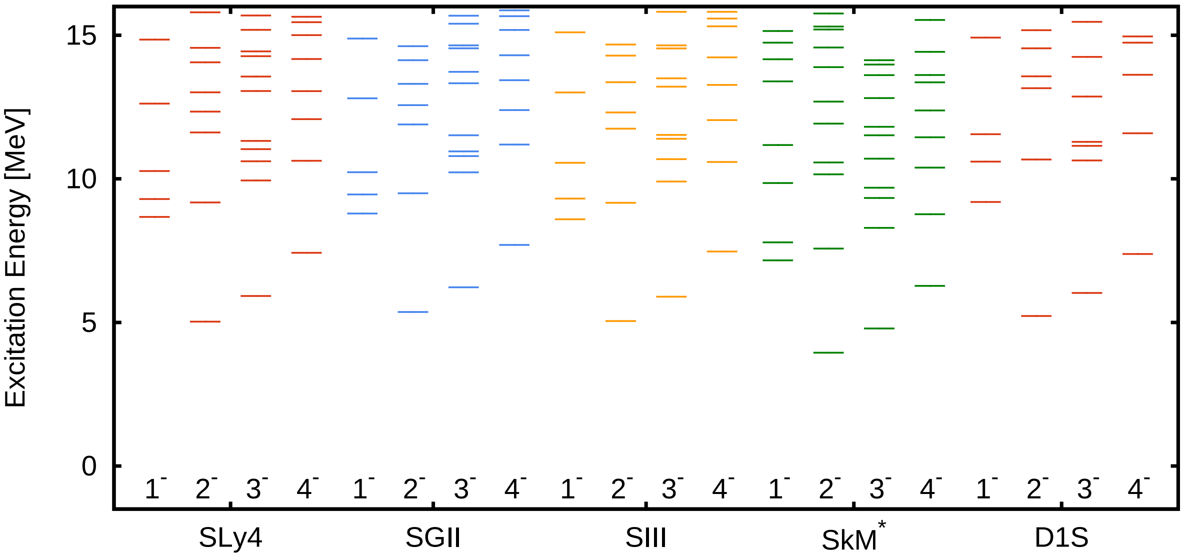

Figure 5.5: Energy levels of negative-parity for ^{20}Ne employing different parameter sets of Skyrme force, SLy4, SGII, SIII, and SkM*, and Gogny D1S force. In the calculation, the same set of SDs is employed.

sign. The calculated radii after the corrections are shown in Table 5.2.

Our calculated value in the ground state is 3.16 ± 0.01 fm. This value is somewhat larger than that of the measured value, 2.91 fm. In the HF calculation, the radius is given by 2.99 fm, which is in good agreement with measured value. Our configuration-mixing calculation, therefore, slightly increases the radius. The MF(VBP) reproduces the radius of ground state. The other theoretical calculations predict a smaller value than measured value. Our radius diminishes as the angular momentum is increased. This feature is similar to mean-field calculations.

5.6 Charge form factors

We next examine charge form factor for elastic process of ^{20}Ne. We correct the center-of-mass and proton size effect in the same evaluation of charge factor for ^{12}C in Sec. 3.6 and ^{16}O in Sec. 4.6. Both effects cancel each other. In Fig. 5.6, we show the charge form factor for elastic process of ^{20}Ne. Red solid curve shows our results, blue dashed curve shows the results of α+^{16}O-core model [102], and crosses with error bars show experimental data [103]. We also show that of Skyrme HF solution in the ground state [Fig. 5.6(yellow dotted curve)].

In the small momentum transfer region $q^2 < 1.5\text{fm}^{-2}$, the elastic form factor is well reproduced by the calculation. For $q^2 > 1.5\text{fm}^{-2}$, our calculation slightly underestimates the form factor. The position of the dip at around 1.5fm^{-2} is reproduced well. On the other hand, the Skyrme HF calculation well reproduces the elastic form factor in whole momentum

transitions	Expt.	Calc.	PPSHF	AMD	GCM	OCM	RGM	SM
$B(E2; 2_1^+ \to 0_1^+)$	65.5 ± 3.3	55.1 ± 3.5	41.6	70.3	50.0	57.0	36.2	57.0
$B(E2; 4_1^+ \to 2_1^+)$	71 ± 6	66.6 ± 4.5	59.9	83.7	64.4	70.9	45.2	69.9
$B(E2; 4_2^+ \to 2_1^+)$	19 ± 2	0.36 ± 0.17						
$B(E2; 0_2^+ \to 2_1^+)$	12	12.2 ± 3.2						
$B(E2; 0_3^+ \to 2_1^+)$	0.99 ± 0.19	0.70 ± 0.76						
$B(E2; 2_3^+ \to 0_1^+)$	2.4 ± 0.3	0.25 ± 0.20						
$B(E2; 6_1^+ \to 4_1^+)$	64 ± 10	53.9 ± 6.6	67.5	52.7	55.3	57.1	36.5	57.9
$B(E2; 3_1^- \to 2_1^-)$	113 ± 29	127 ± 8	97.6	102.8		107.5		97
$B(E2; 4_1^- \to 3_1^-)$	77 ± 16	90 ± 5	73.5	77.8		77.0		75
$B(E2; 4_1^- \to 2_1^-)$	34 ± 6	42 ± 5	32.9	38.5		34.0		36
$B(E2; 5_1^- \to 4_1^-)$	< 808	57 ± 3	52.6	84.5		33.9		44
$B(E2; 5_1^- \to 3_1^-)$	84 ± 19	62 ± 3	53.1	56.5		66.7		48
$B(E2; 6_1^- \to 5_1^-)$	32 ± 13	36 ± 2	39.7	29.9		49.4		32
$B(E2; 6_1^- \to 4_1^-)$	55^{+23}_{-13}	67 ± 7	67.0	64.0		45.1		51
$B(E2; 3_2^- \to 1_1^-)$	161 ± 26	59.8 ± 48.7		151.2	155		121	
$B(E2; 5_2^- \to 3_2^+)$		77 ± 42		182.4	206		133	
$B(E3; 2_1^- \to 2_1^+)$	143 ± 119	182 ± 24				117		
$B(E3; 3_1^- \to 0_1^+)$	261 ± 95	98 ± 12				29.9		

Table 5.1: Observed and calculated B(E2) and B(E3) values of ^{20}Ne in units of e^2fm^4 and e^2fm^6. Observed and calculated results are shown in first and second column. The values of parity projected Hartree-Fock (PPHF) [97], AMD [95], 5α GCM [92], α+^{16}O OCM [87], RGM [86], and SM [98] are also shown for comparison. Experimental data are taken from Ref. [80].

region. The α+^{16}O-core model show small magnitude of charge form factor for $q > 1$fm^{-2}.

5.7 Analysis of wave functions

5.7.1 $K^\pi = 0^+$ and 0^- bands

In Table 5.3, we show the number of the SDs which have large overlap values with the wave function of the states, 0_1^+, 2_1^+, 4_1^+, 6_1^+, 1_1^-, and 3_2^-.

The 0_1^+ and 2_1^+ states have the largest overlap between 2nd SD. In the 4_1^+ state, the 1st SD, which is HF state, is the largest component and 2nd SD is the second largest. The 6_1^+ state have the largest overlap with 33th SD. The HF state is included more than 0.7 in states of $K^\pi = 0^+$ band. The parity-doublet partner of $K^\pi = 0^+$ states, 1_1^- and 3_2^- states have large overlap with 15th SD, which have about 0.8 overlap value to 0_1^+ and 2_1^+. We show the counter plots of densities distributions of the SDs which are large components of $K^\pi = 0^\pm$ band in Fig. 5.7. As seen from the figure, 2nd, 1st and 33th SDs show deformed prolate shape. On the other hand, the 15th show well developed α+^{12}C structure. This is consistent with the transitional character between mean-field like and α+^{12}C cluster structure of $K^\pi = 0^+$ band

J^π	Expt.	Calc.	MF(VAP)	MF(VBP)	5α GCM	α+^{16}O RGM
0_1^+	2.91	3.16 ± 0.01	2.72	2.95	2.65	2.87
2_1^+		3.10 ± 0.01	2.71	2.94		
4_1^+		3.07 ± 0.01	2.70	2.92		
6_1^+		3.03 ± 0.01	2.68	2.89		

Table 5.2: Charge radii of the ground and excited states of ^{20}Ne. The experimental data is taken from Ref. [99]. For comparison, we show the results of mean-field calculation with variation after projection (MF(VAP)) [100], MF with variation before projection (MF(VBP)) [101], 5α GCM [92], and α+^{16}O RGM [86]. See text for details.

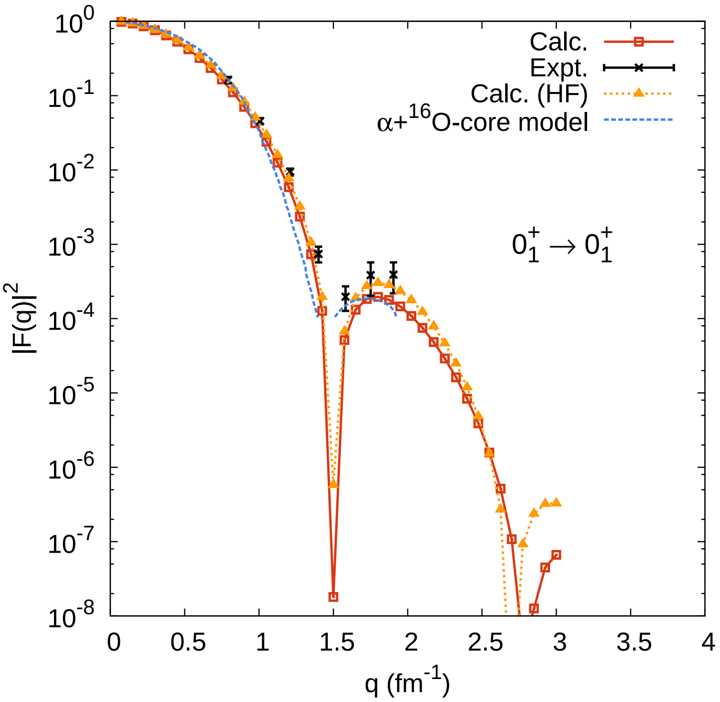

Figure 5.6: Squared elastic form factor for the ground state are shown. Our calculated results are compared with the HF calculation with a single SD, α+^{16}O-core model [102], and measurements [103]. Here, the results using the first set of SDs in Fig. 5.1 are used.

and well developed cluster structure of $K^\pi = 0^-$ band.

5.7.2 $K^\pi = 2^-$ band

In the negative-parity of ^{20}Ne, the $K^\pi = 2^-$ band which is considered to be $(0p)^{-1}(sd)^5$ structure in the deformed mean filed appear in present calculation. As Table. 5.1 illustrates,

0_1^+			2_1^+			4_1^+			6_1^+		
SD	K	P	SD	K	P	SD	K	P	SD	K	P
2	0	0.86	2	0	0.84	1	0	0.82	33	0	0.80
5	0	0.84	5	0	0.84	2	1	0.80	30	1	0.79
15	0	0.80	1	0	0.81	41	0	0.79	2	1	0.77
1	0	0.78	45	0	0.76	5	1	0.75	5	1	0.77
13	0	0.77	15	0	0.76	33	0	0.75	20	1	0.75
9	0	0.72	13	0	0.75	2	0	0.75	1	0	0.74
45	0	0.72	41	0	0.75	45	0	0.75	41	0	0.74
41	0	0.70	9	0	0.74	20	0	0.74	9	0	0.74
20	0	0.68	20	0	0.71	9	0	0.74	30	0	0.73
10	0	0.64	33	0	0.67	5	0	0.74	20	0	0.71

1_1^-			3_2^-		
SD	K	P	SD	K	P
15	0	0.60	15	1	0.60
10	0	0.58	9	1	0.48
5	0	0.54	41	1	0.38
16	0	0.52	22	0	0.36
9	0	0.50	22	2	0.34
22	1	0.45	36	0	0.32
50	0	0.44	30	1	0.31
18	0	0.44	27	1	0.30
36	1	0.41	16	1	0.26
30	0	0.40	36	2	0.25

Table 5.3: The SDs which dominate in the ground rotational $K^\pi = 0^+$ and $K^\pi = 0^-$, the K value, and the squared overlap between each SD and the wave function after configuration mixing are shown.

these states are connected by strong $E2$ value. In the 2_1^- state, the 13th SD is the largest component and 15th is the second largest. In the 3_1^-, 4_1^-, 5_1^-, and 6_1^- states, the 1st SD has the largest overlap. We show in the Fig. 5.8 the density distribution of the 13th and the 5th SDs. They show prolate shapes.

2_1^-			3_1^-			4_1^-			5_1^-			6_1^-		
SD	K	P	SD	K	P	SD	K	P	SD	K	P	SD	K	P
13	2	0.93	5	2	0.87	5	2	0.88	5	2	0.78	5	2	0.77
5	2	0.91	13	2	0.87	13	2	0.87	15	2	0.76	13	2	0.71
15	2	0.86	15	2	0.83	15	2	0.82	9	2	0.73	2	2	0.67
6	2	0.82	6	2	0.74	9	2	0.71	13	2	0.72	15	2	0.64
9	2	0.68	9	2	0.69	6	2	0.70	33	2	0.64	9	2	0.63
18	2	0.63	33	2	0.59	33	2	0.62	2	2	0.59	33	2	0.62
45	2	0.62	45	2	0.59	45	2	0.60	45	2	0.57	45	2	0.59
16	2	0.61	10	2	0.57	2	2	0.57	30	2	0.54	22	5	0.55
10	2	0.61	2	2	0.54	22	2	0.52	6	2	0.54	30	2	0.55
33	2	0.59	18	2	0.54	20	2	0.50	20	2	0.51	5	2	0.51

Table 5.4: The SDs which dominate in the $K^\pi = 2^-$ band, the K value, and the squared overlap between each SD and the wave function after configuration mixing are shown.

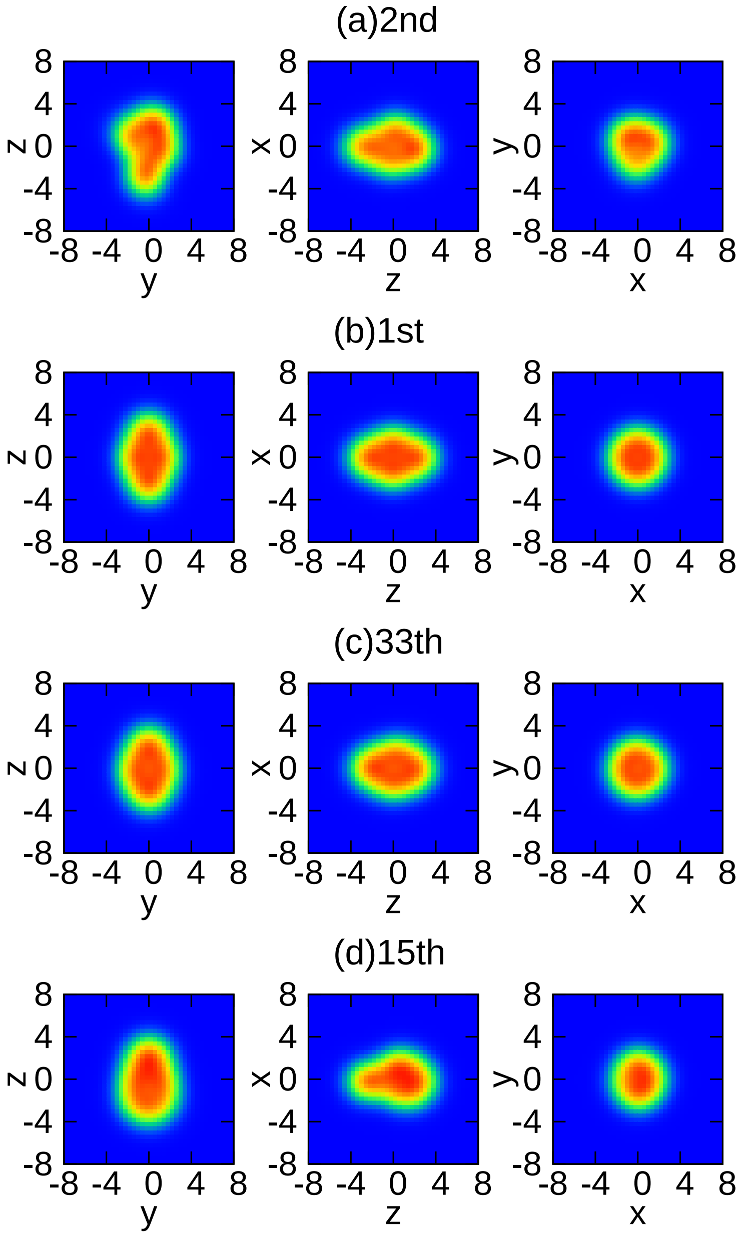

Figure 5.7: Contour plots of the density distribution of the 2nd, 1st, 33th, and 15th SDs in ^{20}Ne, which are major components of the $K^{\pi} = 2^{-}$ bands, 2_1^-, 3_1^-, 4_1^-, 5_1^- and 6_1^-.

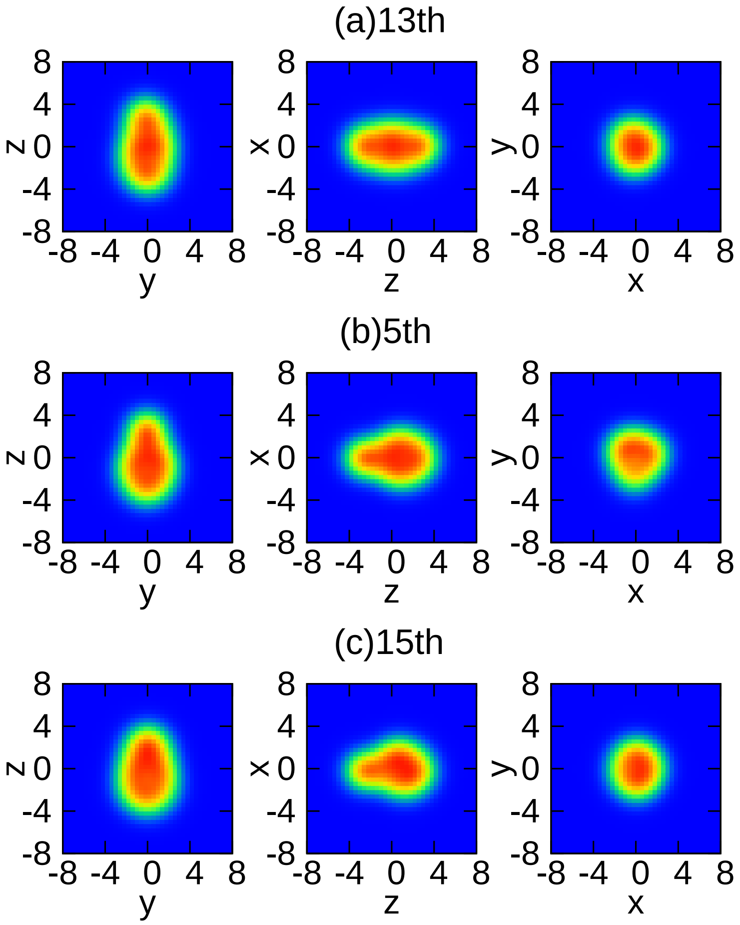

Figure 5.8: Contour plots of the density distribution of the 13th, 5th, and 15th SDs in ^{20}Ne, which are major components of the $K^\pi = 0^\pm$ bands, 0_1^+, 2_1^+, 4_1^+, 1_1^-, and 3_2^-.

Chapter 6

Summary and future problems

In light nuclei, structures with various correlations appear in ground and excited states. While ground states of most light nuclei may be understood by the shell model, there appear a number of cluster structures in excited states. To understand these structures of light nuclei, we apply a new configuration mixing approach to investigate the structure of ^{12}C, ^{16}O, and ^{20}Ne nuclei. Our method is the configuration-mixing approach using Skyrme and Gogny interactions. This approach enables us to obtain reliable descriptions of ground and low-lying excited states, taking both configurations of shell-model and cluster states.

In our approach, we aim to obtain converged solutions of ground and excited states once many-body Hamiltonian is specified. We first generate a number of Slater-determinants using the imaginary-time method starting from initial Slater-determinants which are prepared in a stochastic way. These Slater-determinants are found to show various shapes and clustering. In the next step, the Slater-determinants are projected into eigenstates of parity and angular momentum. Finally they are superposed to diagonalize the many-body Hamiltonian. In practice, we have generated several sets of Slater-determinants and compare the results with difference sets, to quantify the reliability of the calculation. Calculated results of a few low-lying states for each parity and angular momentum coincide accurately, indicating they are well converged with small variance among the different sets of the Slater-determinants. This fact shows that the present calculation provides unique and converged results for the ground and a few low-lying excited states, once the effective nucleon-nucleon force, the Skyrme interaction in the present calculation, is given.

Our calculations reasonably reproduce the overall features of the structure of ^{12}C. The energies and the $B(E2)$ transition strength of the ground state rotational band are well described. The lowest excited states of negative parity, 1^-, 2^-, and 3^-, are also reasonably described, although the excitation energies are slightly too high. The Slater-determinants which dominate in these states show three-α structure. Our calculations also reproduce the excitation energy of the Hoyle (0_2^+) state reasonably. This state is found to be described by a superposition of many Slater-determinants, consistent with the former cluster-model calculations. However, the radius of the 0_2^+ state is calculated to be significantly smaller than those. The spin-orbit interaction which contributes much to the energy in the present method seems to be responsible for this difference. The three-α linear-chain structure appears at around 15 MeV excitation, forming a rotational band. We find two 2^+ states, 2_2^+ and 2_3^+, to appear at excitation energies over 10 MeV in our calculations. Recent measurements report excitation of a 2^+ excited state in a similar energy region. There have been arguments that the measure 2^+ state is a member of the rotational excitation built on the 0_2^+. However, our calculation provides rather small $B(E2)$ values for the transitions of both $2_2^+ \to 0_2^+$ and $2_3^+ \to 0_2^+$. This fact suggests that neither 2_2^+ nor 2_3^+ state may be regarded as the rotationally excited Hoyle state.

We next apply the present method to ^{16}O nucleus. Experimentally, the lowest excitation state is 0_2^+ state whose excitation energy is 6.0 MeV. Microscopic cluster models failed to reproduce this state. Although OCM and shell model reported reasonable descriptions, these theories include some empirical parameters. Our calculated excitation energy of the 0_2^+ state is about 9 MeV. Although this value is 3 MeV higher than the measured value, it is much better than those of cluster models: AMD, RGM, and GCM reported about 13 MeV or more excitation energies for this state. The 0_2^+, 2_1^+, 4_2^+, and 6_2^+ states are connected by the strong $B(E2)$ strength in our calculation. The Slater-determinants which dominate in these states show α+^{12}C cluster structure. For the negative parity, the 1_3^- and 3_3^- states are found to have large overlap with Slater-determinants which have α+^{12}C configuration. The particle-hole excitation states, 1_1^-, 2_1^-, and 3_1^-, are reasonably reproduced by our method.

We next apply our method to ^{20}Ne nucleus. States of 0_1^+, 2_1^+, 4_1^+, and 6_1^+ follow the ground-state band sequence. Calculated $E2$ transition strength between these states are in good agreement with measurements. However, calculated moment of inertia for this band is larger than the measured value. The Slater-determinants which dominate in these states show α+^{16}O cluster structure. We also get the parity-doublet partner of the ground band, 1_1^- and 3_2^-, which show α+^{16}O cluster structure. The 2_1^-, 3_1^-, 4_1^-, and 5_1^- states are connected by strong $E2$ strength. The calculated excitation energies of these states and $B(E2)$ values between these states are in good agreement with measurements. The calculated radius of the ground state and charge form factor is also in good agreement with measurements.

The success for the description of ^{12}C, ^{16}O, and ^{20}Ne nuclei reported in this thesis shows that the present approach is promising for systematic descriptions of various many-body correlations including clustering in light nuclei. Since the present approach does not assume anything regarding nuclear shape and single-particle wave functions, it will be useful for unstable nuclei for which experiments are proceeding rapidly .

In recent years, *ab-initio* approaches starting with realistic nucleon-nucleon force have been shown significant advances. These approaches have been successful in describing the ground and some low-lying excited states of light nuclei. In the present study, we used empirical forces; Skyrme and Gogny forces. It is certainly an interesting extension to use realistic nucleon-nucleon interaction in our approach. Since our approach may take into account a variety of long-range correlations, extension of our approach to use realistic nucleon-nucleon interactions will enable us to achieve fully satisfactory descriptions of ground and low-lying states with various correlations simultaneously.

The present approach does not include tensor correlations explicitly. It is known that tensor correlation helps development of α-particle cluster structures, because the tensor force is very important to reproduce the binding energy of the α-particle. It will be very interesting to examine the effect of the tensor correlation in our approach.

Chapter 7

Acknowledgment

I would like to thanks Prof. K. Yabada for his giving me many valuable advices. Without his guidance and persistent help this thesis would not have been possible. I also would like to express my thanks to Prof. T. Nakatsukasa and Dr. Y. Funaki for their insightful comments and discussions. Finally I wish to express my thanks to other members of the nuclear theory group of University of Tsukuba for their helpful comments and encouragements.

Appendix A

Energy functional

A.1 Skyrme interaction

Skyrme interaction is composed of the density- and momentum-dependent two-body terms:

$$\begin{aligned}\hat{V}_{Skyrme}(\vec{r}_1, \vec{r}_2) &= t_0\left(1 + x_0 P_\sigma\right)\delta\left(\vec{r}_1 - \vec{r}_2\right) + \frac{1}{6}t_3\rho^\alpha\left(1 + x_3\hat{P}_\sigma\right)\delta\left(\vec{r}_1 - \vec{r}_2\right) \\ &+ \frac{1}{2}t_1\left(1 + x_1\hat{P}_\sigma\right)\left(\vec{k}^2 - \vec{k}^2\right)\delta\left(\vec{r}_1 - \vec{r}_2\right) + t_2\left(1 + x_2\hat{P}_\sigma\right)\overleftarrow{k}\cdot\delta\left(\vec{r}_1 - \vec{r}_2\right)\overrightarrow{k} \\ &+ iW_0\left(\vec{\sigma}_1 + \vec{\sigma}_2\right)\cdot\overleftarrow{k}\times\delta\left(\vec{r}_1 - \vec{r}_2\right)\overrightarrow{k}, \qquad (A.1.1)\end{aligned}$$

where $\hat{P}^\sigma$ is the spin exchange operator, and $\overleftarrow{k}$ and $\overrightarrow{k}$ are defined as

$$\overrightarrow{k} = \frac{\overrightarrow{\nabla}_1 - \overrightarrow{\nabla}_2}{2i}, \quad \overleftarrow{k} = -\frac{\overleftarrow{\nabla}_1 - \overleftarrow{\nabla}_2}{2i}. \qquad (A.1.2)$$

Here, $\overrightarrow{k}$ acts on ket state and $\overleftarrow{k}$ acts on bra state. Some parameter sets of Skyrme interaction are given in Table A.1.

A.2 Gogny interaction

The Gogny interaction is given by

$$\begin{aligned}\hat{V}_{Gogny}(\vec{r}_1, \vec{r}_2) &= \sum_{i=1}^{2}\exp\left[-(\vec{r}_1 - \vec{r}_2)^2/\mu_i^2\right]\left(W_i + B_i\hat{P}^\sigma - H_i\hat{P}^\tau - M_i\hat{P}^\sigma\hat{P}^\tau\right) \\ &\quad + iW_0(\vec{\sigma}_1 + \vec{\sigma}_2)\cdot\overleftarrow{k}\times\delta(\vec{r}_1 - \vec{r}_2)\overrightarrow{k} \\ &\quad + t_3\rho^{1/3}\left(1 + \hat{P}^\sigma\right)\delta\left(\vec{r}_1 - \vec{r}_2\right), \qquad (A.2.1)\end{aligned}$$

where $\hat{P}^\tau$ is the isospin exchange operator. Some parameter sets of Gogny interaction are given in Table A.2.

	t_0	t_1	t_2	t_3	W_0
SI	-1057.3	235.9	-100.	14463.5	120.
SII	-1169.9	585.6	-27.1	9331.1	105.
SIII	-1128.75	395.	-95.	14000.	120.
SGI	-1603.	515.9	84.5	8000.	115.
SGII	-2645.	340.	-41.9	15595.	105.
SLy4	-2488.91	486.82	-546.39	13777.	123.
SLy5	-2484.88	483.13	-549.40	13763.	126.
SkM	-2645.	385.	-120.	15595.	120.
SkM*	-2645.	410.	-135.	15595.	130.
SLy4d	-2479.662	473.216	-333.654	13487.	128.

	x_0	x_1	x_2	x_3	α	Ref.
SI	0.56	0.	0.	1.	1	[25]
SII	0.34	0.	0.	1.	1	[25]
SIII	0.45	0.	0.	1.	1	[104]
SGI	-0.02	-0.5	-1.731	0.1381	1/3	[105]
SGII	0.09	-0.0588	1.425	0.06044	1/6	[105]
SLy4	0.834	-0.344	-1.000	1.354	1/6	[106]
SLy5	0.778	-0.328	-1.000	1.267	1/6	[106]
SkM	0.09	0.	0.	0.	1/6	[107]
SkM*	0.09	0.	0.	0.	1/6	[108]
SLy4d	0.8122	-0.7228	-1.	1.3980	1/6	[109]

Table A.1: Parameter sets of Skyrme interaction. Units of t_0, t_1, t_2, t_3, and W_0 are MeV fm^3, MeV fm^5, MeV fm^5, MeV fm^6, and MeV fm^5, respectively. References are shown in last column.

	D1	D1S	D1N	D1M
μ_1	0.7	0.7	0.8	0.5
W_1	-402.4	-1720.3	-2047.61	-12797.57
B_1	-100.	1300.	1700.	14048.85
H_1	-496.2	-1815.53	-2414.93	-15144.43
M_1	-23.56	1397.6	1519.35	11963.89
μ_2	1.2	1.2	1.2	1.
W_i	-21.30	103.639	293.02	490.95
B_2	-11.77	-163.483	-300.78	-752.27
H_2	37.27	162.812	414.59	675.12
M_2	-68.81	-223.933	-316.84	-693.57
t_3	1350	1390.60	1609.46	1562.22
W_0	115	130	115	115.36
Ref.	[110]	[111]	[112]	[113]

Table A.2: Parameter sets of Gogny interaction. μ_i, t_3, and W_0 are in units of fm, MeV fm^4, and MeV fm^5, respectively. W_i, B_i, H_i, and M_i are in unit of MeV. We also show references in the last row.

The expectation value of Gogny interaction (A.2.1) for a SD Φ composed of $\phi_i(\vec{r})$ ($i = 1, \cdots, A$) is represented by

$$
\begin{aligned}
&\left\langle \Phi \middle| \hat{V}_{Gogny} \middle| \Phi \right\rangle \\
&= \frac{1}{2} \sum_{i=1}^{2} \Bigg[W_i \int d\vec{r} \rho(\vec{r}) \int d\vec{r}' \rho(\vec{r}') + B_i \sum_{\sigma,\sigma'} \int d\vec{r} \rho_{\sigma\sigma'}(\vec{r}) \int d\vec{r}' \rho_{\sigma'\sigma}(\vec{r}') \\
&\quad - H_i \sum_{\tau} \int d\vec{r} \rho^{\tau}(\vec{r}) \int d\vec{r}' \rho^{\tau}(\vec{r}') - M_i \sum_{\tau} \sum_{\sigma\sigma'} \int d\vec{r} \rho^{\tau}_{\sigma\sigma'}(\vec{r}) \int d\vec{r}' \rho^{\tau}_{\sigma\sigma'}(\vec{r}') \Bigg] \\
&\qquad \times \exp\left[- \left(\frac{\vec{r} - \vec{r}'}{\mu_i} \right)^2 \right] \\
&- \frac{1}{2} \sum_{i}^{2} \Bigg[W_i \sum_{\sigma\sigma'} \int d\vec{r} \int d\vec{r}' \rho_{\sigma\sigma'}(\vec{r}, \vec{r}') \rho_{\sigma'\sigma}(\vec{r}', \vec{r}) + B_i \int d\vec{r} \int d\vec{r}' \rho(\vec{r}, \vec{r}') \rho(\vec{r}', \vec{r}) \\
&\quad - H_i \sum_{\tau} \sum_{\sigma\sigma'} \int d\vec{r} \int d\vec{r}' \rho^{\tau}_{\sigma\sigma'}(\vec{r}, \vec{r}') \rho^{\tau}_{\sigma'\sigma}(\vec{r}', \vec{r}) - M_i \sum_{\tau} \int d\vec{r} \int d\vec{r}' \rho^{\tau}(\vec{r}, \vec{r}') \rho^{\tau}(\vec{r}', \vec{r}) \Bigg] \\
&\qquad \times \exp\left[- \left(\frac{\vec{r} - \vec{r}'}{\mu_i} \right)^2 \right] + [\text{other terms}], \qquad \text{(A.2.2)}
\end{aligned}
$$

where other terms are the same as the expectation value of Skyrme interaction Eq. (2.5.2).

Here the densities are written by using single particle wave functions $\phi_i(\vec{r},\sigma)$ as

$$\begin{aligned}
\rho(\vec{r}) &= \sum_i \sum_\sigma |\phi_i(\vec{r},\sigma)|^2, && \text{(A.2.3a)}\\
\rho^\tau(\vec{r}) &= \sum_{i\in\tau} \sum_\sigma |\phi_i(\vec{r},\sigma)|^2, && \text{(A.2.3b)}\\
\rho_{\sigma\sigma'}(\vec{r}) &= \sum_i \phi_i^*(\vec{r},\sigma)\phi_i(\vec{r},\sigma'), && \text{(A.2.3c)}\\
\rho^\tau_{\sigma\sigma'}(\vec{r}) &= \sum_{i\in\tau} \phi_i^*(\vec{r},\sigma)\phi_i(\vec{r},\sigma'), && \text{(A.2.3d)}\\
\rho(\vec{r},\vec{r}') &= \sum_i \sum_\sigma \phi_i^*(\vec{r},\sigma)\phi_i(\vec{r}',\sigma), && \text{(A.2.3e)}\\
\rho^\tau(\vec{r},\vec{r}') &= \sum_{i\in\tau} \sum_\sigma \phi_i^*(\vec{r},\sigma)\phi_i(\vec{r}',\sigma), && \text{(A.2.3f)}\\
\rho_{\sigma\sigma'}(\vec{r},\vec{r}') &= \sum_i \phi_i^*(\vec{r},\sigma)\phi_i(\vec{r}',\sigma'), && \text{(A.2.3g)}\\
\rho^\tau_{\sigma\sigma'}(\vec{r},\vec{r}') &= \sum_{i\in\tau} \phi_i^*(\vec{r},\sigma)\phi_i(\vec{r}',\sigma'), && \text{(A.2.3h)}
\end{aligned}$$

where τ denote neutron or proton.

A.3 Off-diagonal matrix elements of Hamiltonian

In this section, we show how to calculate matrix elements of many-body operators between different Slater-determinants Φ and Ψ composed of $\phi_i(x)$ and $\psi_i(x)$ $(i = 1, \cdots, A)$, respectively. This procedure is used need to perform projection calculation.

Bi-orthogonal system

We introduce the bi-orthogonal single-particle wave functions,

$$\tilde{\phi}_i(x) \equiv \sum_{j=1}^{A} \psi_j(x)\left\{B^{-1}\right\}_{ji}, \tag{A.3.1}$$

where we define $B_{ij} \equiv \langle\phi_i|\psi_j\rangle$. Here $\tilde{\phi}_j$ and ϕ_i is bi-orthogonal, $\langle\phi_i|\tilde{\phi}_j\rangle = \delta_{ij}$. The Slater-determinant $\tilde{\Psi}$ composed single-particle wave function $\tilde{\phi}_i(x)$ can be written as $\tilde{\Psi} = \Phi \cdot \det B$. Then the matrix element of an operator $\hat{O}$ becomes

$$\langle\Phi|\hat{O}|\Psi\rangle = \langle\Phi|\hat{O}|\tilde{\Phi}\rangle \cdot \det B. \tag{A.3.2}$$

Here, $\langle\Phi|\hat{O}|\Psi\rangle$ can be calculated in the same manner as $\langle\Phi|\hat{O}|\tilde{\Phi}\rangle$.

A.3.1 Off-diagonal matrix elements for Skyrme Hamiltonian

We calculate transitional matrix elements of Skyrme Hamiltonian. We define $\tilde{V}$ by $\tilde{V} = \left\langle\Phi\middle|\hat{V}\middle|\Psi\right\rangle/\mathrm{det}B$ and the following transitional densities,

$$\rho(\vec{r}) = \sum_{i\in p,n}\sum_{\sigma}\phi_i(\vec{r},\sigma)^*\tilde{\psi}_i(\vec{r},\sigma), \tag{A.3.3a}$$

$$\rho^{(\tau)}(\vec{r}) = \sum_{i\in q}\sum_{\sigma}\phi_i(\vec{r},\sigma)\tilde{\psi}_i(\vec{r},\sigma), \tag{A.3.3b}$$

$$\tau(\vec{r}) = \sum_{i\in p,n}\sum_{\sigma}\vec{\nabla}\phi_i(\vec{r},\sigma)\cdot\vec{\nabla}\tilde{\psi}_i(\vec{r},\sigma), \tag{A.3.3c}$$

$$\tau^{(\tau)}(\vec{r}) = \sum_{i\in q}\sum_{\sigma}\vec{\nabla}\phi_i(\vec{r},\sigma)\cdot\vec{\nabla}\tilde{\psi}_i(\vec{r},\sigma), \tag{A.3.3d}$$

$$J_\lambda(\vec{r}) = \sum_{\mu\nu}\epsilon_{\lambda\mu\nu}J_{\mu\nu}(\vec{r}), \tag{A.3.3e}$$

$$J_{\mu\nu}(\vec{r}) = \frac{1}{2i}\sum_{i\in p,n}\sum_{\sigma\sigma'}\{\phi_i^*(\vec{r}\sigma)\partial_\mu\tilde{\psi}_i(\vec{r},\sigma') - (\partial_\mu\phi_i^*(\vec{r},\sigma))\tilde{\psi}_i(\vec{r},\sigma')\}\left\langle\sigma|\sigma_\nu|\sigma'\right\rangle, \tag{A.3.3f}$$

$$J_\lambda^{(\tau)}(\vec{r}) = \sum_{\mu\nu}\epsilon_{\lambda\mu\nu}J_{q\mu\nu}(\vec{r}), \tag{A.3.3g}$$

$$J_{\mu\nu}^{(\tau)}(\vec{r}) = \frac{1}{2i}\sum_{i\in q}\sum_{\sigma\sigma'}\{\phi_i^*(\vec{r},\sigma)\partial_\mu\tilde{\psi}_i(\vec{r},\sigma') - (\partial_\mu\phi_i^*(\vec{r},\sigma))\tilde{\psi}_i(\vec{r},\sigma')\}\left\langle\sigma|\sigma_\nu|\sigma'\right\rangle, \tag{A.3.3h}$$

$$\vec{\rho}(\vec{r}) = \sum_{i\in p,n}\sum_{\sigma\sigma'}\phi_i^*(\vec{r},\sigma)\tilde{\psi}_i(\vec{r},\sigma')\left\langle\sigma|\vec{\sigma}|\sigma'\right\rangle, \tag{A.3.3i}$$

$$\vec{\rho}^{(\tau)}(\vec{r}) = \sum_{i\in q}\sum_{\sigma\sigma'}\phi_i^*(\vec{r},\sigma)\tilde{\psi}_i(\vec{r},\sigma')\left\langle\sigma|\vec{\sigma}|\sigma'\right\rangle, \tag{A.3.3j}$$

$$\vec{j}(\vec{r}) = \frac{1}{2i}\sum_{i\in p,n}\sum_{\sigma}\{\phi_i^*(\vec{r},\sigma)\vec{\nabla}\tilde{\psi}_i(\vec{r},\sigma) - (\vec{\nabla}\phi_i^*(\vec{r},\sigma))\tilde{\psi}_i(\vec{r},\sigma)\}, \tag{A.3.3k}$$

$$\vec{j}^{(\tau)}(\vec{r}) = \frac{1}{2i}\sum_{i\in q}\sum_{\sigma}\{\phi_i^*(\vec{r},\sigma)\vec{\nabla}\tilde{\psi}_i(\vec{r},\sigma) - (\vec{\nabla}\phi_i^*(\vec{r},\sigma))\tilde{\psi}_i(\vec{r},\sigma)\}, \tag{A.3.3l}$$

$$\vec{T}(\vec{r}) = \sum_{i\in p,n}\sum_{\sigma\sigma'}\vec{\nabla}\phi_i^*(\vec{r},\sigma)\cdot\vec{\nabla}\tilde{\psi}_i(\vec{r},\sigma')\left\langle\sigma|\vec{\sigma}|\sigma'\right\rangle, \tag{A.3.3m}$$

$$\vec{T}^{(\tau)}(\vec{r}) = \sum_{i\in q}\sum_{\sigma\sigma'}\vec{\nabla}\phi_i^*(\vec{r},\sigma)\cdot\vec{\nabla}\tilde{\psi}_i(\vec{r},\sigma')\left\langle\sigma|\vec{\sigma}|\sigma'\right\rangle. \tag{A.3.3n}$$

In the following, we show a formula to calculate transitional matrix element of Skyrme interaction, $\langle\Phi|\hat{V}_{Skyrme}|\Psi\rangle$, for each term. Note that the following $\tilde{V}$ is equal to $\left\langle\Phi\middle|\hat{V}\middle|\Phi\right\rangle$ if $\Psi = \Phi(\mathrm{det}B = 1)$.

t_0 term

We introduce the space inversion operator $\hat{P}_r$, the spin exchange operator $\hat{P}_\sigma$, and the isospin exchange operator $\hat{P}_\tau$. Since the Skyrme interaction is δ-type and has no charge mixing, $\hat{P}_r = 1$, $\hat{P}_\tau = \delta_{\sigma_1\sigma_2}$. The t_0 term is calculated as follows:

$$\begin{aligned}
\tilde{V}_0 &= \frac{t_0}{2}\sum_{ij}\langle\phi_i\phi_j|\delta(\vec{r}_1-\vec{r}_2)\left(1+x_0\hat{P}_\sigma\right)\left(1-\hat{P}_r\hat{P}_\tau\hat{P}_\sigma\right)|\tilde{\psi}_i\tilde{\psi}_j\rangle \\
&= \frac{t_0}{2}\sum_{ij}\langle\phi_i\phi_j|\delta(\vec{r}_1-\vec{r}_2)\left[\left(1+\frac{x_0}{2}\right)-\left(\frac{1}{2}+x_0\right)\hat{P}_\tau+\frac{1}{2}\left(x_0-\hat{P}_\tau\right)\vec{\sigma}_1\cdot\vec{\sigma}_2\right]|\tilde{\psi}_i\tilde{\psi}_j\rangle \\
&= \frac{t_0}{2}\int d\vec{r}\Bigg[\left(1+\frac{x_0}{2}\right)\sum_{i,\sigma}\phi_i^*(\vec{r},\sigma)\tilde{\psi}_i(\vec{r},\sigma)\sum_{j\sigma'}\phi_j^*(\vec{r},\sigma')\tilde{\psi}_j(\vec{r},\sigma') \\
&\quad+\frac{x_0}{2}\sum_{\nu}\sum_{i\sigma_1\sigma_1'}\phi_i^*(\vec{r},\sigma_1)\tilde{\psi}_i(\vec{r},\sigma_1')\langle\sigma_1|\sigma_\nu|\sigma_1'\rangle\sum_{j\sigma_2\sigma_2'}\phi_j^*(\vec{r},\sigma_2)\tilde{\psi}_j(\vec{r},\sigma_2')\langle\sigma_2|\sigma_\nu|\sigma_2'\rangle \\
&\quad-\left(\frac{1}{2}+x_0\right)\sum_{\tau}\sum_{i\in\tau,\sigma}\phi_i^*(\vec{r},\sigma)\tilde{\psi}_i(\vec{r},\sigma)\sum_{j\in\tau\sigma'}\phi_j^*(\vec{r},\sigma')\tilde{\psi}_j(\vec{r},\sigma') \\
&\quad-\frac{1}{2}\sum_{\nu}\sum_{\tau}\sum_{i\in\tau\sigma_1\sigma_1'}\phi_i^*(\vec{r},\sigma_1)\tilde{\psi}_i(\vec{r},\sigma_1')\langle\sigma_1|\sigma_\nu|\sigma_1'\rangle\sum_{j\in\tau'\sigma_2\sigma_2'}\phi_j^*(\vec{r},\sigma_2)\tilde{\psi}_j(\vec{r},\sigma_2')\langle\sigma_2|\sigma_\nu|\sigma_2'\rangle\Bigg] \\
&= \frac{t_0}{2}\int d\vec{r}\left[\left(1+\frac{x_0}{2}\right)\rho(\vec{r})^2+\frac{x_0}{2}\vec{\rho}(\vec{r})^2-\sum_{\tau}\left\{\left(\frac{1}{2}+x_0\right)\rho^{(\tau)}(\vec{r})^2-\frac{1}{2}\vec{\rho}^{(\tau)}(\vec{r})^2\right\}\right],
\end{aligned} \tag{A.3.4}$$

where we use $P_\sigma = \frac{1}{2}(1+\vec{\sigma}_1\cdot\vec{\sigma}_2)$.

t_3 term

Similar to the t_0 term, t_3 term is calculated as follows:

$$\begin{aligned}
\tilde{V}_3 &= \frac{t_3}{12}\sum_{ij}\langle\phi_i\phi_j|\rho(\vec{r})^\alpha\delta(\vec{r}_1-\vec{r}_2)\left(1+x_3\hat{P}_\sigma\right)\left(1-\hat{P}_r\hat{P}_\tau\hat{P}_\sigma\right)|\tilde{\psi}_i\tilde{\psi}_j\rangle \\
&= \frac{t_3}{12}\sum_{ij}\int d\vec{r}\langle\phi_i\phi_j|\rho\left(\frac{\vec{r}_1+\vec{r}_2}{2}\right)^\alpha\delta(\vec{r}-\vec{r}_1)\delta(\vec{r}-\vec{r}_2)\left(1+x_3\hat{P}_\sigma\right)\left(1-\hat{P}_r\hat{P}_\tau\hat{P}_\sigma\right)|\tilde{\psi}_i\tilde{\psi}_j\rangle \\
&= \frac{t_3}{12}\sum_{ij}\int d\vec{r}\rho(\vec{r})^\alpha\langle\phi_i\phi_j|\delta(\vec{r}-\vec{r}_1)\delta(\vec{r}-\vec{r}_2)\left(1+x_3\hat{P}_\sigma\right)\left(1-\hat{P}_r\hat{P}_\tau\hat{P}_\sigma\right)|\tilde{\psi}_i\tilde{\psi}_j\rangle \\
&= \frac{t_3}{12}\int d\vec{r}\rho(\vec{r})^\alpha\left[\left(1+\frac{x_3}{2}\right)\rho(\vec{r})^2+\frac{x_3}{2}\vec{\rho}(\vec{r})^2-\sum_{\tau}\left\{\left(\frac{1}{2}+x_3\right)\rho^{(\tau)}(\vec{r})^2-\frac{1}{2}\vec{\rho}^{(\tau)}(\vec{r})^2\right\}\right]
\end{aligned} \tag{A.3.5}$$

t_1 term

We prepare the following equations:

$$\sum_{i\sigma} \phi_i^*(\vec{r}\sigma)\vec{\nabla}\tilde{\psi}_i(\vec{r}\sigma) = \frac{1}{2}\vec{\nabla}\rho(\vec{r}) + i\cdot\vec{j}(\vec{r}), \tag{A.3.6a}$$

$$\sum_{i\sigma} \left(\vec{\nabla}\phi_i^*(\vec{r}\sigma)\right)\tilde{\psi}_i(\vec{r}\sigma) = \frac{1}{2}\vec{\nabla}\rho(\vec{r}) - i\cdot\vec{j}(\vec{r}), \tag{A.3.6b}$$

$$\sum_{i\sigma} \left[\phi_i^*(\vec{r}\sigma)\nabla^2\tilde{\psi}_i(\vec{r}\sigma) + \left(\nabla^2\phi_i^*(\vec{r}\sigma)\right)\tilde{\psi}_i(\vec{r}\sigma)\right] = \nabla^2\rho(\vec{r}) - 2\tau(\vec{r}), \tag{A.3.6c}$$

$$\sum_{i\sigma\sigma'} \phi_i^*(\vec{r}\sigma)\partial_\mu\tilde{\psi}_i(\vec{r}\sigma)\langle\sigma|\sigma_\nu|\sigma'\rangle = \frac{1}{2}\partial_\mu\rho_\nu(\vec{r}) + iJ_{\mu\nu}(\vec{r}), \tag{A.3.6d}$$

$$\sum_{i\sigma\sigma'} \left(\partial_\mu\phi_i^*(\vec{r}\sigma)\right)\tilde{\psi}_i(\vec{r}\sigma)\langle\sigma|\sigma_\nu|\sigma'\rangle = \frac{1}{2}\partial_\mu\rho_\nu(\vec{r}) - iJ_{\mu\nu}(\vec{r}), \tag{A.3.6e}$$

$$\sum_{i\sigma} \left[\phi_i^*(\vec{r}\sigma)\nabla^2\tilde{\psi}_i(\vec{r}\sigma) + \left(\nabla^2\phi_i^*(\vec{r}\sigma)\right)\tilde{\psi}_i(\vec{r}\sigma)\right]\langle\sigma|\sigma_\nu|\sigma'\rangle = \nabla^2\rho_\nu(\vec{r}) - 2T_\nu(\vec{r}). \tag{A.3.6f}$$

The matrix element which contains t_1 term can be written as

$$\begin{aligned}
\tilde{V}_1 &= -\frac{t_1}{16}\sum_{ij}\langle\phi_i\phi_j|\left(1 + x_1\hat{P}_\sigma\right)\Big[\left(\overleftarrow{\nabla}_1^2 + \overleftarrow{\nabla}_2^2 - 2\overleftarrow{\nabla}_1\cdot\overleftarrow{\nabla}_2\right)\delta(\vec{r}_1 - \vec{r}_2) \\
&\qquad + \delta(\vec{r}_1 - \vec{r}_2)\left(\overrightarrow{\nabla}_1^2 + \overrightarrow{\nabla}_2^2 - 2\overrightarrow{\nabla}_1\cdot\overrightarrow{\nabla}_2\right)\Big]\left(1 - \hat{P}_r\hat{P}_\sigma\hat{P}_\tau\right)|\tilde{\psi}_i\tilde{\psi}_j\rangle \\
&= V_1^{(1)} + V_1^{(2)} + V_1^{(3)} + V_1^{(4)},
\end{aligned} \tag{A.3.7}$$

where

$$\begin{aligned}
\tilde{V}_1^{(1)} &= -\frac{t_1}{16}\left(1 + \frac{x_1}{2}\right)\sum_{ij}\langle\phi_i\phi_j|\Big[\left(\overleftarrow{\nabla}_1^2 + \overleftarrow{\nabla}_2^2 - 2\overleftarrow{\nabla}_1\cdot\overleftarrow{\nabla}_2\right)\delta(\vec{r}_1 - \vec{r}_2) \\
&\qquad + \delta(\vec{r}_1 - \vec{r}_2)\left(\overrightarrow{\nabla}_1^2 + \overrightarrow{\nabla}_2^2 - 2\overrightarrow{\nabla}_1\cdot\overrightarrow{\nabla}_2\right)\Big]|\tilde{\psi}_i\tilde{\psi}_j\rangle,
\end{aligned} \tag{A.3.8}$$

$$\begin{aligned}
\tilde{V}_1^{(2)} &= -\frac{t_1}{16}\frac{x_1}{2}\sum_{ij}\langle\phi_i\phi_j|\Big[\left(\overleftarrow{\nabla}_1^2 + \overleftarrow{\nabla}_2^2 - 2\overleftarrow{\nabla}_1\cdot\overleftarrow{\nabla}_2\right)\delta(\vec{r}_1 - \vec{r}_2) \\
&\qquad + \delta(\vec{r}_1 - \vec{r}_2)\left(\overrightarrow{\nabla}_1^2 + \overrightarrow{\nabla}_2^2 - 2\overrightarrow{\nabla}_1\cdot\overrightarrow{\nabla}_2\right)\Big]\vec{\sigma}_1\cdot\vec{\sigma}_2|\tilde{\psi}_i\tilde{\psi}_j\rangle,
\end{aligned} \tag{A.3.9}$$

$$\begin{aligned}
\tilde{V}_1^{(3)} &= \frac{t_1}{16}\left(\frac{1}{2} + x_1\right)\sum_{ij}\langle\phi_i\phi_j|\Big[\left(\overleftarrow{\nabla}_1^2 + \overleftarrow{\nabla}_2^2 - 2\overleftarrow{\nabla}_1\cdot\overleftarrow{\nabla}_2\right)\delta(\vec{r}_1 - \vec{r}_2) \\
&\qquad + \delta(\vec{r}_1 - \vec{r}_2)\left(\overrightarrow{\nabla}_1^2 + \overrightarrow{\nabla}_2^2 - 2\overrightarrow{\nabla}_1\cdot\overrightarrow{\nabla}_2\right)\Big]\hat{P}_r\hat{P}_\tau|\tilde{\psi}_i\tilde{\psi}_j\rangle,
\end{aligned} \tag{A.3.10}$$

$$\tilde{V}_1^{(4)} = \frac{t_1}{16}\frac{1}{2}\sum_{ij}\langle\phi_i\phi_j|\{(\overleftarrow{\nabla}_1^2 + \overleftarrow{\nabla}_2^2 - 2\overleftarrow{\nabla}_1\cdot\overleftarrow{\nabla}_2)\delta(\vec{r}_1 - \vec{r}_2)$$

$$+\delta(\vec{r}_1-\vec{r}_2)(\overrightarrow{\nabla}_1^2+\overrightarrow{\nabla}_2^2-2\overrightarrow{\nabla}_1\cdot\overrightarrow{\nabla}_2)\}\vec{\sigma}_1\cdot\vec{\sigma}_2\hat{P}_r\hat{P}_\tau\big|\tilde{\psi}_i\tilde{\psi}_j\rangle. \tag{A.3.11}$$

The $V_1^{(1)}$, $V_1^{(2)}$, $V_1^{(3)}$, and $V_1^{(4)}$ are calculated as follows

$$\begin{aligned}
\tilde{V}_1^{(1)} &= -\frac{t_1}{16}\left(1+\frac{x_1}{2}\right)\int d\vec{r}\\
&\Bigg[\sum_{i\sigma_1}\Big\{\left(\nabla^2\phi_i^*(\vec{r}\sigma_1)\right)\tilde{\psi}_i(\vec{r}\sigma_1)+\phi_i^*(\vec{r}\sigma_1)\left(\nabla^2\tilde{\psi}_i(\vec{r}\sigma_1)\right)\Big\}\sum_{j\sigma_2}\phi_j^*(\vec{r}\sigma_2)\tilde{\psi}_j(\vec{r}\sigma_2)\\
&+\sum_{i\sigma_1}\phi_i^*(\vec{r}\sigma_1)\tilde{\psi}_j(\vec{r}\sigma_1)\sum_{j\sigma_2}\Big\{\left(\nabla^2\phi_j^*(\vec{r}\sigma_2)\right)\tilde{\psi}_j(\vec{r}\sigma_2)+\phi_j^*(\vec{r}\sigma_2)\left(\nabla^2\tilde{\psi}_j(\vec{r}\sigma_2)\right)\Big\}\\
&-2\Big\{\sum_{i\sigma_1}\left(\vec{\nabla}\phi_i^*(\vec{r}\sigma_1)\right)\tilde{\psi}_i(\vec{r}\sigma_1)\sum_{j\sigma_2}\left(\vec{\nabla}\phi_j^*(\vec{r}\sigma_2)\right)\tilde{\psi}_j(\vec{r}\sigma_2)\\
&+\sum_{i\sigma_1}\phi_i^*(\vec{r}\sigma_1)\left(\vec{\nabla}\tilde{\psi}_i(\vec{r}\sigma_1)\right)\sum_{j\sigma_2}\phi_j^*(\vec{r}\sigma_2)\left(\vec{\nabla}\tilde{\psi}_j(\vec{r}\sigma_2)\right)\Big\}\Bigg]\\
&= -\frac{t_1}{16}\left(1+\frac{x_1}{2}\right)\int d\vec{r}\Bigg[\left(\nabla^2\rho(\vec{r})-2\tau(\vec{r})\right)\rho(\vec{r})+\rho(\vec{r})\left(\nabla^2\rho(\vec{r})-2\tau(\vec{r})\right)\\
&-2\left(\frac{1}{2}\vec{\nabla}\rho(\vec{r})-i\vec{j}(\vec{r})\right)^2-2\left(\frac{1}{2}\vec{\nabla}\rho(\vec{r})+i\vec{j}(\vec{r})\right)^2\Bigg]\\
&= \frac{t_1}{16}\left(1+\frac{x_1}{2}\right)\int d\vec{r}\Bigg[4\left(\rho(\vec{r})\tau(\vec{r})-\vec{j}(\vec{r})^2\right)-3\rho(\vec{r})\nabla^2\rho(\vec{r})\Bigg].
\end{aligned} \tag{A.3.12}$$

$$\begin{aligned}
V_1^{(2)} &= \frac{t_1}{32}\int d\vec{r}\Bigg[\\
&\sum_{i\sigma_1\sigma_1'}\Big\{\left(\nabla^2\phi_i^*(\vec{r}\sigma_1)\right)\tilde{\psi}_i(\vec{r}\sigma_1)+\phi_i^*(\vec{r}\sigma_1)\left(\nabla^2\tilde{\psi}_i(\vec{r}\sigma_1)\right)\Big\}\langle\sigma_1|\vec{\sigma}|\sigma_1'\rangle\cdot\sum_{j\sigma_2\sigma_2'}\phi_j^*(\vec{r}\sigma_2)\tilde{\psi}_j(\vec{r}\sigma_2)\langle\sigma_2|\vec{\sigma}|\sigma_2'\rangle\\
&+\sum_{i\sigma_1\sigma_1'}\phi_i^*(\vec{r}\sigma_1)\tilde{\psi}_j(\vec{r}\sigma_1)\langle\sigma_1|\vec{\sigma}|\sigma_1'\rangle\cdot\sum_{j\sigma_2\sigma_2'}\Big\{\left(\nabla^2\phi_j^*(\vec{r}\sigma_2)\right)\tilde{\psi}_j(\vec{r}\sigma_2)+\phi_j^*(\vec{r}\sigma_2)(\nabla^2\tilde{\psi}_j(\vec{r}\sigma_2))\Big\}\langle\sigma_2|\sigma|\sigma_2'\rangle\\
&-2\Big\{\sum_{i\sigma_1\sigma_1'}\left(\vec{\nabla}\phi_i^*(\vec{r}\sigma_1)\right)\tilde{\psi}_i(\vec{r}\sigma_1)\langle\sigma_1|\sigma|\sigma_1'\rangle\cdot\sum_{j\sigma_2\sigma_2'}\left(\vec{\nabla}\phi_j^*(\vec{r}\sigma_2)\right)\tilde{\psi}_j(\vec{r}\sigma_2)\langle\sigma_2|\vec{\sigma}|\sigma_2'\rangle\\
&+\sum_{i\sigma_1\sigma_1'}\phi_i^*(\vec{r}\sigma_1)\left(\vec{\nabla}\tilde{\psi}_i(\vec{r}\sigma_1)\right)\langle\sigma_1|\vec{\sigma}|\sigma_1'\rangle\cdot\sum_{j\sigma_2\sigma_2'}\phi_j^*(\vec{r}\sigma_2)(\vec{\nabla}\tilde{\psi}_j(\vec{r}\sigma_2))\Big\}\langle\sigma_2|\vec{\sigma}|\sigma_2'\rangle\Bigg]\\
&= -\frac{t_1}{32}x_1\int d\vec{r}\Bigg[\left(\nabla^2\vec{\rho}(\vec{r})-2\vec{T}(\vec{r})\right)\cdot\vec{\rho}(\vec{r})+\vec{\rho}(\vec{r})\cdot\left(\nabla^2\vec{\rho}(\vec{r})-2\vec{T}(\vec{r})\right)\\
&\qquad-2\Big\{\Big\{\sum_{\mu\nu}\left(\frac{1}{2}\partial_\mu\rho_\nu(\vec{r})-iJ_{\mu\nu}(\vec{r})\right)\Big\}^2+\Big\{\sum_{\mu\nu}(\frac{1}{2}\partial_\mu\rho_\nu(\vec{r})+iJ_{\mu\nu}(\vec{r}))\Big\}^2\Big\}\Bigg]\\
&= \frac{t_1}{32}x_1\int d\vec{r}\Bigg[4\left(\vec{\rho}(\vec{r})\cdot\vec{T}(\vec{r})-\sum_{\mu\nu}J_{\mu\nu}(\vec{r})^2\right)-3\vec{\rho}(\vec{r})\cdot\nabla^2\vec{\rho}(\vec{r})\Bigg]
\end{aligned} \tag{A.3.13}$$

$$
\begin{aligned}
\tilde{V}_1^{(3)} \;=\;& -\frac{t_1}{16}\left(\frac{1}{2}+x_1\right)\sum_{\tau}\int d\vec{r}\Bigg[\\
& \sum_{i\in\tau\sigma_1}\Big\{\left(\nabla^2\phi_i^*(\vec{r}\sigma_1)\right)\tilde{\psi}_i(\vec{r}\sigma_1)+\phi_i^*(\vec{r}\sigma_1)\left(\nabla^2\tilde{\psi}_i(\vec{r}\sigma_1)\right)\Big\}\sum_{j\in\tau\sigma_2}\phi_j^*(\vec{r}\sigma_2)\tilde{\psi}_j(\vec{r}\sigma_2)\\
& +\sum_{i\in\tau\sigma_1}\phi_i^*(\vec{r}\sigma_1)\tilde{\psi}_j(\vec{r}\sigma_1)\sum_{j\in\tau\sigma_2}\Big\{\left(\nabla^2\phi_j^*(\vec{r}\sigma_2)\right)\tilde{\psi}_j(\vec{r}\sigma_2)+\phi_j^*(\vec{r}\sigma_2)\left(\nabla^2\tilde{\psi}_j(\vec{r}\sigma_2)\right)\Big\}\\
& -2\Big\{\sum_{i\in\tau\sigma_1}\left(\vec{\nabla}\phi_i^*(\vec{r}\sigma_1)\right)\tilde{\psi}_i(\vec{r}\sigma_1)\sum_{j\in\tau\sigma_2}\left(\vec{\nabla}\phi_j^*(\vec{r}\sigma_2)\right)\tilde{\psi}_j(\vec{r}\sigma_2)\\
& +\sum_{i\in\tau\sigma_1}\phi_i^*(\vec{r}\sigma_1)\left(\vec{\nabla}\tilde{\psi}_i(\vec{r}\sigma_1)\right)\sum_{j\in\tau\sigma_2}\phi_j^*(\vec{r}\sigma_2)\left(\vec{\nabla}\tilde{\psi}_j(\vec{r}\sigma_2)\right)\Big\}\Bigg]\\
=\;& -\frac{t_1}{16}(\frac{1}{2}+x_1)\int d\vec{r}\Bigg[\left(\nabla^2\rho(\vec{r})-2\tau(\vec{r})\right)\rho(\vec{r})+\rho(\vec{r})\left(\nabla^2\rho(\vec{r})-2\tau(\vec{r})\right)\\
& \qquad -2\left(\frac{1}{2}\vec{\nabla}\rho(\vec{r})-i\vec{j}(\vec{r})\right)^2-2\left(\frac{1}{2}\vec{\nabla}\rho(\vec{r})+i\vec{j}(\vec{r})\right)^2\Bigg]\\
=\;& \frac{t_1}{16}\left(\frac{1}{2}+x_1\right)\int d\vec{r}\Bigg[4\left(\rho^{(\tau)}(\vec{r})\tau^{(\tau)}(\vec{r})-\vec{j}^{(\tau)}(\vec{r})^2\right)-3\rho^{(\tau)}(\vec{r})\nabla^2\rho^{(\tau)}(\vec{r})\Bigg]
\end{aligned}
\tag{A.3.14}
$$

$$
\begin{aligned}
\tilde{V}_1^{(4)} \;&=-\frac{t_1}{32}x_1\sum_{\tau}\int d\vec{r}\Bigg[\\
& \sum_{i\in\tau\sigma_1\sigma_1'}\Big\{\left(\nabla^2\phi_i^*(\vec{r}\sigma_1)\right)\tilde{\psi}_i(\vec{r}\sigma_1)+\phi_i^*(\vec{r}\sigma_1)\left(\nabla^2\tilde{\psi}_i(\vec{r}\sigma_1)\right)\Big\}\langle\sigma_1|\vec{\sigma}|\sigma_1'\rangle\cdot\sum_{j\in\tau\sigma_2\sigma_2'}\phi_j^*(\vec{r}\sigma_2)\tilde{\psi}_j(\vec{r}\sigma_2)\langle\sigma_2|\vec{\sigma}|\sigma_2'\rangle\\
& +\sum_{i\in\tau\sigma_1\sigma_1'}\phi_i^*(\vec{r}\sigma_1)\tilde{\psi}_j(\vec{r}\sigma_1)\langle\sigma_1|\vec{\sigma}|\sigma_1'\rangle\cdot\sum_{j\in\tau\sigma_2\sigma_2'}\Big\{(\nabla^2\phi_j^*(\vec{r}\sigma_2))\tilde{\psi}_j(\vec{r}\sigma_2)+\phi_j^*(\vec{r}\sigma_2)(\nabla^2\tilde{\psi}_j(\vec{r}\sigma_2))\Big\}\langle\sigma_2|\sigma|\sigma_2'\rangle\\
& -2\Big\{\sum_{i\in\tau\sigma_1\sigma_1'}(\vec{\nabla}\phi_i^*(\vec{r}\sigma_1))\tilde{\psi}_i(\vec{r}\sigma_1)\langle\sigma_1|\sigma|\sigma_1'\rangle\cdot\sum_{j\in\tau\sigma_2\sigma_2'}(\vec{\nabla}\phi_j^*(\vec{r}\sigma_2))\tilde{\psi}_j(\vec{r}\sigma_2)\langle\sigma_2|\vec{\sigma}|\sigma_2'\rangle\\
& +\sum_{i\in\tau\sigma_1\sigma_1'}\phi_i^*(\vec{r}\sigma_1)\left(\vec{\nabla}\tilde{\psi}_i(\vec{r}\sigma_1)\right)\langle\sigma_1|\vec{\sigma}|\sigma_1'\rangle\cdot\sum_{j\in\tau\sigma_2\sigma_2'}\phi_j^*(\vec{r}\sigma_2)\left(\nabla\tilde{\psi}_j(\vec{r}\sigma_2)\right)\Big\}\langle\sigma_2|\vec{\sigma}|\sigma_2'\rangle\Bigg]\\
&=-\frac{t_1}{32}x_1\sum_{\tau}\int d\vec{r}\Bigg[\left(\nabla^2\vec{\rho}(\vec{r})-2\vec{T}(\vec{r})\right)\cdot\vec{\rho}(\vec{r})+\vec{\rho}(\vec{r})\cdot\left(\nabla^2\vec{\rho}(\vec{r})-2\vec{T}(\vec{r})\right)\\
& \qquad -2\Big\{\Big\{\sum_{\mu\nu}\left(\frac{1}{2}\partial_\mu\rho_\nu(\vec{r})-iJ_{\mu\nu}(\vec{r})\right)\Big\}^2+\Big\{\sum_{\mu\nu}\left(\frac{1}{2}\partial_\mu\rho_\nu(\vec{r})+iJ_{\mu\nu}(\vec{r})\right)\Big\}^2\Big\}\Bigg]\\
&=\frac{t_1}{32}x_1\sum_{\tau}\int d\vec{r}\Bigg[4\left(\vec{\rho}^{(\tau)}(\vec{r})\cdot\vec{T}^{(\tau)}(\vec{r})-\sum_{\mu\nu}J_{\mu\nu}^{(\tau)}(\vec{r})^2\right)-3\vec{\rho}^{(\tau)}(\vec{r})\cdot\nabla^2\vec{\rho}^{(\tau)}(\vec{r})\Bigg],
\end{aligned}
\tag{A.3.15}
$$

$$
\tilde{V}_1 \;=\frac{t_1}{4}\int d\vec{r}\Bigg[(1+\frac{x_1}{2})\left(\rho(\vec{r})\tau(\vec{r})-\vec{j}(\vec{r})^2\right)-\frac{3}{4}\left(1+\frac{x_1}{2}\right)\rho(\vec{r})\nabla^2\rho(\vec{r})
$$

$$
\begin{aligned}
&+\frac{x_1}{2}\left(\vec{\rho}(\vec{r})\cdot\vec{T}(\vec{r})-\sum_{\mu\nu}J_{\mu\nu}(\vec{r})^2\right)-\frac{3}{8}x_1\vec{\rho}(\vec{r})\cdot\nabla^2\vec{\rho}(\vec{r})\Bigg]\\
&-\frac{t_1}{4}\sum_{\tau}\int d\vec{r}\Bigg[\left(\frac{1}{2}+x_1\right)\left(\rho^{(\tau)}(\vec{r})\tau^{(\tau)}(\vec{r})-\vec{j}^{(\tau)}(\vec{r})^2\right)-\frac{3}{4}\left(\frac{1}{2}+x_1\right)\rho^{(\tau)}(\vec{r})\nabla^2\rho^{(\tau)}(\vec{r})\\
&+\frac{1}{2}\left(\vec{\rho}^{(\tau)}(\vec{r})\cdot\vec{T}^{(\tau)}(\vec{r})-\sum_{\mu\nu}J^{(\tau)}_{\mu\nu}(\vec{r})^2\right)-\frac{3}{8}\vec{\rho}^{(\tau)}(\vec{r})\cdot\nabla^2\vec{\rho}^{(\tau)}(\vec{r})\Bigg]
\end{aligned}
\tag{A.3.16}
$$

t_2 **term**

$$
\begin{aligned}
\tilde{V}_2 &= -\frac{t_2}{8}\sum_{ij}\langle\phi_i\phi_j\big|(1+x_1\hat{P}_\sigma)(\overleftarrow{\nabla}_1-\overleftarrow{\nabla}_2)\delta(\vec{r}_1-\vec{r}_2)\cdot(\overrightarrow{\nabla}_1-\overrightarrow{\nabla}_2)(1-\hat{P}_r\hat{P}_\sigma\hat{P}_\tau)\big|\tilde{\psi}_i\tilde{\psi}_j\rangle\\
&= \tilde{V}_2^{(1)}+\tilde{V}_2^{(2)}+\tilde{V}_2^{(3)}+\tilde{V}_2^{(4)},
\end{aligned}
\tag{A.3.17}
$$

where

$$\tilde{V}_2^{(1)} = -\frac{t_2}{8}\left(1+\frac{x_2}{2}\right)\sum_{ij}\langle\phi_i\phi_j\big|\left(\overleftarrow{\nabla}_1-\overleftarrow{\nabla}_2\right)\delta(\vec{r}_1-\vec{r}_2)\cdot\left(\overrightarrow{\nabla}_1-\overrightarrow{\nabla}_2\right)\big|\tilde{\psi}_i\tilde{\psi}_j\rangle \tag{A.3.18a}$$

$$\tilde{V}_2^{(2)} = \frac{t_2}{8}\frac{x_2}{2}\sum_{ij}\langle\phi_i\phi_j\big|\left(\overleftarrow{\nabla}_1-\overleftarrow{\nabla}_2\right)\delta(\vec{r}_1-\vec{r}_2)\cdot\left(\overrightarrow{\nabla}_1-\overrightarrow{\nabla}_2\right)\vec{\sigma}_1\cdot\vec{\sigma}_2\big|\tilde{\psi}_i\tilde{\psi}_j\rangle \tag{A.3.18b}$$

$$\tilde{V}_2^{(3)} = -\frac{t_2}{8}\left(\frac{1}{2}+x_2\right)\sum_{ij}\langle\phi_i\phi_j\big|\left(\overleftarrow{\nabla}_1-\overleftarrow{\nabla}_2\right)\delta(\vec{r}_1-\vec{r}_2)\cdot\left(\overrightarrow{\nabla}_1-\overrightarrow{\nabla}_2\right)\hat{P}_r\hat{P}_\tau\big|\tilde{\psi}_i\tilde{\psi}_j\rangle, \tag{A.3.18c}$$

$$\tilde{V}_2^{(4)} = -\frac{t_2}{8}\frac{1}{2}\sum_{ij}\langle\phi_i\phi_j\big|\left(\overleftarrow{\nabla}_1-\overleftarrow{\nabla}_2\right)\delta(\vec{r}_1-\vec{r}_2)\cdot\left(\overrightarrow{\nabla}_1-\overrightarrow{\nabla}_2\right)\vec{\sigma}_1\cdot\vec{\sigma}_2\hat{P}_r\hat{P}_\tau\big|\tilde{\psi}_i\tilde{\psi}_j\rangle. \tag{A.3.18d}$$

$$
\begin{aligned}
\tilde{V}_2^{(1)} &= \frac{t_2}{8}\left(1+\frac{x_2}{2}\right)\int d\vec{r}\Bigg[\sum_{i\sigma_1}\left(\vec{\nabla}\phi_i^*(\vec{r}\sigma_1)\right)\cdot\left(\vec{\nabla}\tilde{\psi}_i(\vec{r}\sigma_1)\right)\sum_{j\sigma_2}\phi_j^*(\vec{r}\sigma_2)\tilde{\psi}_j(\vec{r}\sigma_2)\\
&-\sum_{i\sigma_1}\left(\vec{\nabla}\phi_i^*(\vec{r}\sigma_1)\right)\tilde{\psi}_i(\vec{r}\sigma_1)\cdot\sum_{j\sigma_2}\phi_j^*(\vec{r}\sigma_2)\left(\vec{\nabla}\tilde{\psi}_j(\vec{r}\sigma_2)\right)\\
&-\sum_{i\sigma_1}\phi_i^*(\vec{r}\sigma_1)\left(\vec{\nabla}\tilde{\psi}_j(\vec{r}\sigma_1)\right)\cdot\sum_{j\sigma_2}\left(\vec{\nabla}\phi_j^*(\vec{r}\sigma_2)\right)\tilde{\psi}_j(\vec{r}\sigma_2)\\
&+\sum_{i\sigma_1}\phi_i^*(\vec{r}\sigma_1)\tilde{\psi}_i(\vec{r}\sigma_1)\sum_{j\sigma_2}\left(\vec{\nabla}\phi_j^*(\vec{r}\sigma_2)\right)\cdot\left(\vec{\nabla}\tilde{\psi}_j(\vec{r}\sigma_2)\right)\Bigg]\\
&= \frac{t_2}{8}(1+\frac{x_2}{2})\int d\vec{r}\Bigg[\tau(\vec{r})\rho(\vec{r})-(\frac{1}{2}\vec{\nabla}\rho(\vec{r})-i\vec{j}(\vec{r}))(\frac{1}{2}\vec{\nabla}\rho(\vec{r})+i\vec{j}(\vec{r}))\\
&-\left(\frac{1}{2}\vec{\nabla}\rho(\vec{r})+i\vec{j}(\vec{r})\right)\left(\frac{1}{2}\vec{\nabla}\rho(\vec{r})-i\vec{j}(\vec{r})\right)+\rho(\vec{r})\tau(\vec{r})\Bigg]
\end{aligned}
$$

$$= \frac{t_2}{4}(1+\frac{x_2}{2})\int d\vec{r}\Big[\Big(\rho(\vec{r})\tau(\vec{r}) - \vec{j}(\vec{r})^2\Big) + \frac{1}{4}\rho(\vec{r})\nabla^2\rho(\vec{r})\Big] \tag{A.3.19}$$

$$\begin{aligned}
&\tilde{V}_2^{(2)} \\
=\ & \frac{t_2}{16}x_2\int d\vec{r}\Bigg[\sum_{i\sigma_1\sigma_1'}\Big(\vec{\nabla}\phi_i^*(\vec{r}\sigma_1)\Big)\cdot\Big(\vec{\nabla}\tilde{\psi}_i(\vec{r}\sigma_1')\Big)\langle\sigma_1|\vec{\sigma}|\sigma_1'\rangle\sum_{j\sigma_2\sigma_2'}\phi_j^*(\vec{r}\sigma_2)\tilde{\psi}_j(\vec{r}\sigma_2')\langle\sigma_2|\vec{\sigma}|\sigma_2'\rangle \\
&-\sum_{i\sigma_1\sigma_1'}\Big(\vec{\nabla}\phi_i^*(\vec{r}\sigma_1)\Big)\tilde{\psi}_i(\vec{r}\sigma_1')\langle\sigma_1|\vec{\sigma}|\sigma_1'\rangle\cdot\sum_{j\sigma_2\sigma_2'}\phi_j^*(\vec{r}\sigma_2)\Big(\vec{\nabla}\tilde{\psi}_j(\vec{r}\sigma_2')\Big)\langle\sigma_2|\vec{\sigma}|\sigma_2'\rangle \\
&-\sum_{i\sigma_1\sigma_1'}\phi_i^*(\vec{r}\sigma_1)\Big(\vec{\nabla}\tilde{\psi}_i(\vec{r}\sigma_1')\Big)\langle\sigma_1|\vec{\sigma}|\sigma_1'\rangle\cdot\sum_{j\sigma_2\sigma_2'}\Big(\vec{\nabla}\phi_j^*(\vec{r}\sigma_2)\Big)\tilde{\psi}_j(\vec{r}\sigma_2')\langle\sigma_2|\vec{\sigma}|\sigma_2'\rangle \\
&+\sum_{i\sigma_1\sigma_1'}\phi_i^*(\vec{r}\sigma_1)\tilde{\psi}_i(\vec{r}\sigma_1')\langle\sigma_1|\vec{\sigma}|\sigma_1'\rangle\sum_{j\sigma_2\sigma_2'}(\vec{\nabla}\phi_j^*(\vec{r}\sigma_2))\cdot\Big(\vec{\nabla}\tilde{\psi}_j(\vec{r}\sigma_2')\Big)\langle\sigma_2|\vec{\sigma}|\sigma_2'\rangle\Bigg] \\
&= \frac{t_2}{16}x_2\int d\vec{r}\Bigg[\vec{T}(\vec{r})\cdot\vec{\rho}(\vec{r}) - \sum_{\mu\nu}\Big(\frac{1}{2}\partial_\mu\rho_\nu - iJ_{\mu\nu}(\vec{r})\Big)\Big(\frac{1}{2}\partial_\mu\rho_\nu + iJ_{\mu\nu}(\vec{r})\Big) \\
&-\sum_{\mu\nu}\Big(\frac{1}{2}\partial_\mu\rho_\nu + iJ_{\mu\nu}(\vec{r})\Big)\Big(\frac{1}{2}\partial_\mu\rho_\nu - iJ_{\mu\nu}(\vec{r})\Big) + \vec{\rho}(\vec{r})\cdot\vec{T}(\vec{r})\Bigg] \\
&= \frac{t_2}{8}x_2\int d\vec{r}\Bigg[\Bigg(\vec{\rho}(\vec{r})\cdot\vec{T}(\vec{r}) - \sum_{\mu\nu}J_{\mu\nu}^2\Bigg) + \frac{1}{4}\vec{\rho}(\vec{r})\cdot\nabla^2\vec{\rho}(\vec{r})\Bigg],
\end{aligned} \tag{A.3.20}$$

$$\begin{aligned}
\tilde{V}_2^{(3)} &= \frac{t_2}{8}(\frac{1}{2}+x_2)\int d\vec{r}\Bigg[\sum_{i\sigma_1\sigma_1'}\Big(\vec{\nabla}\phi_i^*(\vec{r}\sigma_1)\Big)\cdot\Big(\vec{\nabla}\tilde{\psi}_i(\vec{r}\sigma_1')\Big)\sum_{j\sigma_2\sigma_2'}\phi_j^*(\vec{r}\sigma_2)\tilde{\psi}_j(\vec{r}\sigma_2') \\
&\quad-\sum_{i\sigma_1\sigma_1'}\Big(\vec{\nabla}\phi_i^*(\vec{r}\sigma_1)\Big)\tilde{\psi}_i(\vec{r}\sigma_1')\cdot\sum_{j\sigma_2\sigma_2'}\phi_j^*(\vec{r}\sigma_2)\Big(\vec{\nabla}\tilde{\psi}_j(\vec{r}\sigma_2')\Big) \\
&\quad-\sum_{i\sigma_1\sigma_1'}\phi_i^*(\vec{r}\sigma_1)\Big(\vec{\nabla}\tilde{\psi}_i(\vec{r}\sigma_1')\Big)\cdot\sum_{j\sigma_2\sigma_2'}\Big(\vec{\nabla}\phi_j^*(\vec{r}\sigma_2)\Big)\tilde{\psi}_j(\vec{r}\sigma_2') \\
&\quad+\sum_{i\sigma_1\sigma_1'}\phi_i^*(\vec{r}\sigma_1)\tilde{\psi}_i(\vec{r}\sigma_1')\sum_{j\sigma_2\sigma_2'}\Big(\vec{\nabla}\phi_j^*(\vec{r}\sigma_2)\Big)\cdot\Big(\vec{\nabla}\tilde{\psi}_j(\vec{r}\sigma_2')\Big)\Bigg] \\
&= \frac{t_2}{8}\Big(\frac{1}{2}+x_2\Big)\sum_\tau\int d\vec{r}\Bigg[\tau^{(\tau)}(\vec{r})\rho^{(\tau)}(\vec{r}) - \Big(\frac{1}{2}\vec{\nabla}\rho^{(\tau)}(\vec{r}) - i\vec{j}^{(\tau)}(\vec{r})\Big)\Big(\frac{1}{2}\vec{\nabla}\rho^{(\tau)}(\vec{r}) + i\vec{j}^{(\tau)}(\vec{r})\Big) \\
&\quad-(\frac{1}{2}\vec{\nabla}\rho^{(\tau)}(\vec{r}) + i\vec{j}^{(\tau)}(\vec{r}))(\frac{1}{2}\vec{\nabla}\rho^{(\tau)}(\vec{r}) - i\vec{j}^{(\tau)}(\vec{r})) + \rho^{(\tau)}(\vec{r})\tau^{(\tau)}(\vec{r}))\Bigg] \\
&= \frac{t_2}{4}(1+\frac{x_2}{2})\sum_\tau\int d\vec{r}\Big[(\rho^{(\tau)}(\vec{r})\tau^{(\tau)}(\vec{r}) - \vec{j}^{(\tau)}(\vec{r})^2) + \frac{1}{4}\rho^{(\tau)}(\vec{r})\nabla^2\rho^{(\tau)}(\vec{r})\Big],
\end{aligned} \tag{A.3.21}$$

$$\begin{aligned}
\tilde{V}_2^{(4)} &= -\frac{t_2}{16}\int d\vec{r}_1 d\vec{r}_2 \Bigg[\sum_{i\sigma_1\sigma_1'} \Big\{ \left(\vec{\nabla}\phi_i^*(\vec{r}_1\sigma_1)\right)\tilde{\psi}_i(\vec{r}\sigma_2) - \phi_i^*(\vec{r}\sigma_1)\left(\vec{\nabla}\tilde{\psi}_i(\vec{r}\sigma_2)\right) \Big\} \langle\sigma_1|\vec{\sigma}|\sigma_1'\rangle \\
&\quad \sum_{j\sigma_2\sigma_2'} \big\{ (\vec{\nabla}\phi_i^*(\vec{r}_1\sigma_1))\tilde{\psi}_i(\vec{r}\sigma_2) - \phi_i^*(\vec{r}\sigma_1)(\vec{\nabla}\tilde{\psi}_i(\vec{r}\sigma_2)) \big\} \langle\sigma_2|\vec{\sigma}|\sigma_2'\rangle \Bigg] \\
&= \frac{t_2}{16}\int d\vec{r} \Bigg[\sum_{i\sigma_1\sigma_1'} \left(\vec{\nabla}\phi_i^*(\vec{r}\sigma_1)\right) \cdot \left(\vec{\nabla}\tilde{\psi}_i(\vec{r}\sigma_1')\right) \langle\sigma_1|\vec{\sigma}|\sigma_1'\rangle \sum_{j\sigma_2\sigma_2'} \phi_j^*(\vec{r}\sigma_2)\tilde{\psi}_j(\vec{r}\sigma_2')\langle\sigma_2|\vec{\sigma}|\sigma_2'\rangle \\
&\qquad - \sum_{i\sigma_1\sigma_1'} \left(\vec{\nabla}\phi_i^*(\vec{r}\sigma_1)\right)\tilde{\psi}_i(\vec{r}\sigma_1')\langle\sigma_1|\vec{\sigma}|\sigma_1'\rangle \cdot \sum_{j\sigma_2\sigma_2'} \phi_j^*(\vec{r}\sigma_2)\left(\vec{\nabla}\tilde{\psi}_j(\vec{r}\sigma_2')\right)\langle\sigma_2|\vec{\sigma}|\sigma_2'\rangle \\
&\qquad - \sum_{i\sigma_1\sigma_1'} \phi_i^*(\vec{r}\sigma_1)\left(\vec{\nabla}\tilde{\psi}_i(\vec{r}\sigma_1')\right)\langle\sigma_1|\vec{\sigma}|\sigma_1'\rangle \cdot \sum_{j\sigma_2\sigma_2'} \left(\vec{\nabla}\phi_j^*(\vec{r}\sigma_2)\right)\tilde{\psi}_j(\vec{r}\sigma_2')\langle\sigma_2|\vec{\sigma}|\sigma_2'\rangle \\
&\qquad + \sum_{i\sigma_1\sigma_1'} \phi_i^*(\vec{r}\sigma_1)\tilde{\psi}_i(\vec{r}\sigma_1')\langle\sigma_1|\vec{\sigma}|\sigma_1'\rangle \sum_{j\sigma_2\sigma_2'} \left(\vec{\nabla}\phi_j^*(\vec{r}\sigma_2)\right) \cdot \left(\vec{\nabla}\tilde{\psi}_j(\vec{r}\sigma_2')\right)\langle\sigma_2|\vec{\sigma}|\sigma_2'\rangle \Bigg] \\
&= \frac{t_2}{16}\sum_\tau \int d\vec{r} \Bigg[\vec{T}^{(\tau)}(\vec{r}) \cdot \vec{\rho}^{(\tau)}(\vec{r}) - \sum_{\mu\nu} (\frac{1}{2}\partial_\mu\rho_\nu^{(\tau)} - iJ_{\mu\nu}^{(\tau)}(\vec{r}))(\frac{1}{2}\partial_\mu\rho_\nu^{(\tau)} + iJ_{\mu\nu}^{(\tau)}(\vec{r})) \\
&\quad - \sum_{\mu\nu} (\frac{1}{2}\partial_\mu\rho_\nu^{(\tau)} + iJ_{\mu\nu}^{(\tau)}(\vec{r}))(\frac{1}{2}\partial_\mu\rho_\nu^{(\tau)} - iJ_{\mu\nu}^{(\tau)}(\vec{r})) + \vec{\rho}^{(\tau)}(\vec{r}) \cdot \vec{T}^{(\tau)}(\vec{r}) \Bigg] \\
&= \frac{t_2}{8}\sum_\tau \int d\vec{r} \Bigg[\left(\vec{\rho}^{(\tau)}(\vec{r}) \cdot \vec{T}^{(\tau)}(\vec{r}) - \sum_{\mu\nu} J_{\mu\nu}^{(\tau)2} \right) + \frac{1}{4}\vec{\rho}^{(\tau)}(\vec{r}) \cdot \nabla^2\vec{\rho}^{(\tau)}(\vec{r}) \Bigg] \qquad \text{(A.3.22)}
\end{aligned}$$

Finally we can write t_2 term as

$$\begin{aligned}
\tilde{V}_2 &= \frac{t_2}{4}\int d\vec{r} \Bigg[\frac{1}{4}\left(1+\frac{x_2}{2}\right)\rho\nabla^2\rho + \frac{x_2}{2}\left(\vec{\rho}\cdot\vec{T} - \sum_{\mu\nu} J_{\mu\nu}^2 \right) \\
&\quad + \left(1+\frac{x_2}{2}\right)\left(\rho\tau - \vec{j}^2\right) + \frac{x_2}{8}\vec{\rho}\cdot\nabla^2\vec{\rho} \Bigg] \\
&+ \frac{t_2}{4}\sum_\tau \int d\vec{r} \Bigg[\frac{1}{4}(\frac{1}{2}+x_2)\rho^{(\tau)}\nabla^2\rho^{(\tau)} + \frac{1}{2}\left(\vec{\rho}^{(\tau)}\cdot\vec{T}^{(\tau)} - \sum_{\mu\nu} J_{\mu\nu}^{(\tau)2} \right) \\
&\quad + \left(\frac{1}{2}+x_2\right)\left(\rho^{(\tau)}\tau^{(\tau)} - \vec{j}^{(\tau)2}\right) + \frac{1}{8}\vec{\rho}^{(\tau)}\cdot\nabla^2\vec{\rho}^{(\tau)} \Bigg]. \qquad \text{(A.3.23)}
\end{aligned}$$

W_0 term

We use following equations:

$$i\vec{\nabla}\times\vec{j} = \frac{1}{2}\sum_{i\sigma} \Big\{ \left(\vec{\nabla}\phi_i^*(\vec{r}\sigma)\right)\times\left(\vec{\nabla}\tilde{\psi}_i(\vec{r}\sigma)\right) + \left(\vec{\nabla}\phi_i^*(\vec{r}\sigma)\right)\times\left(\vec{\nabla}\tilde{\psi}_i(\vec{r}\sigma)\right)$$

$$\begin{aligned}
& +\phi_i^*(\vec{r}\sigma)\left(\vec{\nabla}\times\vec{\nabla}\tilde{\psi}_i(\vec{r}\sigma)\right)+\left(\vec{\nabla}\times\vec{\nabla}\phi_i^*(\vec{r}\sigma)\right)\tilde{\psi}_i(\vec{r}\sigma))\} \\
= & \sum_{i\sigma}\left(\vec{\nabla}\phi_i^*(\vec{r}\sigma)\right)\times\left(\vec{\nabla}\tilde{\psi}_i(\vec{r}\sigma)\right) \qquad \text{(A.3.24)}
\end{aligned}$$

$$\begin{aligned}
& \sum_{\sigma\sigma'}\big\{(\sum_{i}\phi_i^*(\vec{r}\sigma)(\vec{\nabla}\tilde{\psi}_j(\vec{r}\sigma'))\times\langle\sigma\big|\vec{\sigma}\big|\sigma\rangle\big\}_\lambda \\
& = \sum_{i\sigma\sigma'}\sum_{\mu\nu}\epsilon_{\lambda\mu\nu}\phi_i^*(\vec{r}\sigma)(\partial_\mu\tilde{\psi}_j(\vec{r}\sigma'))\times\langle\sigma\big|\sigma_\nu\big|\sigma\rangle \\
& = \sum_{\mu\nu}\epsilon_{\lambda\mu\nu}(\frac{1}{2}\partial_\mu\rho_\nu+iJ_{\mu\nu}) \qquad \text{(A.3.25)}
\end{aligned}$$

$$\begin{aligned}
& \sum_{\sigma\sigma'}\big\{(\sum_{i}(\vec{\nabla}\phi_i^*(\vec{r}\sigma))\tilde{\psi}_j(\vec{r}\sigma'))\times\langle\sigma\big|\vec{\sigma}\big|\sigma\rangle\big\}_\lambda \\
& = \sum_{i\sigma\sigma'}\sum_{\mu\nu}\epsilon_{\lambda\mu\nu}(\partial_\mu\phi_i^*(\vec{r}\sigma))\tilde{\psi}_j(\vec{r}\sigma')\times\langle\sigma\big|\sigma_\nu\big|\sigma\rangle \\
& = \sum_{\mu\nu}\epsilon_{\lambda\mu\nu}(\frac{1}{2}\partial_\mu\rho_\nu-iJ_{\mu\nu}) \qquad \text{(A.3.26)}
\end{aligned}$$

$$\begin{aligned}
i\vec{\nabla}\cdot\vec{J}(\vec{r}) &= i\sum_{\lambda\mu\nu}\epsilon_{\lambda\mu\nu}\partial_\lambda J_{\mu\nu} \\
&= \sum_{\lambda\mu\nu}\epsilon_{\lambda\mu\nu}\partial_\lambda\big\{\sum_{i\sigma\sigma'}\phi_i^*(\vec{r}\sigma)(\partial_\mu\tilde{\psi}_i(\vec{r}\sigma))\langle\sigma|\sigma_\nu|\sigma'\rangle-\frac{1}{2}\partial_\mu\rho_\nu(\vec{r})\big\} \\
&= \sum_{i\sigma\sigma'}\sum_{\nu}\big\{\sum_{\lambda\mu}\epsilon_{\lambda\mu\nu}(\partial_\lambda\phi_i^*(\vec{r}\sigma))(\partial_\mu\tilde{\psi}_i(\vec{r}\sigma))\big\}\langle\sigma|\sigma_\nu|\sigma'\rangle \\
&\quad +\sum_{i\sigma\sigma'}\phi_i^*(\vec{r}\sigma)\sum_{\nu}\big\{\sum_{\lambda\mu}\epsilon_{\lambda\mu\nu}(\partial_\lambda\partial_\mu\tilde{\psi}_i(\vec{r}\sigma))\big\}\langle\sigma|\sigma_\nu|\sigma'\rangle-\frac{1}{2}\sum_{\lambda\mu\nu}\epsilon_{\lambda\mu\nu}(\partial_\lambda\partial_\mu\rho_\nu(\vec{r})) \\
&= \sum_{i\sigma\sigma'}\big\{(\vec{\nabla}\phi_i^*(\vec{r}\sigma))\times(\vec{\nabla}\tilde{\psi}_i(\vec{r}\sigma))\big\}\cdot\langle\sigma|\vec{\sigma}|\sigma'\rangle \qquad \text{(A.3.27)}
\end{aligned}$$

$$\tilde{V}_{W_0} = \frac{iW_0}{8}\sum_{ij}\langle\phi_i\phi_j\big|(\vec{\sigma}_1+\vec{\sigma}_2)\cdot(\overleftarrow{\nabla}_1-\overleftarrow{\nabla}_2)\times\delta(\vec{r}_1-\vec{r}_2)(\overrightarrow{\nabla}_1-\overrightarrow{\nabla}_2)(1-\hat{P}_r\hat{P}_\sigma\hat{P}_\tau)\big|\tilde{\psi}_i\tilde{\psi}_j\rangle \qquad \text{(A.3.28)}$$

Only when the resultant spin $S=(\vec{\sigma}_1+\vec{\sigma}_2)$ is 1, the $\tilde{V}_{W_0}$ is non-zero; $\hat{P}_\sigma=1$. Then $\tilde{V}_{W_0}$ can be written as follows

$$\tilde{V}_{W_0} = \tilde{V}_{W_0}^{(1)}+\tilde{V}_{W_0}^{(2)}$$

$$\begin{cases} \tilde{V}^{(1)}_{W_0} = \dfrac{iW_0}{8}\displaystyle\sum_{ij}\langle\phi_i\phi_j\big|(\vec{\sigma}_1+\vec{\sigma}_2)\cdot(\overleftarrow{\nabla}_1-\overleftarrow{\nabla}_2)\times\delta(\vec{r}_1-\vec{r}_2)(\overrightarrow{\nabla}_1-\overrightarrow{\nabla}_2)\big|\tilde{\psi}_i\tilde{\psi}_j\rangle \\ \tilde{V}^{(2)}_{W_0} = -\dfrac{iW_0}{8}\displaystyle\sum_{ij}\langle\phi_i\phi_j\big|(\vec{\sigma}_1+\vec{\sigma}_2)\cdot(\overleftarrow{\nabla}_1-\overleftarrow{\nabla}_2)\times\delta(\vec{r}_1-\vec{r}_2)(\overrightarrow{\nabla}_1-\overrightarrow{\nabla}_2)\hat{P}_r\hat{P}_\tau)\big|\tilde{\psi}_i\tilde{\psi}_j\rangle \end{cases}$$

$$\begin{aligned}
\tilde{V}^{(1)}_{W_0} &= \frac{iW_0}{8}\int d\vec{r}_1 d\vec{r}_2\delta(\vec{r}_1-\vec{r}_2)\sum_{ij}(\langle\sigma_1\big|\vec{\sigma}\big|\sigma_2\rangle+\langle\sigma'_1\big|\vec{\sigma}\big|\sigma'_2\rangle) \\
&\quad\cdot\Big[\big\{(\vec{\nabla}\phi^*_i(\vec{r}_1\sigma_1)\phi^*_j(\vec{r}_2\sigma_2)-\phi^*_i(\vec{r}_1\vec{\sigma}_2)(\vec{\nabla}\phi^*_j(\vec{r}_2\sigma_2))\big\} \\
&\quad\times\big\{(\vec{\nabla}\tilde{\psi}^*_i(\vec{r}_1\sigma_1)\tilde{\psi}^*_j(\vec{r}_2\sigma_2)-\tilde{\psi}^*_i(\vec{r}_1\vec{\sigma}_2)(\vec{\nabla}\tilde{\psi}^*_j(\vec{r}_2\sigma_2))\big\}\Big] \\
&= \frac{iW_0}{8}\int d\vec{r}\Big[\sum_{i\sigma_1\sigma'_1}(\vec{\nabla}\phi^*_i(\vec{r}\vec{\sigma}_1))\times(\vec{\nabla}\tilde{\psi}_i(\vec{r}\sigma'_1))\cdot\langle\sigma_1\big|\vec{\sigma}\big|\sigma'_1\rangle\sum_{j\sigma_2\sigma'_2}\phi^*_j(\vec{r}\sigma_2)\tilde{\psi}_j(\vec{r}\sigma'_2) \\
&\quad+\sum_{i\sigma_1\sigma'_1}\phi^*_i(\vec{r}\vec{\sigma}_1)\tilde{\psi}_i(\vec{r}\sigma'_1)\sum_{j\sigma_2\sigma'_2}(\vec{\nabla}\phi^*_j(\vec{r}\sigma_2))\times(\vec{\nabla}\tilde{\psi}_j(\vec{r}\sigma'_2))\cdot\langle\sigma_2\big|\vec{\sigma}\big|\sigma'_2\rangle \\
&\quad+\sum_{i\sigma_1\sigma'_1}(\vec{\nabla}\phi^*_i(\vec{r}\vec{\sigma}_1))\times(\vec{\nabla}\tilde{\psi}_i(\vec{r}\sigma'_1))\cdot\sum_{j\sigma_2\sigma'_2}\phi^*_j(\vec{r}\sigma_2)\tilde{\psi}_j(\vec{r}\sigma'_2)\langle\sigma_2\big|\vec{\sigma}\big|\sigma'_2\rangle \\
&\quad+\sum_{i\sigma_1\sigma'_1}\phi^*_i(\vec{r}\vec{\sigma}_1)\tilde{\psi}_i(\vec{r}\sigma'_1)\langle\sigma_2\big|\vec{\sigma}\big|\sigma'_2\rangle\cdot\sum_{j\sigma_2\sigma'_2}(\vec{\nabla}\phi^*_j(\vec{r}\sigma_2))\times(\vec{\nabla}\tilde{\psi}_j(\vec{r}\sigma'_2)) \\
&\quad+\sum_{i\sigma_1\sigma'_1}\phi^*_i(\vec{r}\vec{\sigma}_1)(\vec{\nabla}\tilde{\psi}_i(\vec{r}\sigma'_1))\cdot\sum_{j\sigma_2\sigma'_2}(\vec{\nabla}\phi^*_j(\vec{r}\sigma_2))\tilde{\psi}_j(\vec{r}\sigma'_2)\times\langle\sigma_2\big|\vec{\sigma}\big|\sigma'_2\rangle \\
&\quad+\sum_{i\sigma_1\sigma'_1}(\vec{\nabla}\phi^*_i(\vec{r}\vec{\sigma}_1))\tilde{\psi}_i(\vec{r}\sigma'_1)\times\langle\sigma_1\big|\vec{\sigma}\big|\sigma'_1\rangle\cdot\sum_{j\sigma_2\sigma'_2}\phi^*_j(\vec{r}\sigma_2)(\vec{\nabla}\tilde{\psi}_j(\vec{r}\sigma'_2)) \\
&\quad-\sum_{i\sigma_1\sigma'_1}(\vec{\nabla}\phi^*_i(\vec{r}\vec{\sigma}_1))\tilde{\psi}_i(\vec{r}\sigma'_1)\cdot\sum_{j\sigma_2\sigma'_2}\phi^*_j(\vec{r}\sigma_2)(\vec{\nabla}\tilde{\psi}_j(\vec{r}\sigma'_2))\times\langle\sigma_2\big|\vec{\sigma}\big|\sigma'_2\rangle \\
&\quad-\sum_{i\sigma_1\sigma'_1}\phi^*_i(\vec{r}\vec{\sigma}_1)(\vec{\nabla}\tilde{\psi}_i(\vec{r}\sigma'_1))\times\langle\sigma_1\big|\vec{\sigma}\big|\sigma'_1\rangle\cdot\sum_{j\sigma_2\sigma'_2}(\vec{\nabla}\phi^*_j(\vec{r}\sigma_2))\tilde{\psi}_j(\vec{r}\sigma'_2)\Big] \\
&= \frac{iW_0}{4}\int d\vec{r}\Big[i(\vec{\nabla}\times\vec{j}(\vec{r}))\cdot\vec{\rho}(\vec{r})+i\rho(\vec{r})\vec{\nabla}\cdot\vec{J}(\vec{r}) \\
&\quad+\sum_{\lambda\mu\nu}(\frac{1}{2}\vec{\nabla}\rho(\vec{r})+i\vec{j}(\vec{r}))_\lambda\epsilon_{\lambda\mu\nu}(\frac{1}{2}\partial_\mu\rho_\nu-iJ_{\mu\nu}) \\
&\quad-\sum_{\lambda\mu\nu}(\frac{1}{2}\vec{\nabla}\rho(\vec{r})-i\vec{j}(\vec{r}))_\lambda\epsilon_{\lambda\mu\nu}(\frac{1}{2}\partial_\mu\rho_\nu+iJ_{\mu\nu})\Big] \\
&= -\frac{W_0}{4}\int d\vec{r}\Big[(\vec{\nabla}\times\vec{j}(\vec{r}))\cdot\vec{\rho}(\vec{r})+\rho(\vec{r})\vec{\nabla}\cdot\vec{J}(\vec{r})+\sum_{\lambda\mu\nu}\epsilon_{\lambda\mu\nu}\big\{\vec{j}(\vec{r})_\lambda\partial_\mu\rho_\nu-(\partial_\lambda\rho(\vec{r}))J_{\mu\nu})\Big] \\
&= -\frac{W_0}{2}\int d\vec{r}\Big[(\vec{\nabla}\times\vec{j}(\vec{r}))\cdot\vec{\rho}(\vec{r})+\rho(\vec{r})\vec{\nabla}\cdot\vec{J}(\vec{r})\Big] \qquad (A.3.29)
\end{aligned}$$

Finally we can write W_0 term as

$$\begin{aligned}
\tilde{V}^{(2)}_{W_0} &= \frac{iW_0}{8}\int d\vec{r}_1 d\vec{r}_2 \delta(\vec{r}_1-\vec{r}_2)\sum_{\tau}\sum_{ij\in\tau}(\langle\sigma_1|\vec{\sigma}|\sigma_2\rangle+\langle\sigma'_1|\vec{\sigma}|\sigma'_2\rangle) \\
&\quad \cdot\Big[\big\{(\vec{\nabla}\phi^*_i(\vec{r}_1\sigma_1)\phi^*_j(\vec{r}_2\sigma_2)-\phi^*_i(\vec{r}_1\vec{\sigma}_2)(\vec{\nabla}\phi^*_j(\vec{r}_2\sigma_2))\big\} \\
&\quad \times\big\{\tilde{\psi}_i(\vec{r}_2\vec{\sigma}_2)(\vec{\nabla}\tilde{\psi}_j(\vec{r}_1\sigma_2))-(\vec{\nabla}\tilde{\psi}_i(\vec{r}_2\sigma_1))\tilde{\psi}_j(\vec{r}_1\sigma_2)\big\}\Big] \\
&= -\frac{iW_0}{8}\int d\vec{r}\sum_{\tau}\sum_{ij\in\tau}(\langle\sigma_1|\vec{\sigma}|\sigma_2\rangle+\langle\sigma'_1|\vec{\sigma}|\sigma'_2\rangle) \\
&\quad \cdot\Big[\big\{(\vec{\nabla}\phi^*_i(\vec{r}\sigma_1)\phi^*_j(\vec{r}\sigma_2)-\phi^*_i(\vec{r}\vec{\sigma}_2)(\vec{\nabla}\phi^*_j(\vec{r}\sigma_2))\big\} \\
&\quad \times\big\{(\vec{\nabla}\tilde{\psi}_i(\vec{r}\sigma_1))\tilde{\psi}_j(\vec{r}\sigma_2)-\tilde{\psi}_i(\vec{r}\vec{\sigma}_2)(\vec{\nabla}\tilde{\psi}_j(\vec{r}\sigma_2))\big\}\Big] \\
&= \frac{W_0}{2}\sum_{\tau}\int d\vec{r}\Big[(\vec{\nabla}\times\vec{j}^{(\tau)}(\vec{r}))\cdot\vec{\rho}^{(\tau)}(\vec{r})+\rho^{(\tau)}(\vec{r})\vec{\nabla}\cdot\vec{J}^{(\tau)}(\vec{r})\Big]. \qquad \text{(A.3.30)}
\end{aligned}$$

Appendix B

Numerical methods

B.1 Finite lattice method and Fourier transform method for Gogny interaction

We examine a convergence of calculated matrix element of Gogny Hamiltonian $\hat{H}_{Gogny}$ with respect to the radius R_f which was mentioned in Sec. 2.5.2. We calculate the matrix element $\langle\Psi|\,\hat{H}_{Gogny}\,|\Psi\rangle$ by changing R_f. We chose $|\Psi\rangle$ as Skyrme HF state with SLy4 parameter and employ D1S parameter for Gogny interaction.

In Fig. B.1, the vertical axis shows the calculated value of the expectation value, while the horizontal axis shows the radius R_f. The calculated value by using all mesh points is shown as dots line at -130.5 MeV. The value of the expectation value $\langle\Psi|\,\hat{H}_{Gogny}\,|\Psi\rangle$ gradually approaches to 130.5 MeV as R_f gets larger. Once R_f is larger than about 3 fm, the value is almost equal to -130.5 MeV. We thus conclude that the value of the expectation value of Gogny Hamiltonian is converged, if R_f is more than about 3 fm. We next discuss computational costs to calculate the expectation value of Gogny Hamiltonian.

Before showing the result, we estimate computational costs for "Finite spherical lattice" and "Fourier transform". First, we estimate the computational cost for "Finite spherical lattice". The computational cost to calculate the integration in Eq. (2.5.6) is proportion to the product of N_{box} and N_{sphere}, where the N_{box} is the number of mesh points for $\vec{r}$ and the N_{sphere} is the number of mesh points $\vec{r}'$. On the other hand, the computational cost to calculate the densities of Eq. (2.5.7) is proportional to $N_{box} \times N_{sphere}$ and to the nucleon number, A. Because the calculations of the densities need to be performed A times, it is the main part of the numerical calculation. The computational costs to calculate the matrix element by "Finite spherical lattice" is proportion to about $N_{box} \times N_{sphere} \times A$. Next, we estimate the computational cost for "Fourier transform". Since the computational cost is proportion to the number of times to perform Fourier transform, the computational cost for "Fourier transform" is proportion to A^2. Finally we estimate the computational cost of "Skyrme" for comparison. The energy functional is composed of several densities having $\vec{r}$ as variable. Integration of the density over space yields the number of nucleons. Because the calculation of densities is the main part of the numerical calculation, the computational cost of "Skyrme" is proportion to $N_{box} \times A$. Typical, N_{box} is about 4,000 and N_{sphere} is about

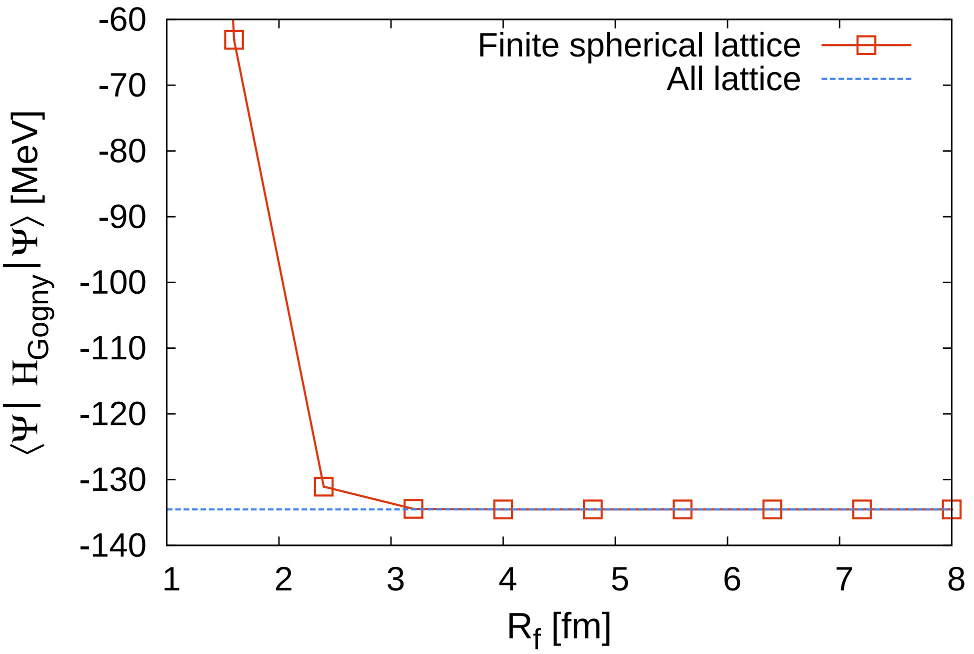

Figure B.1: Calculated expectation value of Gogny Hamiltonian for ^{16}O as a function of R_f. The horizontal line is the calculated value using all mesh points.

500 for $R_f = 3.2$ fm.

We show CPU time for numerical methods of matrix element of Gogny and Skyrme Hamiltonians by changing nucleon number in Fig. B.2. The horizontal axis shows the number of nucleon A. The CPU times are normalized to the CPU time to calculate matrix elements of Skyrme Hamiltonian. Namely, CPU time for ”Skyrme” is 1 for all number of nucleons in the Figure. In the Fig. B.2, the normalized CPU time for ”Finite spherical lattice” is about 15 and does not change by varying the number of nucleon A. This result indicates that calculation of matrix element for Gogny Hamiltonian by ”Finite spherical lattice” takes 15 times longer than that of ”Skyrme” for all nuclei. These results are consistent with the estimation in the previous paragraph: The CPU time for ”Finite spherical lattice” is proportion to about $N_{box} \times N_{sphere} \times A$, while the CPU time for ”Skyrme” is proportion to about $N_{box} \times A$. The normalized CPU time by the CPU time of ”Skyrme” is constant to change of A.

In the Fig. B.2, the normalized CPU time for ”Fourier transform” scales linearly with the number of nucleon. This result is consistent with the estimation: The normalized CPU time is proportionate A, since the CPU time for ”Fourier transform” is proportion to the squared A. As seen from the Fig. B.2, the normalized CPU time for ”Fourier transform” is larger than that for ”Finite spherical lattice” for all nucleon ($A < 12$). We conclude that ”Finite spherical lattice” is more effective than ”Fourier transform” at least $A = 12$ or more nucleus.

Finally we discuss numerical cost for ”All lattice”, which is almost the same method as

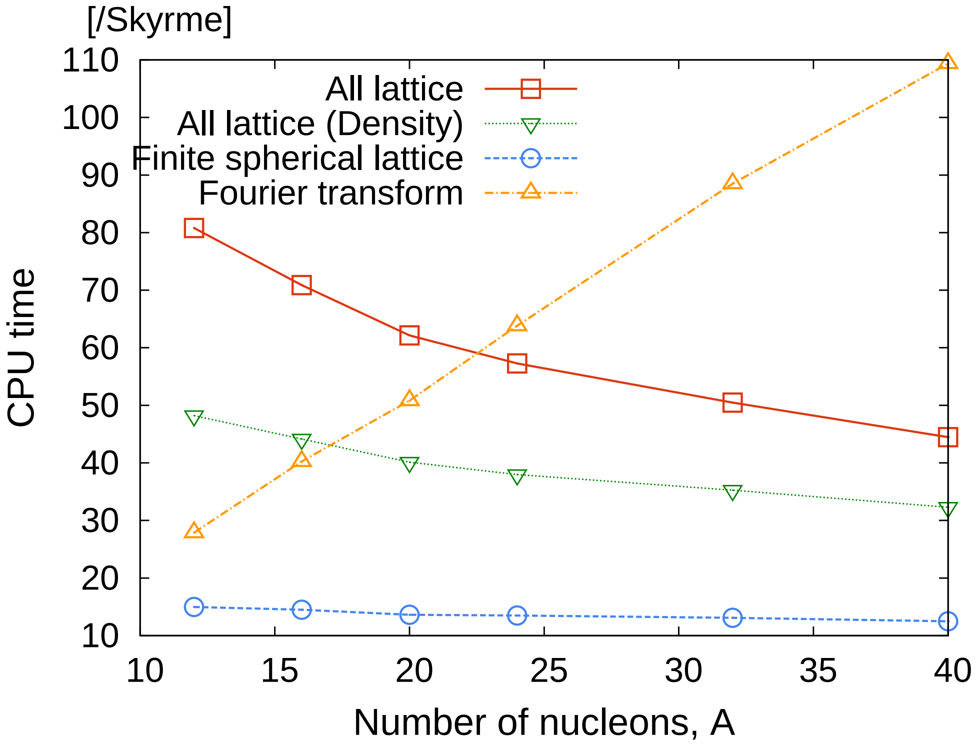

Figure B.2: CPU times for matrix element V_F which is normalized by CPU time for matrix element of Skyrme force. The "All lattice" is CPU time employed all mesh points. The "All lattice (Density)" is CPU time for calculation of density of "All lattice". The "Finite spherical lattice" and "Fourier transform" is CPU time by methods of Finite spherical lattice and Fourier transform, respectively. In the Finite spherical lattice, we chose $R_f = 3.2$ fm.

"Finite spherical method" while the all mesh points of $\vec{r}'$ are employed. We expect that the numerical cost is proportion to the squared N_{sphere} and proportion to the number of nucleon A. From the simple estimation, the numerical cost for "All lattice" is $N_{sphere}/N_{box} \approx 8$ times more expensive than that for "Finite spherical lattice". However, since the mesh points of $\vec{r}$ for "Finite spherical lattice" dose not suite for numerical calculation, it became smaller than 8 times. In the Fig. B.2, the normalized CPU time for "All lattice" is about 15 times larger than that for "Finite spherical lattice" at $A = 12$ and is gradually decreased as the number of nucleon increased. Examining the details, the numerical cost to calculate integration in Eq. (2.5.6) is expected to be constant with A. The normalized CPU time of this integration is decreased linearly [Fig. B.2 All lattice (Integration)]. The numerical cost to calculate densities in Eq. (2.5.7) is decreased as A increased [Fig. B.2 All lattice (Densities)], although we expect that the cost for the densities is proportion to A. This may be because the optimization of numerical calculation become easier as the size of array ρ become larger.

B.2 Center of mass correction

We assume that N-body wave function can be written as product of wave functions of center of mass $\phi(\vec{R}_G)$ and internal coordinate $\Phi_{int}(\vec{r}_1, \cdots, \vec{r}_N)$:

$$\Phi(\vec{r}_1, \cdots \vec{r}_N) = \phi(\vec{R}_G)\Phi_{int}(\vec{r}_1, \cdots, \vec{r}_N), \tag{B.2.1}$$

where $\vec{R}_G$ is position vector of center-of-mass. The internal wave function satisfies the following equation:

$$\Phi_{int}(\vec{r}_1 - \vec{a}, \cdots, \vec{r}_N - \vec{a}) = \Phi_{int}(\vec{r}_1, \cdots, \vec{r}_N), \tag{B.2.2}$$

where $\vec{a}$ is arbitrary vector. The wave function of internal coordinate in Jacobi coordinate $\{\vec{\xi}_1, \cdots, \vec{\xi}_{N-1}\}$ is written as

$$\Phi_{int}(\vec{r}_1, \cdots, \vec{r}_N) = \Phi'_{int}(\vec{\xi}_1, \cdots, \vec{\xi}_{N-1}). \tag{B.2.3}$$

We assume that the center-of-mass and internal wave-function is normalized, respectively:

$$\begin{aligned} \int d\vec{R}_G |\phi_G(\vec{R}_G)|^2 &= 1 & \text{(B.2.4)} \\ \int d\vec{\xi}_1 \cdots d\vec{\xi}_{N-1} |\Phi'_{int}(\vec{\xi}_1, \cdots, \vec{\xi}_{N-1})|^2 &= 1. & \text{(B.2.5)} \end{aligned}$$

The rms radius corrected for center-of-mass is given by

$$\begin{aligned} \langle r^2 \rangle_{int} &= \int d\xi_1 \cdots \xi_{N-1} |\Phi'_{int}(\vec{\xi}_1, \cdots, \vec{\xi}_{N-1})|^2 \frac{1}{N} \sum_{i=1}^{N} (\vec{r}_i - \vec{R}_G)^2 \\ &= \int \vec{R}_G |\phi_G(\vec{R}_G)|^2 \int d\vec{\xi}_1 \cdots \vec{\xi}_{N-1} |\Phi'_{int}(\vec{\xi}_1, \cdots, \vec{\xi}_{N-1})|^2 \sum_{i=1}^{N} \frac{1}{N} (\vec{r}_i - \vec{R}_G)^2 \\ &= \int d\vec{r}_1 \cdots \vec{r}_N |\Phi(\vec{r}_1, \cdots, \vec{r}_N)|^2 \sum_{i=1}^{N} \frac{1}{N} (\vec{r}_i - \vec{R}_G)^2 \\ &= \int d\vec{r}_1 \cdots \vec{r}_N |\Phi(\vec{r}_1, \cdots, \vec{r}_N)|^2 \left(\sum_{i=1}^{N} \frac{1}{N} \vec{r}_i^2 - \vec{R}_G^2 \right) \\ &= \langle r^2 \rangle - \int d\vec{R}_G \vec{R}_G^2 |\phi_G(\vec{R}_G)|^2, & \text{(B.2.6)} \end{aligned}$$

where

$$\langle r^2 \rangle = \int d\vec{r}_1 \cdots \vec{r}_N |\Phi(\vec{r}_1, \cdots, \vec{r}_N)|^2 \frac{1}{N} \sum_{i=1}^{N} \vec{r}_i^2. \tag{B.2.7}$$

$\langle r^2 \rangle$ is radius before correction of center-of-mass effect, and can be calculated by present calculation numerically. We evaluate second term in Eq. (B.2.6) by using harmonic-oscillator shell-model:

$$\int d\vec{R}_G \vec{R}_G^2 |\phi_G(\vec{R}_G)|^2 = \frac{3}{4N\nu}. \tag{B.2.8}$$

Here, we use the wave function of center-of-mass by harmonic-oscillator shell-model:

$$\phi_G(\vec{R}_G) = \left(\frac{2N\nu}{\pi}\right)^{\frac{3}{4}} \exp[-N\nu\vec{R}_G^2], \tag{B.2.9}$$

where we used shell-model single-particle wave functions:

$$\phi_i(\vec{r}) = p_i(\vec{r})e^{-\nu r^2} \quad (p_i(\vec{r}) : \text{polynomial of } \vec{r}). \tag{B.2.10}$$

We use the width parameter of harmonic-oscillator $1/(2\nu) = \hbar/(m\omega) = 0.90A^{1/3} + 0.07\text{fm}^2$ in Ref. [114]. We note that the evaluation of center-of-mass correction in this section is accurate only for the ground state. However, we use this evaluation for excited states.

B.3 Lagrange mesh

In Eqs. (2.3.6), (2.3.7), (2.3.9), and (2.3.10), we operate on $\hat{j}_y$ and $\hat{j}_z$ many times. In order to perform these operations of $\hat{j}_y$ and $\hat{j}_z$ as exactly as possible, we use Lagrange mesh method for first derivative contained in the operators $\hat{j}_y$ and $\hat{j}_z$. In this section, we show the Lagrange mesh method for a first derivative of a function $\psi(x)$.

We expand the function $\psi(x)$ as basis function ϕ_k $(k = 1, \cdots, N_p)$:

$$\psi(x) = \sum_{i=1}^{N_p} \lambda_i^{1/2}\psi(x_i)f_i(x), \tag{B.3.1}$$

where

$$\lambda_i = \left[\sum_{k=1}^{N_p} |\phi_k(x_i)|^2\right]^{-1} \tag{B.3.2}$$

$$f_i(x) = \lambda_i^{1/2}\sum_{k=1}^{N_p} \phi_k^*(x_i)\phi_k(x). \tag{B.3.3}$$

If $\phi_k(x_i)$ is first sin basis

$$\phi_k(x_i) = \sqrt{2}\sin\left[\pi k\frac{x_i}{N_p}\right] \quad (k = 1, \cdots, N_p), \tag{B.3.4}$$

where $x_i = i$ $(i = 0, \cdots, N_p)$,

$$\lambda_i^{-1} = N_p - \frac{\cos[(N-1)\pi x_i]\sin[N\pi x_i]}{2\sin[x_i]} = N_p \tag{B.3.5}$$

$$f_i(x) = 2N_p^{-1/2}\sum_{k=1}^{N_p} \sin\left[\frac{\pi}{N_p}kx\right]\sin\left[\frac{\pi}{N_p}kx_i\right]. \tag{B.3.6}$$

Finally, we get the derivative of the function $\psi(x)$

$$\psi'(x) = \sum_{i=1}^{N_p} \lambda_i^{1/2}\psi(x_i) f_i'(x), \tag{B.3.7}$$

where

$$f_i'(x) = 2N_p^{-1/2}\frac{\pi}{N_p}\sum_{k=1}^{N_p} k\cos\left[\frac{\pi}{N_p}kx\right]\sin\left[\frac{\pi}{N_p}kx_i\right]. \tag{B.3.8}$$

B.4 Matrix elements of tensor operator

To calculate transition strengths, we need to estimate matrix elements of tensor operator. The matrix elements of the given tensor operator $\hat{T}_{\lambda\mu}$ (rank k) between two angular momentum projected states are calculated as follows:

$$\begin{aligned}
&\frac{8\pi^2}{2J_2+1}\frac{8\pi^2}{2J_1+1}\big\langle P^{J_2}_{M_2K_2}\Phi_2\big|\hat{T}_{\lambda\mu}\big|\hat{P}^{J_1}_{M_1K_1}\Phi_1\big\rangle \\
&= \iint d\Omega_2 d\Omega_1 D^{J_2*}_{M_2K_2}(\Omega_2) D^{J_1}_{M_1K_1}(\Omega_1)\big\langle\Phi_2\big|\hat{R}^\dagger(\Omega_2)\hat{Q}_{2\mu}\hat{R}(\Omega_1)\big|\Phi_1\big\rangle \\
&= \iint d\Omega_2 d\Omega_1 D^{J_2*}_{M_2K_2}(\Omega_2) D^{J_1}_{M_1K_1}(\Omega_1)\big\langle\Phi_2\big|\{\hat{R}^\dagger(\Omega_2)\hat{T}_{\lambda\mu}\hat{R}(\Omega_2)\}\hat{R}^\dagger(\Omega_2)\hat{R}(\Omega_1)\big|\Phi_1\big\rangle \\
&= \iint d\Omega_2 d\Omega_1 D^{J_2*}_{M_2K_2}(\Omega_2) D^{J_1}_{M_1K_1}(\Omega_1)\big\langle\Phi_2\big|\sum_{\delta=-\lambda}^{\lambda} D^{\lambda}_{\mu\delta}(\Omega_2)\hat{T}_{\lambda\delta}\hat{R}^\dagger(\Omega_2)\hat{R}(\Omega_1)\big|\Phi_1\big\rangle \\
&= \iint d\Omega_2 d\Omega D^{J_2*}_{M_2K_2}(\Omega_2)\sum_{K=-J_1}^{J_1} D^{J_1}_{M_1K}(\Omega_2) D^{J_1}_{KK_1}(\Omega)\big\langle\Phi_2\big|\sum_{\delta=-\lambda}^{\lambda} D^{\lambda}_{\mu\delta}(\Omega_2)\hat{T}_{\lambda\delta}\hat{R}(\Omega)\big|\Phi_1\big\rangle \\
&= \frac{8\pi^2}{2J_2+1}\big\langle J_1\lambda M_1\mu\big|J_2M_2\big\rangle\sum_{K=-J_1}^{J_1}\sum_{\delta=-\lambda}^{\lambda}\big\langle J_1\lambda K\delta\big|J_2K_2\big\rangle\int d\Omega D^{J_1}_{KK_1}(\Omega)\big\langle\Phi_2\big|\hat{T}_{\lambda\delta}\hat{R}(\Omega)\big|\Phi_1\big\rangle \\
&= \frac{8\pi^2}{2J_2+1}\big\langle J_1\lambda M_1\mu\big|J_2M_2\big\rangle\sum_{K=-J_1}^{J_1}\sum_{\delta=-\lambda}^{\lambda}\big\langle J_1\lambda K\delta\big|J_2K_2\big\rangle \\
&\quad\times\int d\Omega e^{i\alpha\delta} D^{J_1}_{KK_1}(\Omega)\big\langle\Phi_2\big|e^{-i\alpha\hat{J}_z}\hat{T}_{\lambda\delta}e^{-i\beta\hat{J}_y}e^{-i\gamma\hat{J}_z}\big|\Phi_1\big\rangle
\end{aligned}$$

Using Wigner-Eckart theorem

$$\big\langle P^{J_2}_{M_2K_2}\Phi_2\big|\hat{T}_{\lambda\mu}\big|\hat{P}^{J_1}_{M_1K_1}\Phi_1\big\rangle = (2J_2+1)^{-1/2}\big\langle J_1\lambda M_1\mu\big|J_2M_2\big\rangle\big\langle J_2\big\|\hat{T}_\lambda\big\|J_1\big\rangle, \tag{B.4.1}$$

we can calculate $B(E\lambda)$ as

$$
\begin{aligned}
B(E\lambda; J_i \to J_f) &\equiv \frac{1}{2J_i+1}\left|\left\langle J_f \middle\| \hat{T}_\lambda \middle\| J_i \right\rangle\right|^2 \\
&= \left(\frac{2J_f+1}{8\pi^2}\right)\left(\frac{2J_i+1}{8\pi^2}\right)\Bigg| \sum_{K=-J_1}^{J_1} \sum_{\delta=-\lambda}^{\lambda} \left\langle J_1 \lambda K \delta \middle| J_2 K_2 \right\rangle \qquad \text{(B.4.2)} \\
&\quad \int d\Omega e^{i\alpha\delta} D^{J_1}_{KK_1}(\Omega) \left\langle \Phi_2 \middle| e^{-i\alpha \hat{J}_z} \hat{T}_{\lambda\delta} e^{-i\beta \hat{J}_y} e^{-i\gamma \hat{J}_z} \middle| \Phi_1 \right\rangle \Bigg| . \qquad \text{(B.4.3)}
\end{aligned}
$$

This equation is only true if $\left\langle J_1 \lambda M_1 \mu \middle| J_2 M_2 \right\rangle \neq 0$.

B.5 Single-particle Hamiltonian

The single-particle Hamiltonian h_{HF} is defined as

$$
\hat{h}^{(\tau)}_{HF}(\vec{r}) = -\frac{\hbar^2}{2m}\nabla^2 + \hat{h}^{(\tau)}_e(\vec{r}) + \hat{h}^{(\tau)}_o(\vec{r}), \tag{B.5.1}
$$

where

$$
\begin{cases}
\hat{h}^{(\tau)}_e = -\vec{\nabla} \cdot M^{(\tau)}(\vec{r})\vec{\nabla} + U^{(\tau)}(\vec{r}) + \dfrac{1}{2i}\left(\overleftrightarrow{\nabla\sigma} \cdot \overleftrightarrow{B}^{(\tau)}(\vec{r}) + \overleftrightarrow{B}^{(\tau)}(\vec{r}) \cdot \overleftrightarrow{\nabla\sigma}\right) & \text{(B.5.2)} \\
\hat{h}^{(\tau)}_o = -\vec{\nabla} \cdot \left(\vec{\sigma} \cdot \vec{C}^{(\tau)}(\vec{r})\right) \nabla + \vec{\sigma} \cdot \vec{V}^{(\tau)}(\vec{r}) + \dfrac{1}{2i}\left(\vec{\nabla} \cdot \vec{I}^{(\tau)}(\vec{r}) + \vec{I}^{(\tau)} \cdot \vec{\nabla}\right). & \text{(B.5.3)}
\end{cases}
$$

Here, $M^{(\tau)}$, $U^{(\tau)}$, $\overleftrightarrow{B}^{(\tau)}$, $\vec{I}^{(\tau)}$, $\vec{C}^{(\tau)}$, and $\vec{V}^{(\tau)}$ are defined as

$$
\begin{aligned}
M^{(\tau)}(\vec{r}) &= B_3\rho(\vec{r}) + B_4\rho^{(\tau)}(\vec{r}) && \text{(B.5.4a)} \\
U^{(\tau)}(\vec{r}) &= 2B_1\rho(\vec{r}) + 2B_2\rho^{(\tau)}(\vec{r}) + B_3\tau(\vec{r}) + B_4\tau^{(\tau)}(\vec{r}) \\
&\quad + 2B_5\nabla^2\rho(\vec{r}) + 2B_6\nabla^2\rho^{(\tau)}(\vec{r}) \\
&\quad + B_7(\alpha+2)\rho(\vec{r})^{\alpha+1} + B_8\left[\alpha\rho(\vec{r})^{\alpha-1}\sum_{\tau'}\rho^{(\tau')}(\vec{r})^2 + 2\rho(\vec{r})^{\alpha-1}\vec{\rho}(\vec{r})\right] \\
&\quad + B_9\left(\overleftrightarrow{\nabla} \cdot \overleftrightarrow{J}(\vec{r}) + \overleftrightarrow{\nabla} \cdot \overleftrightarrow{J}^{(\tau)}(\vec{r})\right) \\
&\quad + B_{12}\alpha\rho(\vec{r})^{\alpha-1}\vec{\rho}(\vec{r})^2 + B_{13}\alpha\rho(\vec{r})^{\alpha-1}\sum_{\tau}\vec{\rho}^{(\tau)}(\vec{r})^2 \\
&\quad + e^2\left[\int d\vec{r}'\frac{\rho(\vec{r}')}{|\vec{r}-\vec{r}'|} - \left(\frac{3}{\pi}\right)^{1/3}\rho_p(\vec{r})^{1/3}\right]\delta_{\tau',p} && \text{(B.5.4b)} \\
\overleftrightarrow{B}^{(\tau)}(\vec{r}) &= -2B_{14}\overleftrightarrow{J}(\vec{r}) - 2B_{16}\overleftrightarrow{J}^{(\tau)}(\vec{r}) - B_9\left(\overleftrightarrow{\nabla}\rho(\vec{r}) + \overleftrightarrow{\nabla}\rho^{(\tau)}(\vec{r})\right) && \text{(B.5.4c)} \\
\vec{I}^{(\tau)}(\vec{r}) &= -2B_3\vec{j}(\vec{r}) - 2B_4\vec{j}^{(\tau)}(\vec{r}) - B_9\left(\overleftrightarrow{\nabla}\rho(\vec{r}) + \overleftrightarrow{\nabla}\rho^{(\tau)}(\vec{r})\right) && \text{(B.5.4d)} \\
\vec{C}^{(\tau)} &= B_{14}\vec{\rho}(\vec{r}) + B_{16}\rho^{(\tau)}(\vec{r}) && \text{(B.5.4e)}
\end{aligned}
$$

$$\begin{aligned}\vec{V}^{(\tau)} = B_9\left(\vec{\nabla}\times\vec{j}(\vec{r}) + \vec{\nabla}\times\vec{j}^{(\tau)}(\vec{r})\right) + 2B_{10}\vec{\rho}(\vec{r}) + 2B_{11}\vec{\rho}^{(\tau)}(\vec{r}) \\ + 2B_{12}\rho(\vec{r})^{\alpha}\vec{\rho}(\vec{r}) + 2B_{13}\rho(\vec{r})^{\alpha}\vec{\rho}^{(\tau)}(\vec{r}) + 2B_{15}\nabla^2\vec{\rho}(\vec{r}) + 2B_{17}\nabla^2\vec{\rho}^{(\tau)}(\vec{r})\end{aligned} \tag{B.5.4f}$$

In the following, we show formulae to calculate single-particle Hamiltonian of Skyrme interaction for each term.

Kinetic term

$$\frac{\delta}{\delta\phi_i^*(\vec{r}',\sigma')}\int d\vec{r}\,\tau(\vec{r}) \;=\; \nabla^2\phi(\vec{r}',\sigma') \tag{B.5.5}$$

B_1 term

$$\begin{aligned}\frac{\delta}{\delta\phi_i^*(\vec{r}',\sigma')}\int d\vec{r}\,\rho(\vec{r})^2 &= 2\int d\vec{r}\,\rho(\vec{r})\frac{\delta\rho(\vec{r})}{\delta\phi_i^*(\vec{r}'\sigma')} \\ &= 2\rho(\vec{r}')\phi_i(\vec{r}'\sigma')\end{aligned} \tag{B.5.6}$$

B_2 term

$$\begin{aligned}\frac{\delta}{\delta\phi_{i\in\tau'}^*(\vec{r}',\sigma')}\int d\vec{r}\sum_{\tau}\rho^{(\tau)}(\vec{r})^2 &= 2\int d\vec{r}\,\rho^{(\tau')}(\vec{r})\frac{\delta\rho^{(\tau')}(\vec{r})}{\delta\phi_i^*(\vec{r}'\sigma')} \\ &= 2\rho^{(\tau')}(\vec{r}')\phi_i(\vec{r}'\sigma')\end{aligned} \tag{B.5.7}$$

B_3 term

$$\begin{aligned}&\frac{\delta}{\delta\phi_i^*(\vec{r}',\sigma')}\int d\vec{r}\left[\tau(\vec{r})\rho(\vec{r}) - \vec{j}^2\right] \\ &= \left[-\rho(\vec{r}')\nabla^2 - \left(\vec{\nabla}\rho(\vec{r}')\right)\cdot\vec{\nabla} + \tau(\vec{r}') + 2i\vec{j}(\vec{r}')\cdot\vec{\nabla} + i\left(\vec{\nabla}\cdot\vec{j}(\vec{r}')\right)\right]\phi_i(\vec{r}'\sigma')\end{aligned} \tag{B.5.8}$$

B_4 term

$$\begin{aligned}&\frac{\delta}{\delta\phi_{i\in\tau'}^*(\vec{r}',\sigma')}\int d\vec{r}\sum_{\tau}\left[\tau^{(\tau)}(\vec{r})\rho^{(\tau)}(\vec{r}) - \left(\vec{j}^{(\tau)}(\vec{r})\right)^2\right] \\ &= \left[-\rho^{(\tau')}(\vec{r}')\nabla^2 - \left(\vec{\nabla}\rho^{(\tau')}(\vec{r}')\right)\cdot\vec{\nabla} + \tau^{(\tau')}(\vec{r}') + 2i\vec{j}^{(\tau')}(\vec{r}')\cdot\vec{\nabla} + i\left(\vec{\nabla}\cdot\vec{j}^{(\tau')}(\vec{r}')\right)\right]\phi_i(\vec{r}'\sigma')\end{aligned} \tag{B.5.9}$$

B_5 term

$$\frac{\delta}{\delta\phi_i^*(\vec{r}',\sigma')}\int d\vec{r}\rho(\vec{r})\nabla^2\rho(\vec{r}) = 2(\nabla^2\rho(\vec{r}'))\phi_i(\vec{r}'\sigma') \tag{B.5.10}$$

B_6 term

$$\frac{\delta}{\delta\phi_{i\in\tau'}^*(\vec{r}',\sigma')}\int d\vec{r}\sum_{\tau}\rho^{(\tau)}(\vec{r})\nabla^2\rho^{(\tau)}(\vec{r}) = 2(\nabla^2\rho^{(\tau')}(\vec{r}'))\phi_i(\vec{r}'\sigma') \tag{B.5.11}$$

B_7 term

$$\frac{\delta}{\delta\phi_i^*(\vec{r}',\sigma')}\int d\vec{r}\rho(\vec{r})^{\alpha}\rho(\vec{r})^2 = (\alpha+2)\rho(\vec{r}')^{\alpha+1}\phi_i(\vec{r}'\sigma') \tag{B.5.12}$$

B_8 term

$$\frac{\delta}{\delta\phi_{i\in\tau'}^*(\vec{r}',\sigma')}\int d\vec{r}\rho^{(\tau)}(\vec{r})^{\alpha}\rho^{(\tau)}(\vec{r})^2 = (\alpha+2)\rho^{(\tau')}(\vec{r}')^{\alpha+1}\phi_i(\vec{r}'\sigma') \tag{B.5.13}$$

B_9 term

$$\frac{\delta}{\delta\phi_i^*(\vec{r}',\sigma')}\int d\vec{r}\rho(\vec{r})\vec{\nabla}\cdot\vec{J}(\vec{r}) = \left(\vec{\nabla}\cdot\vec{J}(\vec{r}')\right)\phi_i(\vec{r}'\sigma') + \int d\vec{r}\rho(\vec{r})\left(\frac{\delta}{\delta\phi_i^*(\vec{r}',\sigma')}\vec{\nabla}\cdot\vec{J}(\vec{r})\right) \tag{B.5.14}$$

The second term in this equation can be written as

$$\begin{aligned}
&\int d\vec{r}\rho(\vec{r})\left[\frac{\delta}{\delta\phi_i^*(\vec{r}',\sigma')}\vec{\nabla}\cdot\vec{J}(\vec{r})\right] \\
&= \int d\vec{r}\rho(\vec{r})\left[\frac{\delta}{\delta\phi_i^*(\vec{r}',\sigma')}\sum_{\lambda\mu\nu}\epsilon_{\lambda\mu\nu}\partial_\lambda J_{\mu\nu}\right] \\
&= -i\int d\vec{r}\rho(\vec{r})\left[\frac{\delta}{\delta\phi_i^*(\vec{r}',\sigma')}\sum_{\lambda\mu\nu}\epsilon_{\lambda\mu\nu}\sum_j\sum_{\sigma_1\sigma_2}\left(\partial_\lambda\phi_j^*(\vec{r},\sigma_1)\right)\left(\partial_\mu\phi_j(\vec{r},\sigma_2)\right)\langle\sigma_1|\sigma_\nu|\sigma_2\rangle\right] \\
&= i\sum_{\lambda\mu\nu}\epsilon_{\lambda\mu\nu}(\partial_\lambda\rho(\vec{r}'))\sum_{\sigma_2}\left(\partial_\mu\phi_i(\vec{r}',\sigma_2)\right)\left\langle\sigma'|\sigma_\nu|\sigma_2\right\rangle \\
&= -i\vec{\nabla}\rho(\vec{r}')\cdot\left(\sum_\sigma\left\langle\sigma'|\vec{\sigma}|\sigma\right\rangle\times\vec{\nabla}\phi_i(\vec{r}',\sigma)\right),
\end{aligned} \tag{B.5.15}$$

where we use a relation $\vec{\nabla}\times\vec{\nabla}\phi = \sum_{\lambda\mu\nu}\epsilon_{\lambda\mu\nu}\partial_\lambda\partial_\mu\phi = \vec{0}$.

$$
\begin{aligned}
&\frac{\delta}{\delta\phi^*_{i\in\tau'}(\vec{r}',\sigma')}\int d\vec{r}\rho^{(\tau)}(\vec{r})\vec{\nabla}\cdot\vec{J}^{(\tau)}(\vec{r}) \\
&= \left(\vec{\nabla}\cdot\vec{J}^{(\tau')}(\vec{r}')\right)\phi_i(\vec{r}'\sigma') - i\vec{\nabla}\rho^{(\tau')}(\vec{r}')\cdot\left(\sum_\sigma\left\langle\sigma'\left|\vec{\sigma}\right|\sigma\right\rangle\times\vec{\nabla}\phi_i(\vec{r}',\sigma)\right)
\end{aligned}
\tag{B.5.16}
$$

$$
\begin{aligned}
&\frac{\delta}{\delta\phi^*_i(\vec{r}',\sigma')}\int d\vec{r}\vec{j}(\vec{r})\cdot(\vec{\nabla}\times\vec{\rho}) \\
&= \sum_{\lambda\mu\nu}\epsilon_{\lambda\mu\nu}\frac{\delta}{\delta\phi^*_i(\vec{r}',\sigma')}\int d\vec{r}j_\lambda(\vec{r})\partial_\mu\rho_\nu(\vec{r}) \\
&= \sum_{\lambda\mu\nu}\epsilon_{\lambda\mu\nu}\left[-i(\partial_\lambda\phi(\vec{r}',\sigma'))(\partial_\mu\rho_\nu(\vec{r}))-(\partial_\mu j_\lambda(\vec{r}'))\sum_\sigma\phi(\vec{r}',\sigma)\left\langle\sigma'\left|\sigma_\nu\right|\sigma\right\rangle\right] \\
&= -i(\vec{\nabla}\times\vec{\rho}(\vec{r}'))\cdot\nabla\phi(\vec{r}',\sigma')+\sum_\sigma\left(\vec{\nabla}\times\vec{j}(\vec{r}')\right)\cdot\left\langle\sigma'\left|\vec{\sigma}\right|\sigma\right\rangle\phi(\vec{r}',\sigma)
\end{aligned}
\tag{B.5.17}
$$

$$
\begin{aligned}
&\frac{\delta}{\delta\phi^*_{i\in\tau'}(\vec{r}',\sigma')}\int d\vec{r}\vec{j}^{(\tau)}(\vec{r})\cdot(\vec{\nabla}\times\vec{\rho}^{(\tau)}) \\
&= -i(\vec{\nabla}\times\vec{\rho}^{(\tau')}(\vec{r}'))\cdot\nabla\phi(\vec{r}',\sigma')+\sum_\sigma\left(\vec{\nabla}\times\vec{j}^{(\tau')}(\vec{r}')\right)\cdot\left\langle\sigma'\left|\vec{\sigma}\right|\sigma\right\rangle\phi(\vec{r}',\sigma)
\end{aligned}
\tag{B.5.18}
$$

B_{10} **term**

$$
\begin{aligned}
&\frac{\delta}{\delta\phi^*_i(\vec{r}',\sigma')}\int d\vec{r}\vec{\rho}(\vec{r})^2 \\
&= 2\vec{\rho}(\vec{r}')\cdot\sum_\sigma\left\langle\sigma'\left|\vec{\sigma}\right|\sigma\right\rangle\phi_i(\vec{r}',\sigma)
\end{aligned}
\tag{B.5.19}
$$

B_{11} **term**

$$
\begin{aligned}
&\frac{\delta}{\delta\phi^*_{i\in\tau'}(\vec{r}',\sigma')}\int d\vec{r}\sum_\tau\vec{\rho}^{(\tau)}(\vec{r})^2 \\
&= 2\vec{\rho}^{(\tau')}(\vec{r}')\cdot\sum_\sigma\left\langle\sigma'\left|\vec{\sigma}\right|\sigma\right\rangle\phi_i(\vec{r}',\sigma)
\end{aligned}
\tag{B.5.20}
$$

B_{12} term

$$\begin{aligned}
&\frac{\delta}{\delta\phi_i^*(\vec{r}',\sigma')}\int d\vec{r}\rho(\vec{r})^{\alpha}\vec{\rho}(\vec{r})^2 \\
&= \alpha\rho(\vec{r}')^{\alpha-1}\vec{\rho}(\vec{r})^2\phi_i(\vec{r}',\sigma') + 2\rho(\vec{r}')^{\alpha}\vec{\rho}(\vec{r}')\sum_{\sigma}\left\langle\sigma'\left|\vec{\sigma}\right|\sigma\right\rangle\phi_i(\vec{r}',\sigma)
\end{aligned} \tag{B.5.21}$$

B_{13} term

$$\begin{aligned}
&\frac{\delta}{\delta\phi_{i\in\tau'}^*(\vec{r}',\sigma')}\int d\vec{r}\vec{\rho}^{(\tau)}(\vec{r})^{\alpha}\vec{\rho}^{(\tau)}(\vec{r})^2 \\
&= \alpha\rho^{(\tau')}(\vec{r}')^{\alpha-1}\vec{\rho}^{(\tau')}(\vec{r})^2\phi_i(\vec{r}',\sigma') + 2\rho^{(\tau')}(\vec{r}')^{\alpha}\vec{\rho}^{(\tau')}(\vec{r}')\sum_{\sigma}\left\langle\sigma'\left|\vec{\sigma}\right|\sigma\right\rangle\phi_i(\vec{r}',\sigma)
\end{aligned} \tag{B.5.22}$$

B_{14} term

$$\begin{aligned}
&\frac{\delta}{\delta\phi_i^*(\vec{r}',\sigma')}\int d\vec{r}\left[\vec{T}(\vec{r})\cdot\vec{\rho}(\vec{r}) - \overleftrightarrow{J}^2\right] \\
&= \sum_{\sigma}\left(\vec{T}(\vec{r}')\cdot\left\langle\sigma'\left|\vec{\sigma}\right|\sigma\right\rangle\right)\phi(\vec{r}',\sigma) + \int d\vec{r}\vec{\rho}(\vec{r})\cdot\left(\frac{\delta}{\delta\phi_i^*}\vec{T}(\vec{r})\right) - 2\int d\vec{r}\sum_{\mu\nu}J_{\mu\nu}(\vec{r})\cdot\left(\frac{\delta}{\delta\phi_i^*}J_{\mu\nu}(\vec{r})\right)
\end{aligned} \tag{B.5.23}$$

The second term in Eq. (B.5.23) can be written as

$$\int d\vec{r}\vec{\rho}(\vec{r})\cdot\left(\frac{\delta}{\delta\phi_i^*}\vec{T}(\vec{r})\right) = -\sum_{\sigma}\left\langle\sigma'\left|\vec{\sigma}\right|\sigma\right\rangle\cdot\left[\vec{\rho}(\vec{r}')\nabla^2\phi(\vec{r}',\sigma) + \vec{\nabla}\rho(\vec{r}')\cdot\vec{\nabla}\phi_i(\vec{r},\sigma)\right]. \tag{B.5.24}$$

The third term in Eq. (B.5.23) can be written as

$$\begin{aligned}
&-2\int d\vec{r}\sum_{\mu\nu}J_{\mu\nu}(\vec{r})\cdot\left(\frac{\delta}{\delta\phi_i^*}J_{\mu\nu}(\vec{r})\right) \\
&= i\sum_{\mu\nu}\sum_{\sigma}\left[2J_{\mu\nu}(\vec{r})(\partial_{\mu}\phi_i(\vec{r}',\sigma)) + (\partial_{\mu}J_{\mu\nu}(\vec{r}))\phi_i(\vec{r}',\sigma)\right]\left\langle\sigma'\left|\sigma_{\nu}\right|\sigma\right\rangle.
\end{aligned} \tag{B.5.25}$$

B_{16} term

$$\begin{aligned}
&\frac{\delta}{\delta\phi^*_{i\in\tau'}(\vec{r}',\sigma')}\int d\vec{r}\sum_\tau\left[\vec{T}^{(\tau)}(\vec{r})\cdot\vec{\rho}(\vec{r})-(\overleftrightarrow{J}^{(\tau)}(\vec{r}'))^2\right]\\
&= \sum_\sigma\left(\vec{T}^{(\tau')}(\vec{r}')\cdot\left\langle\sigma'\left|\vec{\sigma}\right|\sigma\right\rangle\right)\phi_i(\vec{r}',\sigma)\\
&\quad+\sum_\tau\left[\int d\vec{r}\vec{\rho}^{(\tau)}(\vec{r})\cdot\left(\frac{\delta}{\delta\phi^*_i}\vec{T}^{(\tau)}(\vec{r})\right)-2\int d\vec{r}\sum_{\mu\nu}J^{(\tau)}_{\mu\nu}(\vec{r})\cdot\left(\frac{\delta}{\delta\phi^*_i}J^{(\tau)}_{\mu\nu}(\vec{r})\right)\right]\\
&= \sum_\sigma\left(\vec{T}^{(\tau')}(\vec{r}')\cdot\left\langle\sigma'\left|\vec{\sigma}\right|\sigma\right\rangle\right)\phi_i(\vec{r}',\sigma)\\
&\quad-\sum_\sigma\left\langle\sigma'\left|\vec{\sigma}\right|\sigma\right\rangle\cdot\left[\vec{\rho}^{(\tau')}(\vec{r}')\nabla^2\phi_i(\vec{r}',\sigma)+\vec{\nabla}\rho^{(\tau')}(\vec{r}')\cdot\vec{\nabla}\phi_i(\vec{r},\sigma)\right]\\
&\quad+i\sum_{\mu\nu}\sum_\sigma\left[2J^{(\tau')}_{\mu\nu}(\vec{r})(\partial_\mu\phi_i(\vec{r}',\sigma))+(\partial_\mu J^{(\tau')}_{\mu\nu}(\vec{r}))\phi_i(\vec{r}',\sigma)\right]\left\langle\sigma'\left|\sigma_\nu\right|\sigma\right\rangle \qquad \text{(B.5.26)}
\end{aligned}$$

B_{15} term

$$\begin{aligned}
&\frac{\delta}{\delta\phi^*_i(\vec{r}',\sigma')}\int d\vec{r}\vec{\rho}(\vec{r})\cdot\nabla^2\vec{\rho}(\vec{r})\\
&= 2\sum_\sigma\left\langle\sigma'\left|\vec{\sigma}\right|\sigma\right\rangle\cdot\nabla^2\vec{\rho}(\vec{r}')\phi(\vec{r}',\sigma) \qquad \text{(B.5.27)}
\end{aligned}$$

B_{17} term

$$\begin{aligned}
&\frac{\delta}{\delta\phi^*_{i\in\tau'}(\vec{r}',\sigma')}\int d\vec{r}\sum_\tau\vec{\rho}^{(\tau)}(\vec{r})\cdot\nabla^2\vec{\rho}^{(\tau)}(\vec{r})\\
&= 2\sum_\sigma\left\langle\sigma'\left|\vec{\sigma}\right|\sigma\right\rangle\cdot\nabla^2\vec{\rho}^{(\tau')}(\vec{r}')\phi(\vec{r}',\sigma) \qquad \text{(B.5.28)}
\end{aligned}$$

Coulomb term

$$\begin{aligned}
&\frac{\delta}{\delta\phi^*_{i\in\tau'}(\vec{r}'',\sigma')}\left[\frac{e^2}{2}\int d\vec{r}d\vec{r}'\frac{\rho_p(\vec{r})\rho_p(\vec{r}')}{|\vec{r}-\vec{r}'|}-\frac{3}{4}\left(\frac{3}{\pi}\right)^{1/3}e^2\rho_p^{4/3}(\vec{r})\right]\\
&= e^2\left[\int d\vec{r}\frac{\rho(\vec{r})}{|\vec{r}-\vec{r}'|}-\left(\frac{3}{\pi}\right)^{1/3}\rho_p(\vec{r})^{1/3}\right]\phi_i(\vec{r}'',\sigma')\delta_{\tau',p} \qquad \text{(B.5.29)}
\end{aligned}$$

Bibliography

[1] T. Myo, S. Sugimoto, K. Kat, H. Toki, and K. Ikeda, Progress of Theoretical Physics **117**, 257 (2007), URL `http://ptp.oxfordjournals.org/content/117/2/257.abstract`.

[2] K. Ikeda, N. Takigawa, and H. Horiuchi, Progress of Theoretical Physics Supplement **E68**, 464 (1968), URL `http://ptps.oxfordjournals.org/content/E68/464.abstract`.

[3] K. Ikeda and R. Tamagaki, Progress of Theoretical Physics Supplement **62**, 1 (1977), URL `http://ptps.oxfordjournals.org/content/62/1.short`.

[4] K. Ikeda, H. Horiuchi, and S. Saito, Progress of Theoretical Physics Supplement **68**, 1 (1980), URL `http://ptps.oxfordjournals.org/content/68/1.short`.

[5] Y. Fujiwara, H. Horiuchi, K. Ikeda, M. Kamimura, K. Kiyoshi, Y. Suzuki, and E. Uegaki, Progress of Theoretical Physics Supplement **68**, 29 (1980), URL `http://ptps.oxfordjournals.org/content/68/29.short`.

[6] J. A. Wheeler, Phys. Rev. **52**, 1083 (1937), URL `http://link.aps.org/doi/10.1103/PhysRev.52.1083`.

[7] J. A. Wheeler, Phys. Rev. **52**, 1107 (1937), URL `http://link.aps.org/doi/10.1103/PhysRev.52.1107`.

[8] D. Brink and A. Weiguny, Nuclear Physics A **120**, 59 (1968), ISSN 0375-9474, URL `http://www.sciencedirect.com/science/article/pii/0375947468900596`.

[9] S. Saito, Progress of Theoretical Physics **40**, 893 (1968), URL `http://ptp.oxfordjournals.org/content/40/4/893.short`.

[10] S. Saito, Progress of Theoretical Physics **41**, 705 (1969), URL `http://ptp.oxfordjournals.org/content/41/3/705.abstract`.

[11] Y. Kanada-En'yo and H. Horiuchi, Progress of Theoretical Physics **93**, 115 (1995), URL `http://ptp.oxfordjournals.org/content/93/1/115.abstract`.

[12] Y. Kanada-En'yo, H. Horiuchi, and A. Ono, Phys. Rev. C **52**, 628 (1995), URL `http://link.aps.org/doi/10.1103/PhysRevC.52.628`.

[13] Y. Kanada-En'yo, Progress of Theoretical Physics **117**, 655 (2007), URL `http://ptp.oxfordjournals.org/content/117/4/655.abstract`.

[14] T. Neff and H. Feldmeier, Nuclear Physics A **738**, 357 (2004), ISSN 0375-9474, URL `http://www.sciencedirect.com/science/article/pii/S0375947404006025`.

[15] R. B. Wiringa, S. C. Pieper, J. Carlson, and V. R. Pandharipande, Phys. Rev. C **62**, 014001 (2000), URL `http://link.aps.org/doi/10.1103/PhysRevC.62.014001`.

[16] J. Carlson, Phys. Rev. C **36**, 2026 (1987), URL `http://link.aps.org/doi/10.1103/PhysRevC.36.2026`.

[17] P. Navrátil, J. P. Vary, and B. R. Barrett, Phys. Rev. C **62**, 054311 (2000), URL `http://link.aps.org/doi/10.1103/PhysRevC.62.054311`.

[18] P. Navrátil, S. Quaglioni, I. Stetcu, and B. R. Barrett, Journal of Physics G: Nuclear and Particle Physics **36**, 083101 (2009), URL `http://stacks.iop.org/0954-3899/36/i=8/a=083101`.

[19] P. Maris, J. P. Vary, and A. M. Shirokov, Phys. Rev. C **79**, 014308 (2009), URL `http://link.aps.org/doi/10.1103/PhysRevC.79.014308`.

[20] E. Epelbaum, H. Krebs, D. Lee, and U.-G. Meißner, Phys. Rev. Lett. **106**, 192501 (2011), URL `http://link.aps.org/doi/10.1103/PhysRevLett.106.192501`.

[21] T. Abe, P. Maris, T. Otsuka, N. Shimizu, Y. Utsuno, and J. P. Vary, Phys. Rev. C **86**, 054301 (2012), URL `http://link.aps.org/doi/10.1103/PhysRevC.86.054301`.

[22] K. A. Brueckner, J. L. Gammel, and H. Weitzner, Phys. Rev. **110**, 431 (1958), URL `http://link.aps.org/doi/10.1103/PhysRev.110.431`.

[23] T. H. R. Skyrme, Philosophical Magazine **1**, 1043 (1956), URL `http://www.tandfonline.com/doi/abs/10.1080/14786435608238186`.

[24] T. Skyrme, Nuclear Physics **9**, 615 (1959), ISSN 0029-5582, URL `http://www.sciencedirect.com/science/article/pii/0029558258903456`.

[25] D. Vautherin and D. M. Brink, Phys. Rev. C **5**, 626 (1972), URL `http://link.aps.org/doi/10.1103/PhysRevC.5.626`.

[26] I. C. on Nuclear Self-Consistent Fields (Trieste) (1975.), G. Ripka, M. Porneuf, and I. C. for Theoretical Physics, *Proceedings of the international conference on nuclear self-consistent fields, organized by and held at the international centre for theoretical physics, trieste, february 24-28, 1975 / edited by g. ripka and m. porneuf ; conference directors, l. fonda, g. ripka, m. veneroni* (1975), includes index.

[27] M. Bender, P.-H. Heenen, and P.-G. Reinhard, Rev. Mod. Phys. **75**, 121 (2003), URL `http://link.aps.org/doi/10.1103/RevModPhys.75.121`.

[28] J. Blaizot and D. Gogny, Nuclear Physics A **284**, 429 (1977), ISSN 0375-9474, URL `http://www.sciencedirect.com/science/article/pii/0375947477903955`.

[29] P. G. Reinhard and K. Goeke, Reports on Progress in Physics **50**, 1 (1987), URL `http://stacks.iop.org/0034-4885/50/i=1/a=001`.

[30] S. Shinohara, H. Ohta, T. Nakatsukasa, and K. Yabana, Phys. Rev. C **74**, 054315 (2006), URL `http://link.aps.org/doi/10.1103/PhysRevC.74.054315`.

[31] Y. Fukuoka, S. Shinohara, Y. Funaki, T. Nakatsukasa, and K. Yabana, Phys. Rev. C **88**, 014321 (2013), URL `http://link.aps.org/doi/10.1103/PhysRevC.88.014321`.

[32] A. Tohsaki, H. Horiuchi, P. Schuck, and G. Röpke, Phys. Rev. Lett. **87**, 192501 (2001), URL `http://link.aps.org/doi/10.1103/PhysRevLett.87.192501`.

[33] Y. Funaki, A. Tohsaki, H. Horiuchi, P. Schuck, and G. Röpke, Phys. Rev. C **67**, 051306 (2003), URL `http://link.aps.org/doi/10.1103/PhysRevC.67.051306`.

[34] F. Hoyle, Astrophysical Journal Supplement **1**, 121 (1954), URL `http://adsabs.harvard.edu/abs/1954ApJS....1..121H`.

[35] D. N. F. Dunbar, R. E. Pixley, W. A. Wenzel, and W. Whaling, Phys. Rev. **92**, 649 (1953), URL `http://link.aps.org/doi/10.1103/PhysRev.92.649`.

[36] H. Morinaga, Physics Letters **21**, 78 (1966), ISSN 0031-9163, URL `http://www.sciencedirect.com/science/article/pii/0031916366913497`.

[37] E. Uegaki, Y. Abe, and H. Okabe, ShigetEand Tanaka, Progress of Theoretical Physics **62**, 1621 (1979), URL `http://ptp.oxfordjournals.org/content/62/6/1621.abstract`.

[38] M. Kamimura, Nuclear Physics A **351**, 456 (1981), ISSN 0375-9474, URL `http://www.sciencedirect.com/science/article/pii/0375947481901822`.

[39] P. Navrátil and W. E. Ormand, Phys. Rev. C **68**, 034305 (2003), URL `http://link.aps.org/doi/10.1103/PhysRevC.68.034305`.

[40] F. Ajzenberg-Selove, Nuclear Physics A **506**, 1 (1990), ISSN 0375-9474, URL `http://www.sciencedirect.com/science/article/pii/037594749090271M`.

[41] M. Freer, H. Fujita, Z. Buthelezi, J. Carter, R. W. Fearick, S. V. Förtsch, R. Neveling, S. M. Perez, P. Papka, F. D. Smit, et al., Phys. Rev. C **80**, 041303 (2009), URL `http://link.aps.org/doi/10.1103/PhysRevC.80.041303`.

[42] W. R. Zimmerman, N. E. Destefano, M. Freer, M. Gai, and F. D. Smit, Phys. Rev. C **84**, 027304 (2011), URL `http://link.aps.org/doi/10.1103/PhysRevC.84.027304`.

[43] M. Itoh, H. Akimune, M. Fujiwara, U. Garg, N. Hashimoto, T. Kawabata, K. Kawase, S. Kishi, T. Murakami, K. Nakanishi, et al., Phys. Rev. C **84**, 054308 (2011), URL `http://link.aps.org/doi/10.1103/PhysRevC.84.054308`.

[44] M. Freer, M. Itoh, T. Kawabata, H. Fujita, H. Akimune, Z. Buthelezi, J. Carter, R. W. Fearick, S. V. Förtsch, M. Fujiwara, et al., Phys. Rev. C **86**, 034320 (2012), URL `http://link.aps.org/doi/10.1103/PhysRevC.86.034320`.

[45] W. R. Zimmerman, M. W. Ahmed, B. Bromberger, S. C. Stave, A. Breskin, V. Dangendorf, T. Delbar, M. Gai, S. S. Henshaw, J. M. Mueller, et al., Phys. Rev. Lett. **110**, 152502 (2013), URL `http://link.aps.org/doi/10.1103/PhysRevLett.110.152502`.

[46] M. Freer, S. Almaraz-Calderon, A. Aprahamian, N. I. Ashwood, M. Barr, B. Bucher, P. Copp, M. Couder, N. Curtis, X. Fang, et al., Phys. Rev. C **83**, 034314 (2011), URL `http://link.aps.org/doi/10.1103/PhysRevC.83.034314`.

[47] T. Yamada, H. Horiuchi, K. Ikeda, Y. Funaki, and A. Tohsaki, Journal of Physics: Conference Series **111**, 012008 (2008), URL `http://stacks.iop.org/1742-6596/111/i=1/a=012008`.

[48] A. Ozawa, O. Bochkarev, L. Chulkov, D. Cortina, H. Geissel, M. Hellström, M. Ivanov, R. Janik, K. Kimura, T. Kobayashi, et al., Nuclear Physics A **691**, 599 (2001), ISSN 0375-9474, URL `http://www.sciencedirect.com/science/article/pii/S0375947401005632`.

[49] M. Chernykh, H. Feldmeier, T. Neff, P. von Neumann-Cosel, and A. Richter, Phys. Rev. Lett. **98**, 032501 (2007), URL `http://link.aps.org/doi/10.1103/PhysRevLett.98.032501`.

[50] T. Suhara and Y. Kanada-En'yo, Progress of Theoretical Physics **123**, 303 (2010), URL `http://ptp.oxfordjournals.org/content/123/2/303.abstract`.

[51] T. Suhara and Y. Kanada-En'yo, (private communication).

[52] A. N. Danilov, T. L. Belyaeva, A. S. Demyanova, S. A. Goncharov, and A. A. Ogloblin, Phys. Rev. C **80**, 054603 (2009), URL `http://link.aps.org/doi/10.1103/PhysRevC.80.054603`.

[53] I. Sick and J. McCarthy, Nuclear Physics A **150**, 631 (1970), ISSN 0375-9474, URL `http://www.sciencedirect.com/science/article/pii/0375947470904239`.

[54] A. Nakada, Y. Torizuka, and Y. Horikawa, Phys. Rev. Lett. **27**, 745 (1971), URL `http://link.aps.org/doi/10.1103/PhysRevLett.27.745`.

[55] A. Nakada, Y. Torizuka, and Y. Horikawa, Phys. Rev. Lett. **27**, 1102 (1971), URL `http://link.aps.org/doi/10.1103/PhysRevLett.27.1102.2`.

[56] P. Strehl and T. Schucan, Physics Letters B **27**, 641 (1968), ISSN 0370-2693, URL `http://www.sciencedirect.com/science/article/pii/0370269368903031`.

[57] Y. Kanada-En'yo, Progress of Theoretical Physics **121**, 895 (2009), URL `http://ptp.oxfordjournals.org/content/121/4/895.abstract`.

[58] Y. Kanada-En'yo, Progress of Theoretical Physics **121**, 895 (2009), URL `http://ptp.oxfordjournals.org/content/121/4/895.abstract`.

[59] Y. Funaki, A. Tohsaki, H. Horiuchi, P. Schuck, and G. Rpke, The European Physical Journal A - Hadrons and Nuclei **28**, 259 (2006), ISSN 1434-6001, URL `http://dx.doi.org/10.1140/epja/i2006-10061-5`.

[60] A. Arima, H. Horiuchi, and T. Sebe, Physics Letters B **24**, 129 (1967), ISSN 0370-2693, URL `http://www.sciencedirect.com/science/article/pii/0370269367904996`.

[61] W. C. Haxton and C. Johnson, Phys. Rev. Lett. **65**, 1325 (1990), URL `http://link.aps.org/doi/10.1103/PhysRevLett.65.1325`.

[62] Y. Utsuno and S. Chiba, Phys. Rev. C **83**, 021301 (2011), URL `http://link.aps.org/doi/10.1103/PhysRevC.83.021301`.

[63] Y. Suzuki, Progress of Theoretical Physics **55**, 1751 (1976), URL `http://ptp.oxfordjournals.org/content/55/6/1751.abstract`.

[64] K. Fukatsu, K. Katō, and H. Tanaka, Progress of Theoretical Physics **81**, 738 (1989), URL `http://ptp.oxfordjournals.org/content/81/4/738.abstract`.

[65] K. Fukatsu and K. Katō, Progress of Theoretical Physics **87**, 151 (1992), URL `http://ptp.oxfordjournals.org/content/87/1/151.abstract`.

[66] H. Horiuchi (1975), proc. INS-IPCR Int. Symp. on Cluster Structure of Nuclei and Transfer Reactions Induced by Heavy-Ions, Tokyo.

[67] P. Descouvemont, Phys. Rev. C **47**, 210 (1993), URL `http://link.aps.org/doi/10.1103/PhysRevC.47.210`.

[68] N. Furutachi, M. Kimura, A. Doté, Y. Kanada-En'yo, and S. Oryu, Progress of Theoretical Physics **119**, 403 (2008), URL `http://ptp.oxfordjournals.org/content/119/3/403.abstract`.

[69] Y. Funaki, T. Yamada, H. Horiuchi, G. Röpke, P. Schuck, and A. Tohsaki, Phys. Rev. Lett. **101**, 082502 (2008), URL `http://link.aps.org/doi/10.1103/PhysRevLett.101.082502`.

[70] Y. Funaki, T. Yamada, A. Tohsaki, H. Horiuchi, G. Röpke, and P. Schuck, Phys. Rev. C **82**, 024312 (2010), URL `http://link.aps.org/doi/10.1103/PhysRevC.82.024312`.

[71] T. Yamada, Y. Funaki, T. Myo, H. Horiuchi, K. Ikeda, G. Röpke, P. Schuck, and A. Tohsaki, Phys. Rev. C **85**, 034315 (2012), URL `http://link.aps.org/doi/10.1103/PhysRevC.85.034315`.

[72] J. Vary, B. Barrett, R. Lloyd, P. Navrátil, A. Nogga, and W. Ormand, Nuclear Physics A **746**, 123 (2004), ISSN 0375-9474, ¡ce:title¿Proceedings of the Sixth International Conference on Radioactive Nuclear Beams (RNB6)¡/ce:title¿, URL `http://www.sciencedirect.com/science/article/pii/S0375947404009777`.

[73] A. Shirokov, V. Kulikov, A. Mazur, E. Mazur, P. Maris, and J. Vary, Bulletin of the Russian Academy of Sciences: Physics **74**, 538 (2010), ISSN 1062-8738, URL `http://dx.doi.org/10.3103/S1062873810040258`.

[74] R. Roth, J. Langhammer, A. Calci, S. Binder, and P. Navrátil, Phys. Rev. Lett. **107**, 072501 (2011), URL `http://link.aps.org/doi/10.1103/PhysRevLett.107.072501`.

[75] M. Włoch, D. J. Dean, J. R. Gour, M. Hjorth-Jensen, K. Kowalski, T. Papenbrock, and P. Piecuch, Phys. Rev. Lett. **94**, 212501 (2005), URL `http://link.aps.org/doi/10.1103/PhysRevLett.94.212501`.

[76] G. Hagen, D. J. Dean, M. Hjorth-Jensen, T. Papenbrock, and A. Schwenk, Phys. Rev. C **76**, 044305 (2007), URL `http://link.aps.org/doi/10.1103/PhysRevC.76.044305`.

[77] G. Hagen, T. Papenbrock, D. J. Dean, M. Hjorth-Jensen, and B. V. Asokan, Phys. Rev. C **80**, 021306 (2009), URL `http://link.aps.org/doi/10.1103/PhysRevC.80.021306`.

[78] S. Binder, J. Langhammer, A. Calci, P. Navrátil, and R. Roth, Phys. Rev. C **87**, 021303 (2013), URL `http://link.aps.org/doi/10.1103/PhysRevC.87.021303`.

[79] H. Hergert, S. K. Bogner, S. Binder, A. Calci, J. Langhammer, R. Roth, and A. Schwenk, Phys. Rev. C **87**, 034307 (2013), URL `http://link.aps.org/doi/10.1103/PhysRevC.87.034307`.

[80] D. Tilley, C. Cheves, J. Kelley, S. Raman, and H. Weller, Nuclear Physics A **636**, 249 (1998), ISSN 0375-9474, URL `http://www.sciencedirect.com/science/article/pii/S0375947498001298`.

[81] D. Tilley, H. Weller, and C. Cheves, Nuclear Physics A **564**, 1 (1993), ISSN 0375-9474, URL `http://www.sciencedirect.com/science/article/pii/0375947493900737`.

[82] H. Horiuchi and K. Ikeda, Progress of Theoretical Physics **40**, 277 (1968), URL `http://ptp.oxfordjournals.org/content/40/2/277.abstract`.

[83] T. Inoue, T. Sebe, H. Hagiwara, and A. Arima, Nuclear Physics **59**, 1 (1964), ISSN 0029-5582, URL `http://www.sciencedirect.com/science/article/pii/0029558264901105`.

[84] A. Arima, M. Sakakura, and T. Sebe, Nuclear Physics A **170**, 273 (1971), ISSN 0375-9474, URL `http://www.sciencedirect.com/science/article/pii/0375947471906361`.

[85] Y. Akiyama, A. Arima, and T. Sebe, Nuclear Physics A **138**, 273 (1969), ISSN 0375-9474, URL `http://www.sciencedirect.com/science/article/pii/0375947469903364`.

[86] T. Matsuse, M. Kamimura, and Y. Fukushima, Progress of Theoretical Physics **53**, 706 (1975), URL `http://ptp.oxfordjournals.org/content/53/3/706.abstract`.

[87] Y. Fujiwara, Progress of Theoretical Physics **62**, 138 (1979), URL `http://ptp.oxfordjournals.org/content/62/1/138.abstract`.

[88] H. Kazama, K. Katō, and H. Tanaka, Progress of Theoretical Physics **71**, 215 (1984), URL `http://ptp.oxfordjournals.org/content/71/1/215.abstract`.

[89] F. Nemoto and H. Bandō, Progress of Theoretical Physics **47**, 1210 (1972), URL `http://ptp.oxfordjournals.org/content/47/4/1210.abstract`.

[90] J. Hiura, Y. Abe, S. Saitō, and O. Endō, Progress of Theoretical Physics **42**, 555 (1969), URL `http://ptp.oxfordjournals.org/content/42/3/555.abstract`.

[91] F. Nemoto, Y. Yamamoto, H. Horiuchi, Y. Suzuki, and K. Ikeda, Progress of Theoretical Physics **54**, 104 (1975), URL `http://ptp.oxfordjournals.org/content/54/1/104.abstract`.

[92] M. Dufour, P. Descouvemont, and D. Baye, Phys. Rev. C **50**, 795 (1994), URL `http://link.aps.org/doi/10.1103/PhysRevC.50.795`.

[93] Y. Kanada-En'yo and H. Horiuchi, Progress of Theoretical Physics **93**, 115 (1995), URL `http://ptp.oxfordjournals.org/content/93/1/115.abstract`.

[94] Y. Taniguchi, M. Kimura, and H. Horiuchi, Progress of Theoretical Physics **112**, 475 (2004), URL `http://ptp.oxfordjournals.org/content/112/3/475.abstract`.

[95] M. Kimura, Phys. Rev. C **69**, 044319 (2004), URL `http://link.aps.org/doi/10.1103/PhysRevC.69.044319`.

[96] R. Roth, T. Neff, H. Hergert, and H. Feldmeier, Nuclear Physics A **745**, 3 (2004), ISSN 0375-9474, URL `http://www.sciencedirect.com/science/article/pii/S0375947404008917`.

[97] H. Ohta, K. Yabana, and T. Nakatsukasa, Phys. Rev. C **70**, 014301 (2004), URL `http://link.aps.org/doi/10.1103/PhysRevC.70.014301`.

[98] T. Tomoda and A. Arima, Nuclear Physics A **303**, 217 (1978), ISSN 0375-9474, URL `http://www.sciencedirect.com/science/article/pii/0375947478900520`.

[99] C. D. Jager, H. D. Vries, and C. D. Vries, Atomic Data and Nuclear Data Tables **14**, 479 (1974), URL `http://www.sciencedirect.com/science/article/pii/S0092640X74800021`.

[100] R. Cusson and H. Lee, Nuclear Physics A **211**, 429 (1973), URL `http://www.sciencedirect.com/science/article/pii/0375947473904351`.

[101] E. Caurier and B. Grammaticos, Nuclear Physics A **279**, 333 (1977), ISSN 0375-9474, URL `http://www.sciencedirect.com/science/article/pii/0375947477902329`.

[102] J. Hiura, F. Nemoto, and H. BandH, Progress of Theoretical Physics Supplement **52**, 173 (1972), URL `http://ptps.oxfordjournals.org/content/52/173.short`.

[103] E. A. Knight, R. P. Singhal, R. G. Arthur, and M. W. S. Macauley, Journal of Physics G: Nuclear Physics **7**, 1115 (1981), URL `http://stacks.iop.org/0305-4616/7/i=8/a=017`.

[104] M. Beiner, H. Flocard, N. V. Giai, and P. Quentin, Nuclear Physics A **238**, 29 (1975), ISSN 0375-9474, URL `http://www.sciencedirect.com/science/article/pii/0375947475903383`.

[105] N. V. Giai and H. Sagawa, Physics Letters B **106**, 379 (1981), ISSN 0370-2693, URL `http://www.sciencedirect.com/science/article/pii/0370269381906468`.

[106] E. Chabanat, P. Bonche, P. Haensel, J. Meyer, and R. Schaeffer, Nuclear Physics A **635**, 231 (1998), ISSN 0375-9474, URL `http://www.sciencedirect.com/science/article/pii/S0375947498001808`.

[107] H. Krivine, J. Treiner, and O. Bohigas, Nuclear Physics A **336**, 155 (1980), ISSN 0375-9474, URL `http://www.sciencedirect.com/science/article/pii/0375947480906181`.

[108] J. Bartel, P. Quentin, M. Brack, C. Guet, and H.-B. Hkansson, Nuclear Physics A **386**, 79 (1982), ISSN 0375-9474, URL `http://www.sciencedirect.com/science/article/pii/0375947482904031`.

[109] K.-H. Kim, T. Otsuka, and P. Bonche, Journal of Physics G: Nuclear and Particle Physics **23**, 1267 (1997), URL `http://stacks.iop.org/0954-3899/23/i=10/a=014`.

[110] J. Dechargé and D. Gogny, Phys. Rev. C **21**, 1568 (1980), URL `http://link.aps.org/doi/10.1103/PhysRevC.21.1568`.

[111] J. Berger, M. Girod, and D. Gogny, Computer Physics Communications **63**, 365 (1991), ISSN 0010-4655, URL `http://www.sciencedirect.com/science/article/pii/001046559190263K`.

[112] F. Chappert, M. Girod, and S. Hilaire, Physics Letters B **668**, 420 (2008), ISSN 0370-2693, URL `http://www.sciencedirect.com/science/article/pii/S0370269308011271`.

[113] S. Goriely, S. Hilaire, M. Girod, and S. Péru, Phys. Rev. Lett. **102**, 242501 (2009), URL `http://link.aps.org/doi/10.1103/PhysRevLett.102.242501`.

[114] M. W. Kirson, Nuclear Physics A **781**, 350 (2007), ISSN 0375-9474, URL `http://www.sciencedirect.com/science/article/pii/S037594740600769X`.